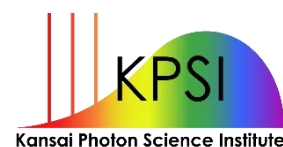




# ANNUAL REPORT 2018



**Kansai Photon Science Institute**  
Quantum Beam Science Research Directorate  
National Institutes for  
Quantum and Radiological Science and Technology





# ANNUAL REPORT 2018

# Contents

<b>Preface</b>	<b>1</b>
<b>Activities of KPSI</b>	<b>3</b>
<b>User Facilities</b>	<b>7</b>
<b>Research Highlights</b>	<b>13</b>
<b>Publication List</b>	<b>55</b>
<b>The Kids' Science Museum of Photons</b>	<b>65</b>
<b>Appendix</b>	<b>79</b>



## はじめに

本年報では、関西光科学研究所（以下、関西研）において 2018 年度に実施した研究開発の主だった成果を紹介しています。関西研は国立研究開発法人量子科学技術研究開発機構（以下、量研）の研究開発拠点であり、けいはんな学研都市にある京都府木津地区と兵庫県播磨地区の 2 か所に研究サイトを持っています。そこでは、研究系職員約 80 名及びそれを支える技術系・事務系スタッフを含めて総勢約 150 名のスタッフが、量研における関西研のミッションである「レーザーや放射光による光科学技術の研究開発」を推進しています。木津地区では、世界トップレベルの高強度レーザー技術を基盤としたレーザー加速や X 線発生等のレーザー駆動の新しい放射線源開発、レーザーの短パルス性を活かした超高速計測技術開発、そして放射線影響や創薬に資する量子生命科学の最先端の研究開発を実施しています。また、播磨地区では、大型放射光施設 SPring-8 の 2 本の専用ビームラインと計算機シミュレーションを活用することで、新しい放射光 X 線利用技術開発と物質材料科学の最先端研究を展開しています。

量研関西研として 3 年が経ち、新しい組織の中で優れた研究成果が生まれ始めています。木津地区のレーザー科学分野においては、J-KAREN レーザーの光学素子の配置を見直すことによるパルスコントラストの改善や、レーザー加速による GeV 級の準単色電子ビーム生成やプラズマからの高次高調波を用いた極短パルス X 線発生に成功するなどの成果を挙げるとともに、生命科学分野においては、遺伝子の転写制御メカニズムにおける DNA の物理化学的な役割を解明する等の新たな知見が生まれています。また、播磨地区においても、放射光 X 線を用いた鉙物マダイトの機能発現機構の解明や X 線自由電子レーザー-SACLA を用いた世界最短波長の超蛍光の観測など、数多くの優れた成果を挙げています。さらに、光技術の社会実装の観点からは、非侵襲血糖値測定技術やレーザーによるトンネル検査技術の実用化に向けた取組を引き続き行っています。

関西研は、「光」を通じた我が国の量子科学技術の発展とイノベーション戦略に貢献する開かれた研究拠点としての役割を果たすべく、今後とも職員一同、より一層努力してまいります。皆様のご理解・ご協力を宜しくお願い申し上げます。

2019 年 4 月 8 日  
関西光科学研究所  
所長 河内 哲哉



## Preface

This annual report from Kansai Photon Science Institute (KPSI) provides highlights of the scientific and technical researches that were conducted over the 2018 fiscal year.

KPSI was reconstituted in April 2016 as one of the research and development (R&D) bases of National Institutes for Quantum and Radiological Science and Technology (QST). At KPSI's two R&D sites, the Kizu site in Keihanna Science City in Kyoto Prefecture and the Harima site in Hyogo Prefecture, there are about 150 staff, comprising around 80 researchers and the technical and administrative staff who support them. We promote the R&D of optical science and technology using lasers and synchrotron-radiation X-rays, which is the mission of KPSI in QST. At the Kizu site, we are conducting state-of-the-art research for developing new-type laser-driven radiation sources such as laser accelerated particle beam and ultrashort X-rays based upon world-leading top-class high-intensity laser technology, ultrafast measurement methodology using ultrashort pulse technology, and quantum life science that helps us understand radiation effects and develop new medicines. At the Harima site, using two contract beamlines of SPring-8 and computer simulation, we are developing new technology to utilize synchrotron radiation X-rays and carrying out state-of-the-art research in material science.

Three years have passed since the restart of KPSI in QST, and several outstanding results are being produced. In the laser science field at the Kizu site, the pulse contrast of the J-KAREN laser is substantially improved by reviewing the arrangement of the optical elements, and we have succeeded in generating GeV class quasi-monochromatic electron beam by laser acceleration and ultrashort X-rays generation using higher-order harmonics from relativistic plasma. In the field of the life science, new findings emerged such as elucidating the physicochemical role of DNA in the transcriptional control mechanism of genes. At the Harima site, we also obtained several excellent results such as discovering the functional expression mechanism of mineral magadiite using synchrotron radiation X-rays and the observation of the shortest wavelength super fluorescence using the X-ray free electron laser SACLA. In addition, regarding the social implementation of optical technology, we are making efforts toward practical application of non-invasive blood glucose measurement and laser based tunnel inspection technology.

KPSI will continue to fulfill our role as an open research center of "science of light" and will contribute to quantum science and technology and the strategy for innovation in Japan. We appreciate your understanding and cooperation.

8<sup>th</sup> April, 2019  
Director General of KPSI  
Tetsuya KAWACHI

## Activities of KPSI

## 関西光科学研究所の主な動き

### シンポジウム・研究会等の開催

5月8日～9日 「光・量子ビーム科学合同シンポジウム 2018」  
関西研多目的ホール棟（京都府木津川市） 大阪大学と量研との間で締結された包括協定に基づき、関西研と大阪大学レーザー科学研究所の連携協力体制をより強固なものにし、光・量子ビーム科学分野の研究開発を加速することを目的として、合同シンポジウムを開催しました。



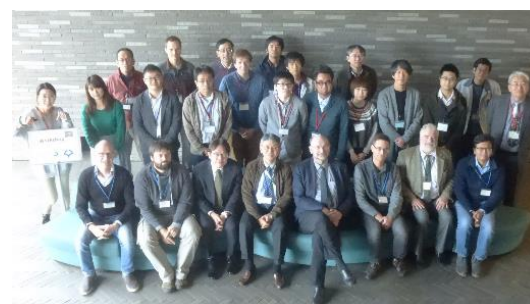
6月6日～8日 「第34回化学反応討論会」 関西研多目的ホール棟（京都府木津川市） 化学反応速度論および動力学に関連する幅広い分野の研究者が一堂に会し、励起状態の生成と緩和を含む化学反応に関する新しい知見、それらの応用研究に関する最先端の実験および理論について討論を行いました。招待講演、口頭発表、ポスター発表を通して、3日間に渡り討論を行い、展示企業9社を含む約150名の方々が参加しました。



11月26日～29日 「The 8th Asian Summer School & Symposium on Laser Plasma Acceleration and Radiation (ASSS-8)」 関西研多目的ホール棟（京都府木津川市）、奈良春日野国際フォーラム“麓”（奈良県奈良市） ASSSは51名（講師10名含む。中国、韓国、ネパール、日本、スペイン、イギリス、ロシア、チェコ、ドイツ、米国）の参加者での開催となりました。3日目、4日目は第2回QST国際シンポジウムと合同で行いました。



11月27日 「ドイツHZDR・阪大ILE・KPSI-QST第2回ワークショップ」 関西研木津地区（京都府木津川市）HZDR（ドイツ）および大阪大学レーザー科学研究所（阪大ILE）と合同で高エネルギー密度科学や高強度レーザーに関するワークショップを開催し、情報交換を行いました。



11月28日～29日 「第2回QST国際シンポジウム」 奈良春日野国際フォーラム“麓”（奈良県奈良市） 高強度レーザーが切り拓く新たな光・量子科学技術をテーマに、第2回QST国際シンポジウムを開催し、251名の参加者が集いました。高強度レーザー開発とその応用に関わる幅広い研究分野で活躍している国内外の研究者を招待し、高強度レーザーが切り拓く光・量子科学技術の最先端研究に係るQST国際シンポジウムを開催したことで、世界の潮流をとらえるとともに、QSTのプレゼンスを高めることができました。





12月6日～7日 「レーザー応用技術産学官連携成果報告会」福井大学附属国際原子力工学研究所（福井県敦賀市） 原子力機構と量研の間で平成28年度に締結された「レーザー技術の開発及び普及の推進」に関する覚書に基づき、レーザー応用技術・産学官連携成果に関する報告会を開催しました。

3月1日 「QST 放射光科学シンポジウム 2019/微細構造解析プラットフォーム第3回放射光利用研究セミナー」大型放射光施設 SPring-8 放射光普及棟大会議室（兵庫県佐用町） 関西研放射光科学研究センター、文部科学省ナノテクノロジープラットフォーム QST 微細構造解析プラットフォームの主催で、QST 放射光科学シンポジウムを開催しました。センターの職員のみならず、外部の第一線の共同研究者も交えて、先端的放射光利用技術の開発、物質・材料の研究、次世代放射光施設で期待される軟 X 線放射光を利用した研究などについての講演が行なわれ、ナノテクノロジープラットフォーム事業の推進に資する講演会となりました。

### SPRING-8 のイベント

4月29日に第26回 SPring-8&SACLA 施設公開が開催され、関西研は専用ビームライン（BL11XU と BL14B1）を公開し、講義授業及び展示実験等を行いました。今年は絶好の好天に恵まれ、理研の広報も行き届き、過去最高記録を大幅に更新する 10,672 名もの参加者がありました。

7月8日～11日に第18回 SPring-8 夏の学校が開催され、関西研は 11 の主催団体の一つとして貢献しました。次世代の放射光利用研究者の発掘と育成を目的として、関西研では、主としてビームライン 14B1 における実習（放射光を利用した高温高圧合成）を実施しました。



### 関西光科学研究所（木津地区）施設公開

10月28日に関西光科学研究所（木津地区）の施設公開を開催しました。昨年度は台風の影響でやむを得ず中止となりましたが、今年度は天候にも恵まれ 1,104 名の方々にお越しいただきました。世界トップクラスの高強度レーザー施設の見学や、光の実験ショー、工作教室などに加え、高崎量子応用研究所からのブース出展もあり、ご来場いただいた皆様にはご好評をいただきました。



## レーザー打音検査装置の社会実装試験

内閣府が主導する戦略的イノベーションプログラム（SIP）の支援を受けて、トンネルコンクリートの内側の欠陥を遠隔・高速に検査する技術の共同開発の一環として、社会実装試験を行いました。今年度は、学研都市推進機構からのご紹介で、5月に奈良市、6月に大阪府の道路トンネルを試験場として提供して頂き、実際のトンネル現場での実証試験を行いました。また12月には、関西研から400km離れた静岡県尾崎トンネルまで自走で移動しての実証試験に成功しました。梅雨の最中の日々刻々と変化する天候の中で装置を稼働させた経験や、遠距離移動を伴うレーザー打音検査装置の運用試験を実施できたことは、実用化への大きな自信となりました。



## 木津地区の主な出展イベント

2018年度も積極的にアウトリーチ活動を実施しました。きつづ光科学館ふおとの年間来場者は昨年度を上回り48,000人を達成しました。

4月8日「第41回花と緑の見学会」出展 高崎量子応用研究所（群馬県高崎市）

7月28日～29日「青少年のための科学の祭典2018全国大会」出展 科学技術館（東京都千代田区）

8月2日～3日「夏休み2018宿題自由研究大作戦」出展 インテックス大阪（大阪府大阪市住之江区）

10月4日～5日「京都スマートシティエキスポ2018」出展 けいはんなオープンイノベーションセンター（京都府相楽郡精華町）

10月4日～5日「第13回けいはんなビジネスメッセ2018」出展 けいはんなプラザ（京都府相楽郡精華町）

10月25日～27日「けいはんな情報通信フェア2018」出展 けいはんなプラザ（京都府相楽郡精華町）



## 受賞ラッシュ

平成30年春の褒章 「紫綬褒章」 小池雅人客員研究員（光量子科学研究部）

平成30年秋の叙勲 「瑞宝中綬章」 加藤義章先生（元関西研所長）

2018年ノーベル物理学賞 CPA(チャープドパルス増幅)技術 関西研設立に際しご助言頂くなど 関西研と関わりの深い Gérard Mourou（ジェラルド ムルー）先生

2018年チャンドラセカール賞 田島俊樹先生（元関西研所長）

アメリカ物理学会 2019年 Robert R. Wilson 賞 田島俊樹先生（元関西研所長）



加藤 義章 先生 平成30年秋の叙勲 瑞宝中綬章 受賞記念講演会・祝賀会 (H31.3.30 ホテルグランヴィア京都)

# User Facilities



## 主要な施設・装置

### 木津地区

#### ○J-KAREN レーザー装置

##### 【装置概要】

世界トップクラスの極短パルス超高強度レーザーです。30J のレーザーエネルギーを 30 フェムト秒（1 フェムトは 1000 兆分の 1）の時間に閉じ込めることにより 1000 兆ワットの超高強度を実現します。

（右の写真は強力な励起レーザーの光で緑色に光っています。）

##### 【装置性能】

- ・照射エネルギー：30 J/pulse
- ・コントラスト比： $10^{-12}$
- ・波長：800 nm
- ・繰り返し：0.1 Hz
- ・パルス幅：30 フェムト秒
- ・集光強度： $10^{22}$  W/cm<sup>2</sup>

##### 【主要な研究課題】

レーザーの高度化技術の開発、イオンおよび電子のレーザー加速技術の開発、高エネルギーコヒーレント X 線の発生等



#### ○X 線レーザー実験装置

##### 【装置概要】

強力なレーザーで作ったプラズマを使って発振する X 線のレーザーです。目に見える光に比べて発振波長が短く、さらにほんの一瞬の短い間しか光らないという特徴を生かして、固体表面で起こる物性現象の変化の様子を観察等に利用しています。

##### 【装置性能】

- ・照射エネルギー：1  $\mu$ J/pulse
- ・波長：13.9 nm
- ・繰り返し：0.1 Hz
- ・パルス幅：約 10 ピコ秒

##### 【主要な研究課題】

軟 X 線光学素子の評価、フェムト秒レーザーアブレーションの機構解明



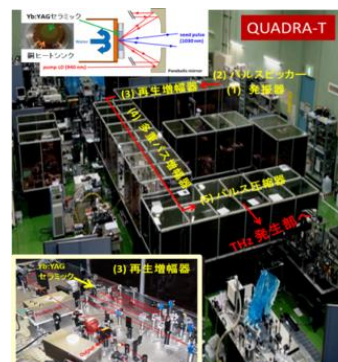
#### ○QUADRA-T レーザーシステム

##### 【装置概要】

1 秒間に 1000 発のレーザーパルスが繰り返せる高平均出力ピコ秒パルスレーザーです。中心周波数 0.3THz の高強度テラヘルツパルスを発生することが可能です。

##### 【装置性能】

- ・照射エネルギー：10 mJ/pulse
- ・波長：1030 nm





- ・繰り返し：1 kHz
- ・パルス幅：約 1 ピコ秒

#### 【主要な研究課題】

高繰り返し高出力レーザー（パラメトリック増幅器等）の開発、高強度テラヘルツ光源の開発

## 播磨地区

播磨地区では大型放射光施設 SPring-8 に 2 本の QST 専用ビームラインを設置しているほか、日本原子力研究開発機構（JAEA）の専用ビームラインにも複数の放射光専用実験装置を常設しています。一方で、QST 専用ビームラインにも、JAEA の専用実験装置が常設されています。

### ○BL11XU（QST 極限量子ダイナミクス I ビームライン）

#### 【装置概要】

SPring-8 標準の真空封止アンジュレータを光源とし、マルチ結晶交換システムを装備することで、広範囲のエネルギー領域の高輝度放射光 X 線を高効率に利用できるビームラインです。

#### 【装置性能】

- ・光源：真空封止アンジュレータ
- ・エネルギー領域：6～70 keV
- ・分光結晶：Si(111)、Si(311)
- ・実験装置：放射光メスバウアー分光装置、共鳴非弾性 X 線散乱装置、及び表面 X 線回折計

##### 1. 放射光メスバウアー分光装置

$^{57}\text{Fe}$ 、 $^{61}\text{Ni}$  等のメスバウアー核種を対象とした放射光メスバウアー分光が可能で、物質の電子、磁気状態から格子振動状態に関する情報などを得ることができます。

##### 2. 共鳴非弾性 X 線散乱装置

2m 長アームに搭載した球面湾曲型集光式アナライザー結晶による背面反射を用いることで、高分解能の X 線分光を行い、散乱光の方位や入射光とのエネルギー差から、運動量移行を伴う固体内素励起が観察できます。

##### 3. 表面 X 線回折計

分子線エピタキシー（MBE）チェンバーを搭載した表面構造解析用装置で、窒化物を含む半導体結晶などの成長過程を、X 線回折法を用いてその場観察・リアルタイム観察することができます。

#### 【主要な研究課題】

金属薄膜の原子層単位での磁性探査、白金系燃料電池触媒の電子状態解析、半導体量子ドットや半導体多層膜の成長過程のリアルタイム解析



### ○BL14B1（QST 極限量子ダイナミクス II ビームライン）

#### 【装置概要】

偏向電磁石を光源とすることで、連続スペクトルを持つ白色 X 線や高エネルギーの単色 X 線が利用可能なビームラインです。全反射ミラーや分光結晶の曲げ機構によって、試料位置への集光が可能となっています。

## 【装置性能】

- ・光源：偏向電磁石
- ・エネルギー領域：白色 X 線（5～150 keV）、単色 X 線（5～90 keV）
- ・実験装置：高温高压プレス装置、分散型 XAFS 測定装置（JAEA）及び  $\kappa$ （カッパー）型回折計（JAEA）

### 1. 高温高压プレス装置

高温高压の条件下にある試料を、白色 X 線を用いたエネルギー分散型 X 線回折法やラジオグラフィ法、単色 X 線を用いた XAFS（X 線吸収微細構造）法や角度分散型 X 線回折法によって調べることができます。



## 【主要な研究課題】

高压下での金属水素化物形成過程のその場観察

## ○BL22XU（JAEA 専用ビームライン）における放射光専用実験装置

### 1. 単色 X 線実験用高温高压プレス装置（JAEA BL22XU）

高温高压下（到達圧力 10 GPa（10 万気圧）、到達温度 2000 K 程度）の X 線回折測定や X 線吸収法を用いた密度測定、室温、1 MPa 未満の水素ガス雰囲気中でのその場 X 線回折観察、時分割 X 線回折測定が可能な装置です。



### 2. ダイヤモンドアンビルセル回折計（JAEA BL22XU）

大型イメージングプレート検出器と高エネルギー X 線を利用することにより、高压下での単結晶 X 線回折及び粉末 X 線回折実験、X 線全散乱測定及び原子二体分布関数（PDF）解析が可能な装置です。



### 3. 大型 X 線回折計

共鳴 X 線散乱による電子軌道状態の観測、スペックル回折によるドメイン構造の研究、応力・歪み分布測定などの回折マッピングなど多目的に利用する四軸回折計です。

## 【主要な研究課題】

水素貯蔵合金の水素吸蔵過程の時分割その場 X 線回折測定、負の熱膨張材料、超伝導体、f 電子系化合物、コヒーレント X 線を利用したスペックル散乱によるナノドメイン観察。応力・歪みの 3 次元分布測定、等

## 施設の稼働実績

### ○木津地区

#### 実施課題件数

装置名称	独自研究	受託研究	共同研究	施設共用
J-KAREN レーザー装置	2	2	0	2
X 線レーザー実験装置	0	1	5	1
QUADRA-T レーザーシステム	1	0	0	0
kHz チタンサファイアレーザー	3	0	4	0
X 線回折装置	1	0	1	0
軟 X 線平面結像型回折格子	0	0	1	0

## ○播磨地区

2018年度のSPring-8蓄積リングの運転時間は約5230時間で、放射光利用時間はそのうちの約4600時間でした。量研、原子力機構とも専用ビームラインでは10～20%弱程度の調整時間を除き、放射光利用時間で独自研究や受託研究、外部利用者への施設共用と研究支援を行っています。

### 実施課題件数

ビームライン	独自研究	受託研究	共同研究	施設共用
BL11XU	8	0	11	20
BL14B1	12	0	1	7
BL22XU	5	0	5	12

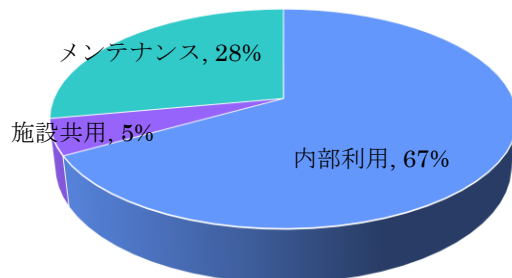
### 利用日数

ビームライン	独自研究	受託研究	共同研究	施設共用
BL11XU	79	0	78	53
BL14B1	56	0	3	19
BL22XU	35	0	34	32

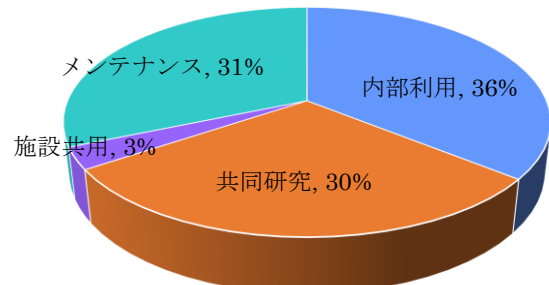
## 施設の利用状況

### ○木津地区

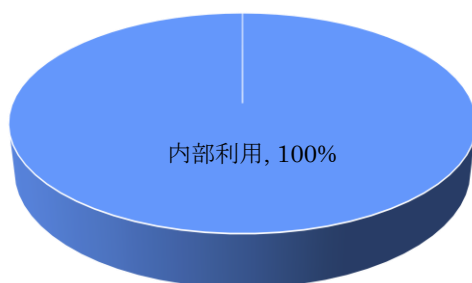
J-KAREN レーザー装置  
(合計ビームタイム：1612 時間)



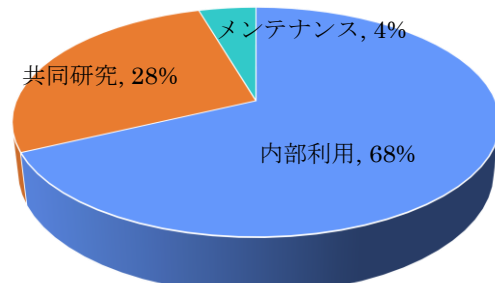
X 線レーザー実験装置  
(合計ビームタイム：1597 時間)



QUADRA-T レーザー装置  
(合計ビームタイム：178 時間)

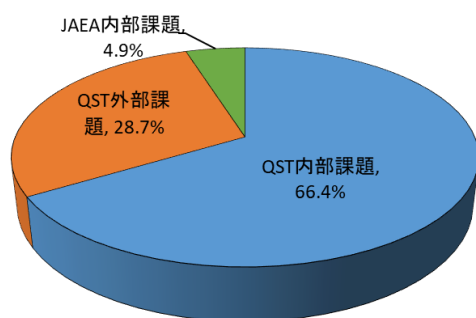


その他装置（木津地区）  
(合計ビームタイム：1565 時間)

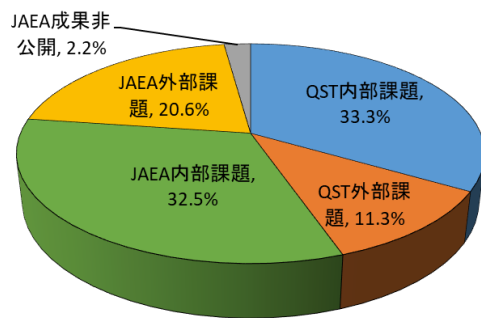


### ○播磨地区

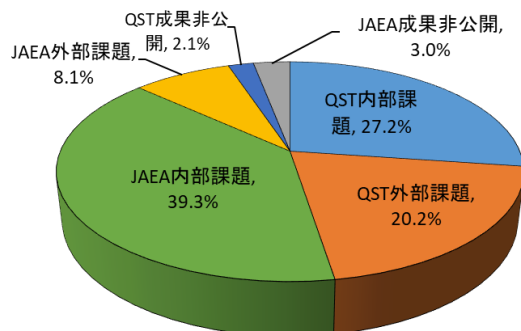
QST極限量子ダイナミクス I ビームライン(BL11XU)



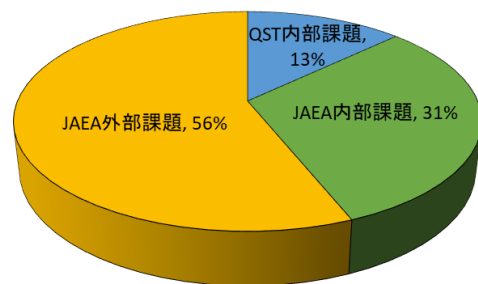
QST極限量子ダイナミクス II ビームライン(BL14B1)



JAEA重元素科学 I ビームライン(BL22XU)



JAEA重元素科学 II ビームライン(BL23SU)



# Research Highlights

# R & D for Advanced Photon Research

Kiminori Kondo (Director)

Department of Advanced Photon Research

In the department of Advanced Photon Research, the base of the research is the science and technology of advanced lasers. In particular, high-peak-power laser technology, high-repetition-rate and high-stability laser technology, and ultrashort-pulse technology are the most important. We develop these technologies in-house and apply them to various objects. The largest laser system in KPSI is the Petawatt (PW)-class high-peak-power laser J-KAREN-P. This system has been upgraded since obtaining the supplementary budget in FY2012. The long commissioning operation term was completed in the last fiscal year. Therefore, from this fiscal year, not only internal users in KPSI, but external users have also started to use the system in PW-class operation mode. The restart of the external user mode for J-KAREN-P should be emphasized here. The extreme focused intensity of  $10^{22}$  W/cm<sup>2</sup> on target with extremely high-contrast suppression of the proceeding optical component to the main pulse is now available. This extreme status of our high-power laser infrastructure is maintained by the laser facility operation office, advanced laser group, and high-intensity laser science group. In particular, the advanced laser group not only maintains J-KAREN-P to deliver the laser pulse with the best condition, but also develops and introduces new technology to maintain the condition of J-KAREN-P as world-leading class. High-intensity laser science group mainly studies laser-driven ion acceleration, laser electron acceleration, and relativistic high-order harmonic generation with J-KAREN-P in KPSI.

One of the most important applications is the development of a laser-driven secondary radiation source. An extremely high optical field can be formed with focusing extremely high peak

power to an ultimately small spot size. Atoms and molecules exposed to this extremely high field are immediately ionized by field ionization. Actually, the corresponding optical intensity to the atomic unit is only  $3 \times 10^{16}$  W/cm<sup>2</sup>, which is much lower than that to be generated with J-KAREN-P. The generated free electrons move along the extremely high optical field, then the ultra-relativistic quiver motion is induced. These energetic quivering electrons induce the generation of various secondary radiations. This means that there is a possibility of a compact energetic quantum beam source without conventional accelerator technology. If this technology is established and applied to various fields, a type of destructive innovation could occur. For example, one of the most important applications of a laser-driven secondary radiation source is the application to Quantum Scalpel, which is a new-generation heavy-ion cancer therapy machine planned to be developed by 8 years from now. Quantum Scalpel is the one of the main projects in QST. The injector part of Quantum Scalpel is based on the laser-driven carbon accelerator. The JST-MIRAI R & D program (large-scale type) started in Nov. 2017. The aim of this program is show a proof of concept. Not only ion accelerator, but laser plasma electron accelerator is also under development in KPSI, with this MIRAI program by JST and ImPACT program by the cabinet. Moreover, not only charged particle acceleration, but X-rays are also generated with ultrashort high-peak-power lasers. Burst intensification by singularity emitting radiation (BISER) is the new laser-driven coherent X-ray generation scheme, which has been invented by KPSI. Usually high-order harmonics are generated from the outermost bound electrons in atomic and molecular systems in a sufficiently high optical field. Therefore, the quiver energy is limited even

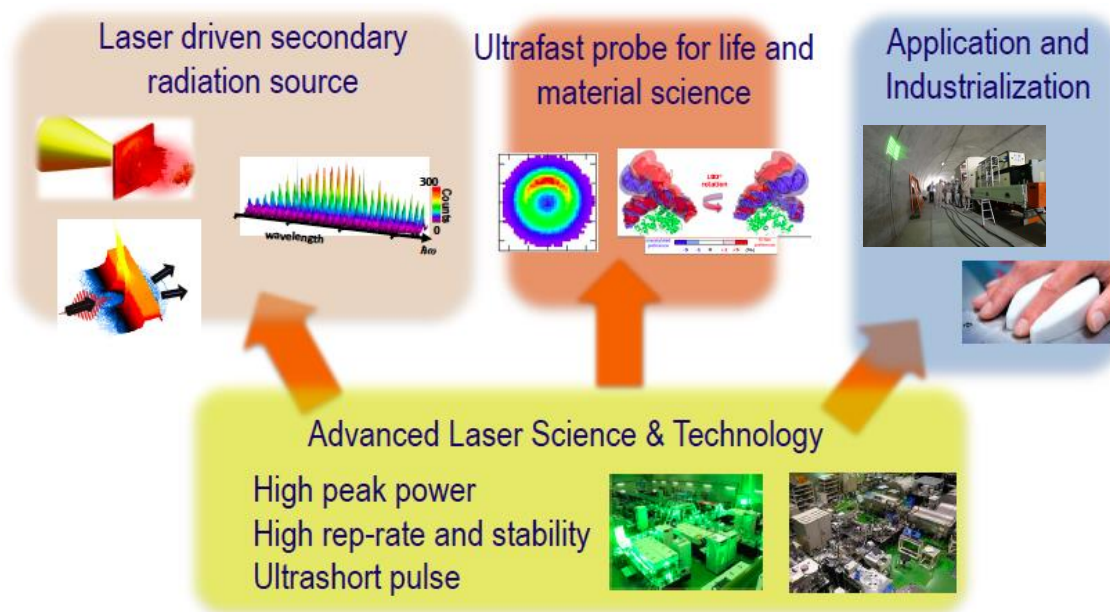


Fig. 1 Research and development of department of Advanced Photon Research

with using an IR pump laser for taking higher quiver energy in the same interaction intensity. However, BISER is emitted by the oscillation of a high-density electron bunch formed by a laser wakefield. Then, in principle, there is no limit on the quiver energy of electron bunch oscillation. There is a possibility of a keV-scale coherent X-ray source without using a gigantic linac like such as SACLA. These secondary radiation sources driven by ultrashort high-peak-power lasers are under research mainly by the high-intensity laser science group and the advanced laser group.

The next important application of our advanced laser science and technology is an ultrafast probe for life and material science. In particular, for material science, not only an ultrashort probe, but THz radiation is also developed, mainly in the ultrafast dynamics group. Until the last fiscal year, the C-Phost project has been performed by the ultrafast dynamics group. Strong THz radiation is generated with a kHz 10-mJ ps laser system, QUADRA-T. These radiation and laser systems are used for various ultrafast dynamics research. For life science applications, a bright and stable short pulse laser system has been developed and applied to the two-photon microscope for observing the neuron dynamics in mouse brain at NIRS. This research began to demonstrate one of the featured results by the unification of NIRS and JAEA two years ago. In this fiscal year, a deeper part was successfully obtained with the developed bright laser system than that with the commercially based system. Recently, the ultrashort probe could be upgraded to the attosecond regime to start attosecond science in KPSI. Not only attosecond science, but the related study of CPS laser fabrication also has been started. These studies are supported by the Q-LEAP program, which has started from this fiscal year and could continue for 10 years. This project will be studied by the ultrafast dynamics group and X-ray laser group. The X-ray laser group studies the interaction between intense X-rays and solid materials with the laser-plasma-based X-ray laser at KPSI and SXFEL at SACLA. The intense X-ray fabrication technology is an important fine structure fabrication technology, which has advanced to current laser fabrication technology. The repetition rate of the present X-ray laser system in KPSI is only 0.1 Hz, whereas it is 60 Hz in SACLA. Then, the X-ray laser group will shut down the present X-ray laser system and will upgrade it to a 10 to 100-Hz system based on a Ti:sapphire laser technique in the near future.

In a sense, the most important application of our advanced laser science and technology is industrialization. In fact, this fiscal year is the final fiscal year for the SIP program by the cabinet for the development of nondestructive tunnel inspection technology. This technology is tried to apply to commercial technology for making the venture company. One of the key technologies of the nondestructive tunnel inspection technology is the high-average-power high-repetition-rate intense laser technology. This technology is used for hitting the inner surface of the concrete tunnel to induce an acoustic wave inside the wall. To induce an acoustic wave of sufficient amplitude, a 5-J per pulse with 50-Hz repetition rate system has been developed and successfully loaded on an inspection vehicle. This system has been successfully demonstrated in a real tunnel. The impression of the general people was very high, and there was much press coverage related to this technology in this fiscal year. This technology is closely related to the development of high-average-power high-peak-power laser systems, which could be used in the laser-driven carbon ion injector in Quantum Scalpel.

In this annual report, some topical studies are introduced from recent results published in several journals. From the high-intensity laser science group, the physics related to the flying

mirror are shown by Dr. Koga. Dr. Kai reports on a unique diagnostic study on electron bunches in a laser wakefield. This study is performed under the ImPACT program which will finish within this fiscal year. From the advanced laser group, Dr. Sagisaka reports on high-order harmonics and proton generation from a thin foil irradiated by an extremely high optical field. Dr. Fukuda shows his unique laser acceleration study of pure proton acceleration using a hydrogen cluster target. From the X-ray laser group, Dr. Imazono reports a flat-field grating spectrometer for the tender X-ray region. Dr. Ishino discusses the damage generation with intense picosecond X-rays. From the ultrafast dynamics group, Dr. Otake shows an analytical model of electron excitation in dielectrics in high field. Dr. Itakura explains his unique ultrafast measurement scheme using plasma reflection.



# Relativistic Flying Mirrors Generating Upshifted Higher Harmonic Generation

James K. Koga

High-Intensity Laser Science Group, Department of Advanced Photon Research

Horseshoe bats use echolocation to determine their position and because their emitters (nose) and receivers (ears) are both moving, they experience the double Doppler effect [1]. Figure 1 shows a schematic of this. They also dynamically lower their emitting frequency to keep the reflected signal within a frequency

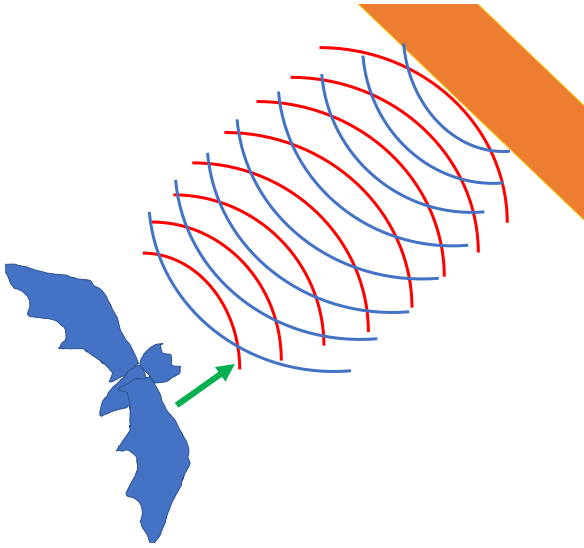


Figure 1. Bat using the double Doppler effect

range [1]. This double Doppler effect can also occur with light. In his paper on special relativity, Einstein described the upshift of electromagnetic radiation from a relativistically moving mirror [2]. However, a large amount of energy is necessary to accelerate a macroscopic object to relativistic velocities, such as shown in the NASA starlight program [3]. Because lasers propagating in plasma at nearly the speed of light can generate plasma waves, it was proposed to use breaking plasma waves as relativistic mirrors to reflect, compress, and upshift laser light [4]. This concept has been shown to work theoretically [4], numerically [5], and experimentally [6–9] (see also review [10]). However, until now the laser pulse reflecting off the relativistic mirror has been chosen to be of sufficiently low intensity that the energy of the reflected pulse is far below the energy stored in the wake wave, such that the mirror is not significantly perturbed [11]. In this work we considered strong laser pulses and how they would reflect off of relativistically moving plasma waves [12]. We were motivated by the fact that obtaining and using high-intensity light with high frequencies and short wavelengths is of interest not only for applications, but also from a fundamental point of view [13,14].

In order to investigate the possibility of using strong laser pulses reflecting off relativistic flying mirrors, we performed numerical calculations via one-dimensional particle-in-cell (PIC) simulations using the code EPOCH [15]. The simulations consisted of two counter-propagating laser pulses colliding in an underdense plasma. One high-intensity laser was used to generate

the breaking plasma wave (driver) and the other laser was used to reflect off of the relativistic flying mirror (source). Owing to the large upshift factor, the source laser had a wavelength longer than the driver pulse to allow resolution of the expected short wavelength reflected radiation within reasonable simulation sizes [12]. We found that source pulses with intensities even near the relativistic regime could be reflected off the relativistic flying mirrors [12]. In the best case of the considered simulations, harmonics of the upshifted source pulse were observed and wavelengths up to  $\sim 160$  times shorter than the original source pulse were generated [12]. Figure 2 shows a schematic of the interaction, in which the driver laser and source laser collide in an underdense plasma and a portion of the source pulse is reflected, upshifted, and compressed by the breaking plasma wave, i.e., the relativistic flying mirror. The details can be found in [12].

In the future, with higher-dimensional scenarios, we will investigate the focusing of the reflected source pulses and will consider using them for electron–positron pair creation with several focused laser pulses [16].

## Acknowledgments

This work was performed with Sergei V. Bulanov, Timur Zh. Esirkepov, Masaki Kando, Stepan S. Bulanov, and Alexander S. Pirozhkov. This work was supported by JSPS KAKENHI Grant Number JP16K05639 and by the project High Field Initiative (CZ.02.1.01/0.0/0.0/15\_003/0000449) from the European Regional Development Fund. SSB acknowledges support from the Office of Science of the US DOE under Contract No. DE-AC02-05CH11231. The simulations were performed on the “SGI ICE X” supercomputer at the Tokai Research and Development Center of the Japan Atomic Energy Agency.

## References

1. Biophysics, edited by W. Hoppe, W. Lohmann, H. Markl, and H. Ziegler, Springer-Verlag, Berlin 1983.
2. A. Einstein, *Ann. Phys.*, Lpz. 322 891 (1905).
3. N. Kulkarni, P. Lubin, and Q. Zhang, *The Astronomical Journal* **155**, 155 (2018).
4. S. V. Bulanov, I. N. Inovenkov, V. I. Kirsanov, N. M. Naumova and A. S. Sakharov, *Sov. Phys.—Lebedev Inst. Rep.* **6**, 9 (1991).
5. S. V. Bulanov, T. Zh. Esirkepov and T. Tajima, *Phys. Rev. Lett.* **91**, 085001 (2003).
6. M. Kando, et al., *Phys. Rev. Lett.* **99**, 135001 (2007).
7. A. S. Pirozhkov, et al., *Phys. Plasmas* **14**, 123106 (2007).
8. M. Kando, et al., *Phys. Rev. Lett.* **103**, 235003 (2009).
9. A. S. Pirozhkov, et al., *AIP Conf. Proc.* **1153**, 274 (2009).
10. S. V. Bulanov, T. Zh. Esirkepov, M. Kando, A. S. Pirozhkov and N. N. Rosanov, *Phys. Usp.* **56**, 429 (2013).
11. A. S. Pirozhkov, S. V. Bulanov, T. Zh. Esirkepov, A. Sagisaka, T. Tajima and H. Daido, *Intensity Scalings of Attosecond*



- Pulse Generation by the Relativistic-irradiance Laser Pulses, in *Ultrafast Optics V* (Berlin: Springer) 265 (2007).
12. J. K. Koga, S. V. Bulanov, T. Zh. Esirkepov, M. Kando, S. S. Bulanov and A. S. Pirozhkov, *Plasma Phys. Control. Fusion* **60**, 074007 (2018).
  13. T. Yamaji, et al., *Phys. Lett. B* **763**, 454 (2016).
  14. J. K. Koga and T. Hayakawa, *Phys. Rev. Lett.* **118**, 20480 (2017).
  15. T. D. Arber, et al., *Plasma Phys. Control. Fusion* **57** 113001 (2015).
  16. S. V. Bulanov, et al., *Nucl. Instrum. Methods Phys. Res. A* **660**, 31 (2011).

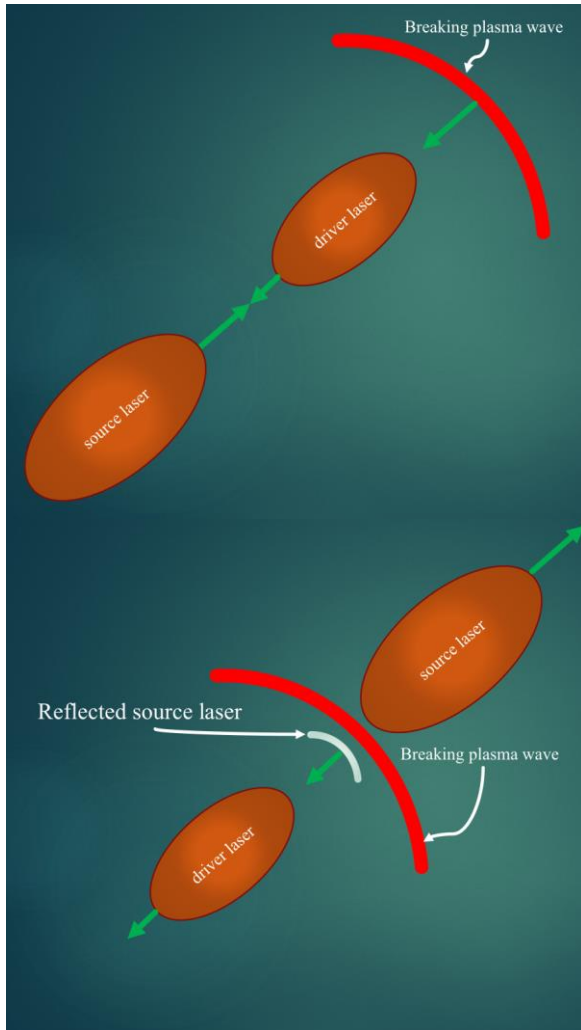


Figure 2. Driver laser creating breaking plasma wave, relativistic flying mirror, and counter-propagating source laser in a background underdense plasma (upper figure). Part of the source laser is reflected off the breaking plasma wave (relativistic flying mirror), upshifted, and compressed (lower figure).

# Introducing the electro-optic spatial decoding technique into laser wakefield acceleration

Kai Huang and Masaki Kando

High Intensity Laser Science Group, Department of Advanced Photon Research

Laser wakefield acceleration (LWFA) [1] has been studied intensively owing to its inherent ultrashort and ultrahigh-acceleration gradient characteristics. By using an ultrashort and ultra-intense laser pulse ( $10^{18}$  W/cm<sup>2</sup>) from chirped pulse amplification (CPA) [2], a large-amplitude plasma wave can be produced in underdense plasma, allowing the electron bunch to be accelerated to GeV range over centimeter-scale distances. Secondary X-ray sources from such electron bunches by undulators [3] or betatron [4] oscillations are considered to have potential applications in the ultrafast X-ray pump-probe studies.

Because X-ray photons are emitted by electron bunches, the emission timing and pulse durations of the X-ray sources are directly determined by the temporal characteristics of the electron bunches. The electrons from LWFA are always assumed to be injected into the first bucket just after the drive laser pulse. Thus, “jitter-free” or relatively small jitter were always considered to be the merits of LWFA. Yet, the emission timings of the electrons have to date never been experimentally measured. For a plasma wave in linear mode, the ambient electrons could be trapped randomly into a certain wave bucket. The possibility that electron bunches could have jitter cannot be ignored.

The durations of the electron bunches from LWFA have been determined by the analyzing the coherent transition radiation [5] produced when an electron passes through a metal foil or plasma boundary. A bunch duration of 1.7 fs (rms) has been reported in the literature. However, those detections either lack single-shot capabilities or sacrifice electron bunch quality for lateral applications. What’s more, they didn’t show the capabilities to real-time observing the emission timings of the electron bunches.

For single-shot nondestructive detection of the electron temporal profiles, we choose to introduce the electro-optic (EO) spatial decoding technique into LWFA. When an electron bunch passes by an EO crystal, the Coulomb field of the electron bunch induces birefringence to the probe laser that is simultaneously incident through the EO crystal. By setting an angle  $\theta_p$  between the probe laser and electron beam propagation directions, the longitudinal profiles of the electron bunches are encoded transversely to the probe laser profile with a temporal mapping relationship:  $c\Delta\tau = \Delta\xi \tan \theta_p$  [6], where  $c$  is the speed of light,  $\Delta\tau$  is the timing difference, and  $\Delta\xi$  is the signal displacement observed on the CCD. Such a relationship is simply achieved by considering that the Coulomb field of a relativistic electron is compressed along the direction perpendicular to its direction of motion in free space.

An experiment has been performed using the JLITE-X laser in Kansai Photon Science Institute. The laser pulse in the interaction chamber has a duration of 40 fs (FWHM) and power < 10 TW. The laser was focused by an F/20 off-axis-parabola (OAP) to a supersonic gas jet for relativistic electron beam generation. Initially, we positioned the EO crystal 1.5 m away to avoid damage to the crystal by the transmitted drive laser. Unfortunately, owing to the divergence, pointing fluctuation, and longitudinal elongation of the electron beams, we did not observe the EO signal at such positions. This problem was solved by

setting the crystal very close to the gas nozzle and outside of the drive laser emission cone, as shown in Fig. 1. The detection point is at (2.2 mm, 1.5 mm) from the exit of the nozzle. At this detection position, we succeeded in observing the EO signal of the electron bunches.

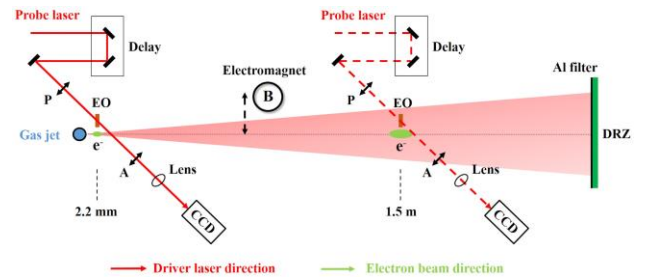


Figure 1: Experimental setup. “P” and “A” denote a pair of polarizers with polarization directions orthogonal to each other. A GaP crystal of thickness 50  $\mu$ m was used in the detection with the  $[-1,1,0]$  crystal axis perpendicular to the electron path. The probe laser has an incident angle of  $\theta_p = 44^\circ$ .

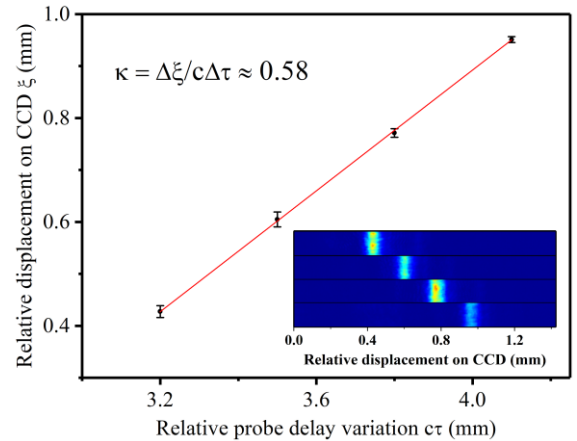


Figure 2: Temporal mapping relationship measurement. Insets are the single-shot EO signals with four different probe delay settings. Error bars denote the deviations of 20 consecutive shots.

Soon after observing the EO signals, we examined the temporal mapping relationship by checking the EO signals at four different probe settings with fixed plasma density. To our surprise, the fitted relationship was different from the widely used model, as illustrated in Fig. 2. The fitted slope was 0.58, which was much smaller than  $1/\tan \theta_p \approx 1.03$ . This inconsistency suggested that the relative angle between the Coulomb field front and the electron propagation direction was larger than  $\theta_p$ . The assumed model in which the Coulomb field is compressed orthogonally to the electron propagation direction is not applicable in our case.

In the case of LWFA, the electrons are emitted from plasma, where electromagnetic components with frequencies smaller than

the plasma eigenfrequency are shielded. When we set the EO crystal very close to the plasma source, the free space condition would not be valid anymore. An analysis on the Liénard–Wiechert potential shows that because the electromagnetic field propagates with the speed of  $c$ , the wavefront of the Coulomb field of the electron is spherical, as shown Fig. 3(a). Because the electron propagates with a speed smaller than  $c$ , when the electron is very close to the source position, the front of the field is attached to the electron. However, when the electron propagates for a long distance, the “free-space” condition becomes valid and the Coulomb field becomes perpendicular to the electron propagation direction, as shown in Fig. 3(c).

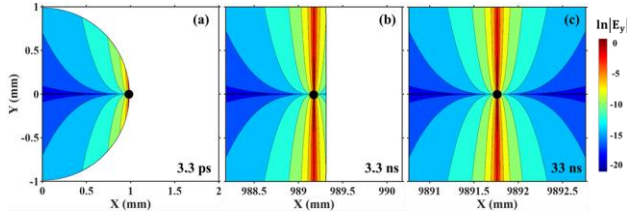


Figure 3: Static electric field analysis. The  $\ln|E_y|$  distribution of a 30-MeV electron at propagation time of 3.3 ps (a), 3.3 ns (b), and 33 ns (c). X is the electron propagation direction and Y is the transverse direction.

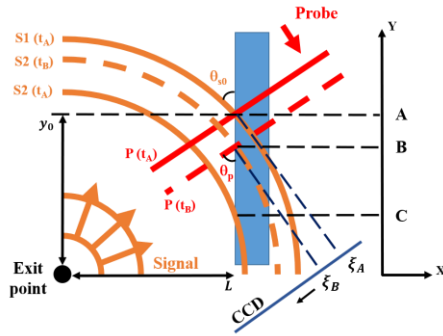


Figure 4: Geometry for the calculation of a new temporal mapping relationship. The red straight lines and brown curved lines denote the wavefront of the probe laser and the THz signal field, respectively. The THz field incident angle on the EO crystal surface at transverse position  $y$  and longitudinal distance of  $L$  from the source position is  $\theta_{s0} = \arctan(y/L)$ . The probe incident angle is  $\theta_p$ .

With the knowledge of the Coulomb field structure, we deduced a new temporal mapping relationship for the application of this method in LWFA. As illustrated in Fig. 4, the probe laser encounters a first line in the THz field at position A and time  $t_A$  and a second line in the THz field at position B and time  $t_B$ . The two lines in the signal have a timing difference of  $\Delta\tau$  and the recorded displacement on the CCD is  $\Delta\xi = \xi_B - \xi_A$ . For a signal with a spherical wavefront, a new temporal mapping relationship is expressed in a nonlinear form as [7]:

$$c\Delta\tau = \Delta\xi \tan \theta_p + \frac{L}{\cos \theta_{s0}} - \frac{L}{\cos \theta_{s0}} \sqrt{1 - \frac{2 \sin \theta_{s0} \cos \theta_{s0}}{\cos \theta_p} \frac{\Delta\xi}{L} + \frac{\cos^2 \theta_{s0}}{\cos^2 \theta_p} \frac{\Delta\xi^2}{L^2}} \quad (1)$$

Because the problem we investigate has a very small time scale, that is,  $\Delta\xi \ll L$ , Eq (1) can be simplified as  $c\Delta\tau = \left(1 + \frac{\sin \theta_{s0}}{\cos \theta_p}\right) \tan \theta_p \Delta\xi - \frac{\cos \theta_{s0}}{\cos^2 \theta_p} \frac{\Delta\xi^2}{2L}$ . Ignoring the higher-order component, we have:

$$c\Delta\tau = \left(1 + \frac{\sin \theta_{s0}}{\sin \theta_p}\right) \tan \theta_p \Delta\xi \quad (2)$$

Eq (2) describes the case in which the THz signal is a plane

wave and obliquely incident on the crystal at an angle of  $\theta_{s0}$ . We note that when setting  $\theta_{s0} = 0$ , Eq (2) returns to the widely used model:  $c\Delta\tau = \Delta\xi \tan \theta_p$ . In the experimental setup, the EO detection point corresponds to an angle of  $\theta_{s0} = 34.3^\circ$ . Using the fitted slope value in Fig. 2 and Eq (2), the average signal incident angle is calculated to be  $\overline{\theta_s} = 33.1^\circ$ . This coincidence demonstrates that the Coulomb fields of the electron bunches near the source point have spherical wavefronts and Eq (2) is applicable for this method in LWFA.

In summary, we introduced, for the first time, the EO spatial decoding technique into LWFA. The temporal signals of the electron bunches have been nondestructively detected in single-shot mode. By setting the EO crystal very close to the plasma exit, we discovered that the Coulomb fields of the electron bunches have spherical wavefronts. A new temporal mapping relationship has been deduced to determine the real timing difference during the decoding process. We believe this study is of significance for the application of EO spatial decoding as a real-time electron bunch timing monitor in LWFA.

## Acknowledgments

We acknowledge Prof. A. Zigler, Prof. P. Bolton, and Dr. A. Pirozhkov for fruitful discussions, and Prof. Hosokai and Dr. Sano for their encouragement. We thank H. Kotaki, M. Mori, Y. Hayashi, and N. Nakanii for help with the experiment. We are grateful for the theoretical support from T. Esirkepov, J. K. Koga, and S. V. Bulanov. This work was funded by the ImPACT Program of the Council for Science, Technology and Innovation (Cabinet Office, Government of Japan).

## References

1. T. Tajima and J. M. Dawson, *Phys. Rev. Lett.* 43, 267 (1979).
2. D. Strickland and G. Mourou, *Opt. Commun.* 55, 447 (1985).
3. M. Fuchs et al., *Nat. Phys.* 5, 826 (2009).
4. A. Rousse et al., *Phys. Rev. Lett.* 93, 135003 (2004).
5. J. van Tilborg et al., *Phys. Rev. Lett.* 96, 014801 (2006); O. Lundh et al., *Nat. Phys.* 7, 219 (2011); A. D. Debus et al., *Phys. Rev. Lett.* 104, 084802 (2010).
6. B. Stefan. No. DESY-THESIS-2007-020. DESY, (2007).
7. K. Huang et al., *Sci. Rep.* 8, 2938 (2018).

# UV harmonics and proton generation from a thin-foil target with the J-KAREN laser

Akito Sagisaka, Alexander S. Pirozhkov, and Hiromitsu Kiriya

Advanced Laser Group, Department of Advanced Photon Research

High-intensity laser and plasma interactions produce particle beams and electromagnetic waves such as high-energy electrons, high-energy ions, and high-order harmonics [1–5]. High-order harmonics have been observed in the relativistic regime with gas [6–8] and solid targets [9–12]. In a gas target, burst intensification by singularity emitting radiation (BISER) is observed [6–8]. In the case of a solid density target, the models of harmonic generation in the relativistic regime include the relativistic oscillating mirror model [3,13,14] and the sliding mirror model [15,16]. In these models, the laser pulse reflected from an oscillating or sliding overdense layer of plasma electrons is modulated and its spectrum contains high-order harmonics. High-energy protons have been observed at the rear side of the thin-foil target [4,5]. In this experiment, UV harmonics in the relativistic regime with protons using an aluminum (Al) foil target irradiated with the J-KAREN laser are observed.

The J-KAREN laser system [17,18] is used as a high-intensity laser. The pulse duration of the laser in this experiment is  $\sim 35$  fs (FWHM). A schematic of the experimental setup is shown in Figure 1. A p-polarized laser pulse is focused with an off-axis parabolic mirror onto a target at an angle of incidence of  $45^\circ$ . The estimated peak intensity is up to  $\sim 10^{21}$  W/cm<sup>2</sup> with the effective pulse duration and effective spot size [19]. The protons are measured with a stack of RCF and CR-39 detectors [20–22]. The reflected UV harmonics are measured with a fiber spectrometer [22,23]. The harmonic radiation is scattered from a PTFE sheet [24,25] and passes through a fiber. A UV harmonic spectrum obtained with a 2- $\mu$ m-thick Al target is shown in Figure 2 [22]. The sharp peaks

are from hard X-rays generated by the laser–plasma interaction. The third- and fourth-order harmonic peaks are broadened and shifted on some shots. The red shift and broadening of the harmonic spectrum can be caused by the Doppler shift at the critical density [26–29] and the relativistic self-phase modulation of the laser as it passes through the preformed plasma [30,31]. The preformed plasma generation at the target front side is considered from the spectral shift and broadening.

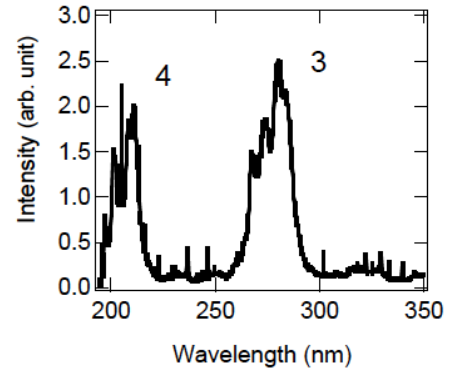


Fig. 2 UV harmonic spectrum with an Al foil target. Reprinted with permission from [22].

The observation of UV harmonics in the relativistic regime is useful for the diagnostics of the laser and thin-foil interaction.

High-energy protons are observed with a thinner target. The maximum proton energy is  $\sim 39$  MeV for a 0.8- $\mu$ m-thick Al target. The third- and fourth-order harmonics are measured for this shot. The integrated third-order harmonic signal as a function of the deflection angle of the proton beam with energies of from around 34 MeV to around 36 MeV obtained from separate laser shots with various fluctuations is shown in Figure 3 [22]. Vertical bars are error bars. Horizontal bars are widths of the proton beam pattern. The deflection angle is taken to be the angle between the proton beam toward the laser beam direction and the target normal direction. The third-order harmonic signal decreases with the deflection angle of the proton beam rather than the proton energy, suggesting that the target rear side deformation from the laser prepulse is likely the relevant reason. This assumes that the UV harmonic intensity decreases as the target front side preformed plasma and target rear side deformation increase, considering that the change in the preformed plasma is related to the fluctuation of the prepulse condition.

Simultaneous generation of UV harmonics and high-energy protons from a thin-foil target are observed in the relativistic regime with the J-KAREN laser.

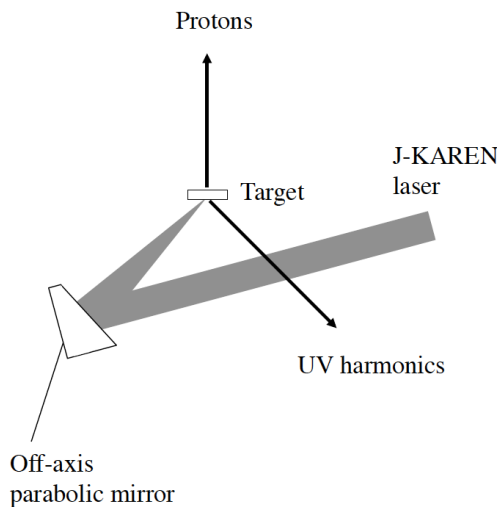


Fig. 1 Schematic view of the experimental setup.

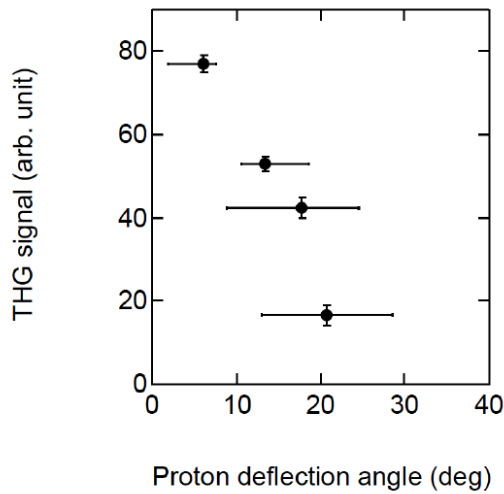


Fig. 3 Integrated third-order harmonic signal as a function of the deflection angle of the proton beam. THG stands for third-order harmonic generation. Reprinted with permission from [22].

## Acknowledgments

We thank K. Ogura, M. Nishiuchi, H. Sakaki, T. Zh Esirkepov, M. Kando, A. Ya. Faenov, T. A. Pikuz, S. V. Bulanov, and K. Kondo for their contributions.

## References

1. G. A. Mourou et al., Rev. Mod. Phys. **78**, 309 (2006).
2. U. Teubner and P. Gibbon, Rev. Mod. Phys. **81**, 445 (2009).
3. S. V. Bulanov et al., Phys. Usp. **56**, 429 (2013).
4. H. Daido et al., Rep. Prog. Phys. **75**, 056401 (2012).
5. A. Macchi et al., Rev. Mod. Phys. **85**, 751 (2013).
6. A. S. Pirozhkov et al., Phys. Rev. Lett. **108**, 135004 (2012).
7. A. S. Pirozhkov et al., New J. Phys. **16**, 093003 (2014).
8. A. S. Pirozhkov et al., Scientific Reports **7**, 17968 (2017).
9. B. Dromey et al., Nature Phys. **2**, 456 (2006).
10. B. Dromey et al., Phys. Rev. Lett. **99**, 085001 (2007).
11. C. Thaury et al., Nature Phys. **3**, 424 (2007).
12. A. Tarasevitch et al., Phys. Rev. Lett. **98**, 103902 (2007).
13. S. V. Bulanov et al., Phys. Plasmas **1**, 745 (1994).
14. R. Lichters et al., Phys. Plasmas **3**, 3425 (1996).
15. A. S. Pirozhkov et al., Phys. Plasmas **13**, 013107 (2006).
16. A. S. Pirozhkov et al., Phys. Lett. A **349**, 256 (2006).
17. H. Kiriya et al., Opt. Lett. **35**, 1497 (2010).
18. H. Kiriya et al., IEEE Sel. Topics J. Quantum Electron. **21**, 1601118 (2015).
19. A. S. Pirozhkov et al., Opt. Express **25**, 20486 (2017).
20. K. Ogura et al., Opt. Lett. **37**, 2868 (2012).
21. M. Nishiuchi et al., Phys. Plasmas **22**, 033107 (2015).
22. A. Sagisaka et al., The Review of Laser Engineering, **46**, 148 (2018).
23. I. W. Choi et al., Appl. Phys. Lett. **99**, 181501 (2011).
24. A. S. Pirozhkov et al., Appl. Phys. Lett. **94**, 241102 (2009).
25. A. S. Pirozhkov et al., in *2nd Int. Symp. Laser-Driven Relativistic Plasmas Applied to Science, Industry and Medicine*, AIP Conf. Proc. **1153**, 7 (2009).
26. M. Zepf et al., Phys. Plasmas **3**, 3242 (1996).
27. M. P. Kalashnikov et al., Phys. Rev. Lett. **73**, 260 (1994).
28. S. C. Wilks et al., Phys. Rev. Lett. **69**, 1383 (1992).
29. W. L. Kruer et al., Phys. Rev. Lett. **35**, 1076 (1975).
30. C. A. Coverdale et al., Fiz. Plazmy, **22**, 685 (1996) [Plasma Phys. Rep. **22**, 617 (1996)].
31. I. Watts et al., Phys. Rev. E **66**, 036409 (2002).



# High-repetition, multi-MeV, pure proton source via Coulomb explosion of micron-scale hydrogen cluster targets

Yuji Fukuda, Ryutaro Matsui and Hiromitsu Kiriya

Advanced Laser Group, Department of Advanced Photon Research

Laser-driven ion acceleration has been one of the most active areas of research over approximately the past decade, because accelerated multi-MeV ion beams have unique properties that can be employed in a broad range of applications, including nuclear science, hadron cancer therapy, and fast ignition for inertial confinement fusion. Recent advancements in laser-driven ion acceleration techniques using thin-foil targets allow maximum proton energies close to 100 MeV. From the perspective of practical applications, high-purity proton beams with high reproducibility are quite advantageous. In experiments using thin-foil targets, however, protons from surface contaminants along with high- $z$  component materials are accelerated together, making the production of impurity-free proton beams unrealistic.

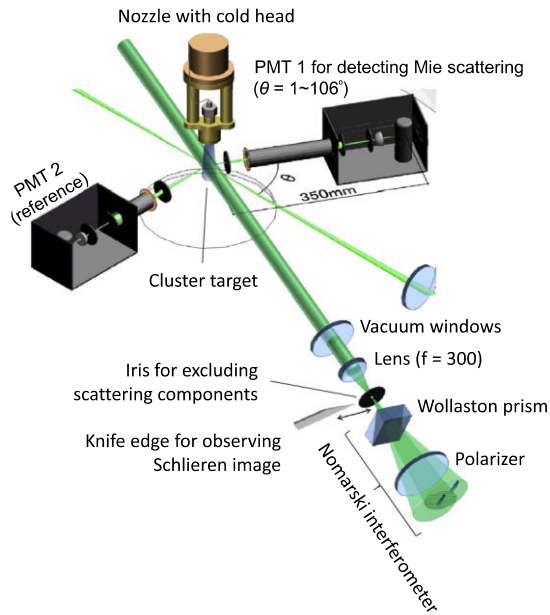


Fig. 1 Schematic of experimental setup for the cluster size measurement using Mie scattering and for the gas phase density measurement using a Nomarski interferometer.

Here, we introduce a micron-scale hydrogen cluster, composed of  $10^8 \sim 10^{10}$  hydrogen molecules, as a target to generate impurity-free, highly reproducible, and robust multi-MeV proton beams [1,2]. Because of the recent progress in intense laser technology, advanced PW-class lasers can now achieve intense laser fields of approximately  $10^{22}$  W/cm<sup>2</sup>. With such fields, all the electrons inside a micron-scale hydrogen cluster up to 3.0  $\mu$ m in diameter can be fully stripped off, resulting in a pure Coulomb explosion with a pronounced increase in the maximum accelerated proton energies, scaled as  $E_{max} = 276(d/2)^2$  MeV, where  $d$  is the cluster diameter. For example, 100-MeV protons

could be produced via the Coulomb explosion of a 1.2- $\mu$ m-diameter hydrogen cluster under irradiation by a laser pulse with a peak intensity of  $1.6 \times 10^{21}$  W/cm<sup>2</sup> [2]. The robust nature of the Coulomb explosion mechanism offers an additional advantage for practical applications.

Hydrogen clusters with diameters in the few-micrometer range have been produced for the first time in an expansion of supercooled, high-pressure hydrogen gas into a vacuum through a conical nozzle connected to a cryogenic pulsed solenoid valve [1,2]. The size distribution of the clusters has been evaluated by measuring the angular distribution of laser light scattered from them (see Fig. 1). The data were analyzed based on the Mie scattering theory combined with the Tikhonov regularization method, including instrumental functions, the validity of which was assessed by performing a calibration study using a reference target consisting of standard microparticles with two different sizes. The size distribution of the clusters was found to show discrete peaks at  $0.33 \pm 0.03$ ,  $0.65 \pm 0.05$ ,  $0.81 \pm 0.06$ ,  $1.40 \pm 0.06$ , and  $2.00 \pm 0.13$   $\mu$ m in diameter, as shown in Fig. 2.

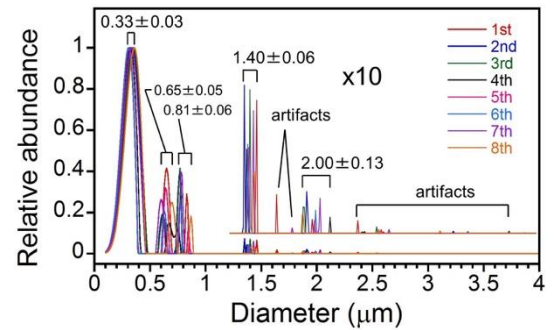


Fig. 2 Size distributions of hydrogen clusters measured using the Mie scattering method at the pulsed valve temperature of 25 K and the hydrogen gas pressure of 6 MPa.

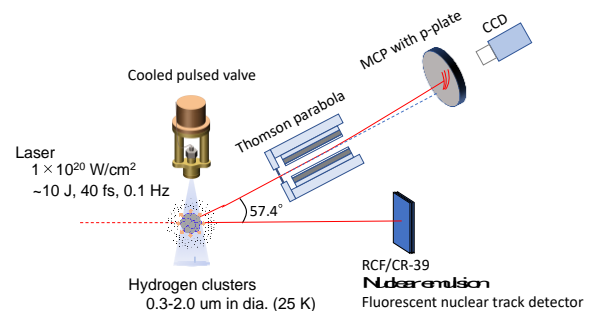


Fig. 3 Schematic of experimental setup for laser-driven proton acceleration using the micron-scale hydrogen clusters.

By using the micron-scale hydrogen cluster target, we have conducted ion acceleration experiments at a focused laser intensity of  $1 \times 10^{20}$  W/cm<sup>2</sup> [3] with the 0.1-Hz PW-class J-KAREN laser at QST-KPSI [4] (see Fig. 3). In order to characterize the accelerated ions, we used the nuclear track detector plates (CR-39), nuclear emulsion plates [5], and real-time Thomson parabola equipped with a microchannel plate (MCP), phosphor screen, and CCD camera. We have succeeded in acquiring a proton-only signal at 0.1 Hz using the real-time Thomson Parabola, which was installed at an angle of 57.4 degrees with respect to the beam axis (see Fig. 4). We also found from the CR-39 that protons with a maximum energy of 12 MeV, consistent with the numerical simulations [6], were accelerated in the laser propagation direction.

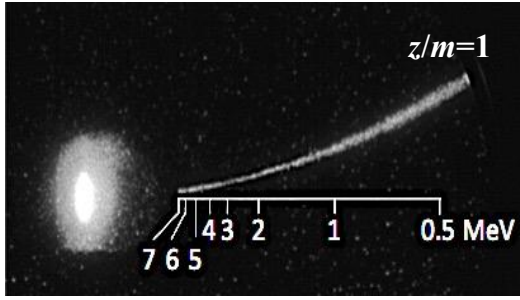


Fig. 4 Single-shot proton signals detected using the Thomson parabola spectrometer equipped with an MCP, a phosphor screen, and a CCD camera. The maximum energy was estimated to be approximately 7 MeV. The bright spot is due to neutral particles and UV lights generated from the irradiated target.

Looking to the future, the possibility of producing directional quasimonoenergetic proton bunches at the energy level of 300 MeV, in combination with advanced PW-class lasers [7], is quite promising for practical applications, because such beams are inherently highly reproducible and free of impurities and debris.

## Acknowledgments

The author thanks Drs. M. Kanasaki, S. Jinno, A. Sagisaka, K. Ogura, N. Nakanii, Y. Miyasaka, H. Sakaki, H. Tanaka, M. Uno, Y. Takano, K. Morii, T. Asai, K. Sakamoto, K. Shimizu, Y. Okamoto, K. Morishima, S. Kodaira, Y. Kishimoto, K. Oda, T. Yamauchi, M. Uesaka, A. Sugiyama, K. Kondo, T. Kawachi, and M. Kando for their technical assistance, fruitful discussions, and encouragement.

## References

1. S. Jinno, H. Tanaka, R. Matsui, M. Kanasaki, H. Sakaki, M. Kando, K. Kondo, A. Sugiyama, M. Uesaka, Y. Kishimoto, Y. Fukuda, Characterization of micron-size hydrogen clusters using Mie scattering, *Opt. Express* **25**, 18774 (2017).
2. S. Jinno, M. Kanasaki, M. Uno, R. Matsui, M. Uesaka, Y. Kishimoto, Y. Fukuda, Micron-size Hydrogen Cluster Target for Laser-Driven Proton Acceleration, *Plasma Phys. Control. Fusion* **60**, 044021 (2018).
3. A. S. Pirozhkov, Y. Fukuda, M. Nishiuchi, H. Kiriyama, A. Sagisaka, K. Ogura, M. Mori, M. Kishimoto, H. Sakaki, N. P. Dover, K. Kondo, N. Nakanii, K. Huang, M. Kanasaki, K. Konko, M. Kando, Approaching the diffraction-limited, bandwidth-limited Petawatt, *Opt. Express* **25**, 20486 (2017).
4. H. Kiriyama, A. S. Pirozhkov, M. Nishiuchi, Y. Fukuda, K. Ogura, A. Sagisaka, Y. Miyasaka, M. Mori, H. Sakaki, N. P.

- Dover, K. Kondo, J. K. Koga, T. Zh. Esirkepov, M. Kando, K. Kondo, High-contrast high-intensity repetitive petawatt laser, *Opt. Lett.* **43**, 2595 (2018).
5. T. Asai, M. Kanasaki, S. Jinno, N. Shutoh, T. Yamauchi, K. Oda, K. Morishima, Y. Fukuda, Application of nuclear emulsions for the identification of multi-MeV protons in laser ion acceleration experiments, submitted to *High Energy Density Physics* (2018).
6. Y. Okamoto, R. Matsui, Y. Fukuda, Y. Kishimoto, Cluster size dependence in Coulomb explosion of hydrogen clusters, *The Physical society of Japan 2018 Annual (73rd) Meeting*, March 2018, Chiba, Japan.
7. R. Matsui, Y. Fukuda, Y. Kishimoto, Quasimonoenergetic Proton Bunch Acceleration Driven by Hemispherically Converging Collisionless Shock in a Hydrogen Cluster Coupled with Relativistically Induced Transparency, *Phys. Rev. Lett.* **122**, 014804 (2019).

# Analytical formulation for electron excitation in dielectrics under an intense laser field

Tomohito Otake

Ultrafast Dynamics Group, Department of Advance Photon Research

Electron excitation in dielectrics by an intense laser field is the main process in laser–matter interactions. Technical developments in femtosecond laser processing have made it possible to produce a nanoscale laser-induced periodic surface structure (LIPSS), and to realize nonthermal ablation for subwavelength resolution [1–4]. For femtosecond lasers, electron excitation by multiphoton ionization and tunnel ionization is crucial, because such nonlinear processes generate a controllable free-carrier density and confine the material change to the focal volume. Therefore, the prediction of the electron excitation rate using theoretical models and/or numerical simulation is important.

Keldysh proposed a theory for the rate of electron excitation under an intense linearly polarized laser field [5]. His approach is very general and can be used to describe the photoionization of different objects from single atoms to crystals. Because of its generality, the Keldysh model has attracted much attention and has become one of the standard tools in the theory of laser photoionization. For atoms and molecules, the Keldysh–Faisal–Reiss (KFR) theory, which is an implementation of the original Keldysh work, is one of the most important theories in understanding the electron–laser interaction.

Jones and Reiss have developed a formula for the rate of electron excitation under a circular polarized laser employing the  $S$ -matrix theory [6]. Whereas the Keldysh formula treats the time-dependent wavefunction of the valence and conduction bands as the Houston function and includes only the reduced electron–hole mass, the Jones and Reiss formula treats only the conduction band as the Houston function (Volkov state) and includes the effective mass of the valence and conduction bands independently. Therefore, a direct comparison between the Keldysh and Jones formulas is not relevant.

The purpose of this work is to construct an analytical formula for the transition probability in dielectrics including multiphoton and tunneling processes under a circularly polarized laser. We derive the transition probability in a crystalline solid under a circularly polarized laser, assuming a parabolic two-band system and using the Houston function [7] as the time-dependent wave function.

The total transition probability induced by the circularly polarized laser is found to be

$$W_c = \frac{e^2 A_0^2 P^2 \mu^{3/2}}{\sqrt{2} \pi m^2 c^2} \sum_{l=l_0}^{\infty} \int d\theta \sin \theta \left( J_{l-1}^2(\eta') + J_{l+1}^2(\eta') \right) \sqrt{\zeta_l}, \quad (1)$$

where

$$\eta' = \frac{e A_0 \sqrt{2 \zeta_l} \sin \theta}{\sqrt{\mu} \omega c}, \quad (2)$$

and

$$\zeta_l = l\omega - (B_g + U_p). \quad (3)$$

Here,  $J_l(\eta)$  is the Bessel function.

The total transition probability induced by the linearly polarized laser is found to be

$$W_L = \frac{e^2 A_0^2 P^2 \mu^{3/2}}{2 \sqrt{2} \pi m^2 c^2} \sum_{l=l_0}^{\infty} \int d\theta' \sin \theta' \left( J_{l-1}(\alpha, \beta) + J_{l+1}(\alpha, \beta) \right)^2 \sqrt{\kappa_l}, \quad (4)$$

where

$$\kappa_l = l\omega - (B_g + U_p). \quad (5)$$

Here,  $\theta'$  is the angle between the polarization direction and  $\vec{k}$ , and  $l_0$  is the maximum integer  $l$  at which  $\kappa_l > 0$ .  $J_l(\alpha, \beta)$  is the generalized Bessel function and  $U_p = e^2 A_0^2 / 4\mu c$  is the ponderomotive energy.  $\alpha$  and  $\beta$  are defined as

$$\alpha = \frac{e A_0 \sqrt{\kappa_l} \cos \theta'}{\sqrt{\mu} \omega c}, \quad \beta = \frac{e^2 A_0^2}{8 \mu \omega c^2}. \quad (6)$$

$\alpha$ -quartz is a typical dielectric used in nonlinear laser–matter interaction studies, and we selected it here as an example with which to illustrate the application of our developed formalism. The transition probability ( $W_L$ ) of  $\alpha$ -quartz by linearly polarized 800-nm light is shown in Fig. 1 by a red solid line.

We assumed a band gap of 9 eV and reduced mass of 0.30  $m$  [8].  $W_L$  calculated by the full expression of the conventional Keldysh formula (dashed line) and tunneling limit (dot-dashed line) are also shown in Fig. 1 for comparison. Our formalism shows excellent agreement with the Keldysh theory. This result indicates that our formula includes the multiphoton and tunneling processes as the Keldysh formula does.

The transition rate induced by circularly polarized 800-nm light as a function of laser intensity is illustrated in Fig. 2 as a blue dashed line. The transition rate induced by linearly polarized 800-nm light is also shown as a solid red line. The power law of the transition rate induced by the circularly polarized light is slightly different from that for linearly polarized light, and higher than that for linearly polarized light of higher intensity. Temnov *et al.* [9] reported the ratio of the ionization rate around an intensity of  $1 \times 10^{13}$  W/cm<sup>2</sup>. From the relationship between the

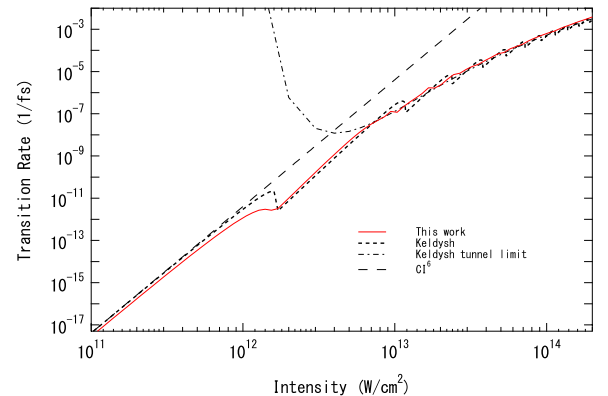


Fig. 1 Transition probability as a function of laser intensity for linearly polarized 800-nm light in  $\alpha$ -SiO<sub>2</sub>. The red solid line represents the excitation rate determined by our formalism, the blue dashed line represents the excitation rate based on the full expression of the Keldysh theory, the green dotted line represents the tunneling limit of the Keldysh theory, and the black dot-dashed line represents the simple six-photon process.



intensity in vacuum ( $I_v$ ) and that in media ( $I_m$ ),  $I_m = \varepsilon^{1/2} I_v$ , where  $\varepsilon$  is the dielectric constant,  $1 \times 10^{13}$  W/cm<sup>2</sup> corresponds to  $4 \times 10^{12}$  W/cm<sup>2</sup> in Fig. 2. The experimental value for the excitation rate ratio  $W_c/W_L$  is 0.3. Our result gives ratios of 0.1–0.2 at  $(2 \times 10^{12})$ – $(1 \times 10^{13})$  W/cm<sup>2</sup>, which is in reasonable agreement with the experimental value. We extended the Keldysh-type formula for the solid state under an intense circularly polarized laser, assuming the Houston function for the valence and conduction bands. Because our formula depends only on the reduced mass, it can be directly compared with the Keldysh formula. Our simple formula describes the electron excitation rate, reproduces the Keldysh formula with excellent agreement for  $\alpha$ -quartz, and makes it possible to separate the contribution of each  $l$ -photon process with linear or circular polarization. The ratio of the rate of transition under linear polarization to that under circular polarization determined using our formula shows reasonable agreement with the experimental results.

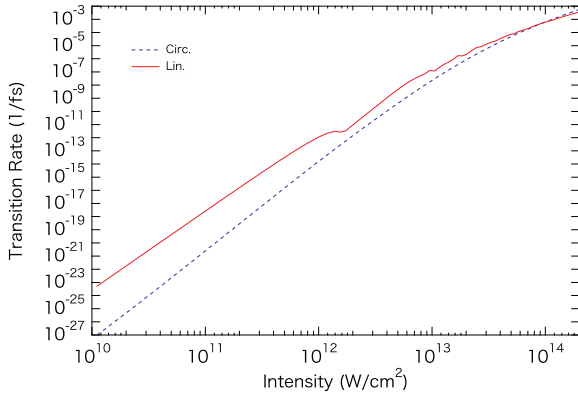


Fig. 2 Transition probability as a function of electric field intensity for linearly polarized (red solid line) and circularly polarized (blue dashed line) light.

### Acknowledgments

The author thanks Y. Shinohara, S. A. Sato, and K. Yabana. This work was supported by JST-CREST under grant number JP-MJCR16N5 and by JSPS KAKENHI (Grants Nos. 21740303, 15H03674, and 17K05089). Numerical calculations were performed on the supercomputer PRIMERGY BX900 at the Japan Atomic Energy Agency (JAEA).

### References

1. K. M. Davis, K. Miura, N. Sugimoto, and K. Hirao, *Opt. Lett.* **21**, 1729 (1996).
2. R. R. Gattass and E. Mazur, *Nat. Photonics* **2**, 219 (2008).
3. K. Miura, J.R. Qiu, H. Inouye, T. Mitsuyu, and K. Hirao, *Appl. Phys. Lett.* **71**, 3329 (1997).
4. V. R. Bhardwaj, E. Simova, P. P. Rajeev, C. Hnatovsky, R. S. Taylor, D. M. Rayner, and P. B. Corkum, *Phys. Rev. Lett.* **96**, 057404 (2006).
5. L. V. Keldysh, *Sov. Phys. JETP* **20**, 1307 (1965).
6. H. D. Jones and H. R. Reiss, *Phys. Rev. B* **16**, 2466 (1977).
7. W. V. Houston, *Phys. Rev.* **57**, 184 (1940).
8. B. Brar, G. D. Wilk, and A. C. Seabaugh, *Appl. Phys. Lett.* **69**, 2728 (1996).
9. V.V. Temnov, K. Sokolowski-Tinten, P. Zhou, A. El-Khamhawy, and D. von der Linde, *Phys. Rev. Lett.* **97**, 237403 (2006).
10. Khamhawy, and D. von der Linde, *Phys. Rev. Lett.* **97**, 237403 (2006).

# Spatiotemporal characterization of VUV pulses by plasma-mirror frequency-resolve optical gating

Ryuji Itakura, Hiroshi Akagi, and Tomohito Otobe

Ultrafast Dynamics Group, Department of Advanced Photon Research

High-order harmonics of femtosecond laser pulses are known to be a powerful tool for time-resolved photoelectron spectroscopy and transient absorption spectroscopy of atoms and molecules. Short-wavelength pulses generated as high-order harmonics are also sensitive probes into laser plasma with a high density of excited electrons on the surface of solid materials, because the plasma resonance frequency is proportional to the square root of the density of excited electrons. Recently, we demonstrated that time-resolved vacuum ultraviolet (VUV) reflection spectroscopy is applicable to the characterization of VUV pulses and to the extraction of reflectivity changes in ultrafast plasma formation [1, 2]. In this study, we carefully investigate not only the temporal characteristic, but also the spatial mode of plasma reflection.

The output pulses of a Ti:Sapphire laser (80 fs, 795 nm, 10 Hz) are focused on a Xe gas jet for high-order harmonic generation. The fundamental ( $\omega$ ) and fifth harmonics ( $5\omega$ ) are separated with a multilayer mirror for 160-nm reflection. After adding a delay between  $\omega$  and  $5\omega$ , two beams are colinearly recombined and focused on a transparent solid target of fused silica (FS). The target is continuously moved with a two-dimensional motorized stage such that the fresh surface is irradiated with laser pulses. Time-resolved VUV reflection spectra of FS are measured with a Seya-Namioka-type VUV spectrometer equipped with an imaging detector at the exit.

In the analysis, we improve the FROG iteration procedure based on the least-squares generalized projections algorithm [2]. As a result, the Fresnel reflection of the unexcited FS surface is included in the time-dependent reflectivity. The retrieved reflectivity is normalized by setting the reflectivity of the unexcited FS to unity. The spectrum component only by the  $\omega$  irradiation is subtracted from the spectrum measured by the irradiation of both  $\omega$  and  $5\omega$ .

The two-dimensional (2D) image at the exit of the spectrometer is recorded by a CCD camera in shot-by-shot mode. A raw single-shot image on the phosphor screen is shown in Fig. 1, where the horizontal axis is transformed to the wavelength and

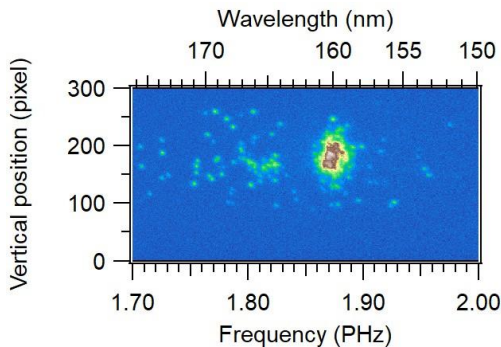


Fig. 1 Raw image of reflected VUV beam at the exit of VUV spectrometer.

the vertical axis represents the spatial coordinate of the VUV beam in the vertical direction on the screen.

From the central part ( $175 \leq y \leq 190$  pixels) in the vertical distribution, time-resolved VUV reflection spectra are obtained as shown in Fig. 2(a). In the negative-delay region, the weak Fresnel reflection of the unexcited FS surface is observed. Around zero delay ( $\tau = 0$ ), the plasma is formed by the pump  $\omega$  pulse and then the reflectivity rapidly increases.

Through the FROG analysis based on the LSGPA, we can successfully retrieve the time-resolved reflection spectra as shown in Fig. 2(b). The  $5\omega$  pulse shape and temporal reflectivity are simultaneously characterized as shown in Fig. 3(a) and 3(b), respectively. The pulse duration of the  $5\omega$  pulse is extracted as 20 fs, which is nearly the Fourier-transform limit. The reflectivity of FS increases to the maximum  $R_{\max}$  from the Fresnel reflectivity  $R_0$  within the  $\omega$  pulse duration of 80 fs. Thus, it is demonstrated that the 20-fs duration of the  $5\omega$  pulse can be characterized by PM-FROG, even if the rise time of the plasma reflectivity is longer than the  $5\omega$  pulse duration.

Next, we examine the spatial dependence of the  $5\omega$

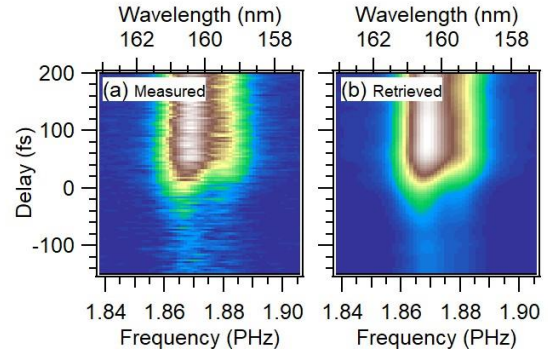


Fig. 2 Time-resolved reflection spectra of plasma mirror on FS. (a) Measured and (b) retrieved results.

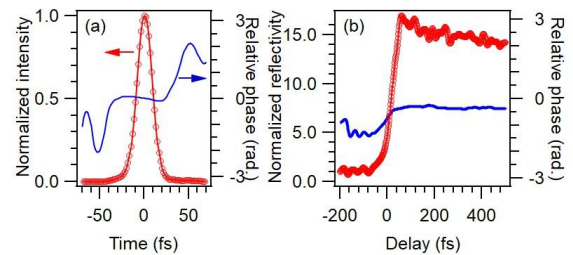


Fig. 3 (a) Retrieved  $5\omega$  pulse-shape. (Red circles: intensity, blue line: relative phase). (b) Time-dependent reflectivity (red circles) and its phase (blue line) of the plasma mirror. Reflectivity is normalized with the Fresnel reflectivity  $R_0$  of the unexcited FS surface.

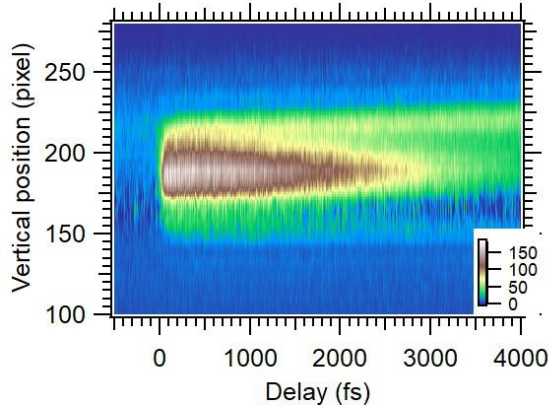


Fig. 4 Time-resolved spatial (vertical) profile of the reflected  $5\omega$  beam. The signal caused solely by pump-laser irradiation is subtracted.

waveform. The vertical spatial profile of the  $5\omega$  beam is obtained by integrating over the wavelength range between 159.1 and 161.2 nm. The temporal variation of the spatial profile is shown in Fig. 4. It is clear that there are two types of temporal behavior in the reflectivity. After the rapid increase, the reflectivity decreases almost to the initial value  $R_0$  at the delay of  $\tau = 4$  ps in the spatial region below  $y = 210$  pixels. In the region above  $y = 210$  pixels, a singularly slow decay of the reflectivity can be observed. It is known that a Seya–Namioka-type VUV spectrometer has inherent astigmatism. In other words, a high spectral resolution is achieved at the sacrifice of the vertical focusing. Nevertheless, a strong spatial dependence of the time-resolved reflectivity appears in the present measurement. It is worth discussing the spatial property of the plasma reflectivity qualitatively.

The maximum reflectivity  $R_{\max}$  depends on the spatial region. This is attributed to the excited electron density governed by the spatial intensity profile of the pump  $\omega$  beam, which should have the highest intensity in the spatially central part. As a result, the spatial distribution of the excited electron density exhibits the peak in the central region of the beam. The dependence of the reflectivity on the distance from the center reflects the spatial distribution of the excited electron density, as previously reported by Siegel et al. [3]. Although the reflectivity strongly depends on the spatial region, the VUV waveform is almost independent of the spatial region. In other words, the waveform of the VUV pulse is measured to be spatially uniform.

In addition to the major component, the singularly long decay component is also identified in the upper edge region of 210–230 pixels of the time-resolved spatial profile. This long decay is attributed to the reflection at the outermost ring of the ablation crater, where the fused silica surface survives after the ablation [3]. Although photoexcitation takes place at the outermost ring, the removal of the atomic layer hardly occurs. A certain amount of the atomic density is maintained at the outermost ring after the laser pulse irradiation, whereas the spallation takes place in the spatially central region. The decay rate in the upper edge region is expected to be governed dominantly by the electronic relaxation in the absence of ablation.

Further, it is found that the long decay component shifts spatially upward in the vertical direction as the delay increases. This shift reflects the dynamics occurring at the outermost ring. Material densification was proposed as a possible mechanism [3]. The spatial shift measured in this study is an indication of the radial expansion of the densification ring.

In summary, we demonstrated that a nearly Fourier-transform-limited VUV pulse with a pulse duration of 20 fs can

be characterized by PM-FROG. In addition, the temporal waveform of the VUV pulse is measured to be spatially uniform, whereas the reflectivity depends on the spatial profile of the plasma mirror. The spatial characterization of the VUV pulse becomes more important because of the rapid progress of ultrafast microscopy and coherent diffractive imaging in the short-wavelength region. Simultaneously, the spatiotemporal dependence of the reflectivity is also obtained by PM-FROG. The measurement technique of PM-FROG will be able to make a substantial contribution to ultrafast imaging in the VUV region.

## Acknowledgments

The authors thank Y. Hagihara and Y. Wada for their support, and N. Hasegawa, M. Nishikino, T. Imazono, M. Ishino, and T. Nakajima for their valuable discussions. This study has been supported by the following funding sources: MEXT Q-LEAP program; C-PhoST program; JSPS KAKENHI (17H02802); Research Foundation for Opto-Science and Technology; Institute of Advanced Energy, Kyoto University, the Joint Usage/Research Program on Zero-Emission Energy Research (ZE30B-37).

## References

1. R. Itakura, T. Kumada, M. Nakano, and H. Akagi, *Opt. Express* **23**, 10914 (2015).
2. R. Itakura, T. Kumada, M. Nakano, and H. Akagi, *High Power Laser Sci. Eng.* **4**, e18 (2016).
3. J. Siegel, D. Puerto, W. Gawelda, G. Bachelier, J. Solis, L. Ehrentraut, and J. Bonse, *Appl. Phys. Lett.* **91**, 082902 (2007).

# Development of a tender X-ray emission spectrometer with an aperiodic Ni/C multilayer grating

Takashi Imazono

X-ray Laser Group, Department of Advanced Photon Research

X-ray emission spectroscopy (XES) is a powerful tool for studying the electronic structure of materials. Recently, with the advent of high-brilliance synchrotron radiation sources, XES studies in the photon energy range between approximately 1 and 5 keV, the so-called tender X-ray range, have gained increased attention. In our previous study, a flat-field spectrometer equipped with an aperiodic W/B<sub>4</sub>C multilayer-coated varied-line-spacing (VLS) grating for use in combination with electron microscopes was developed, and high-resolution X-ray emission spectra in the tender X-ray range were successfully measured at a constant angle of incidence, i.e., with no mechanical movement, which is a necessary condition to be installed in a transmission electron microscope (TEM) [1,2]. The aperiodicity of the multilayer structure on the VLS grating originates from the topmost bilayer with a larger thickness than the other W/B<sub>4</sub>C bilayers. This plays a role in enhancing the reflectance of the longer wavelengths based on a similar principle to hard X-ray supermirrors; it contributes a uniform diffraction efficiency over the range 2–4 keV. In spite of the fact that XES measurements in the range 1–2 keV, in which various X-ray emission lines are observed, are also regarded as important in materials science research, it is difficult to effectively detect and resolve X-ray emissions in the range with this spectrometer, because of the  $M_{4,5}$  absorption edges of tungsten in addition to the spectral resolution reduction. We have invented aperiodic Ni/C multilayers capable in covering the energy range 1–3.5 keV at constant angles of incidence, and developed a flat-field spectrometer equipped with a VLS grating and a pre-focusing mirror coated with these Ni/C multilayers [3]. Such a pre-focusing mirror is useful not only for collecting divergent X-ray radiation in a wide variety of measurements, but also for preventing ablation debris from the source point from reaching the optical components of the system in laser plasma X-ray measurements. We herein report on the spectrometer performance evaluated from the linewidths of the various characteristic X-ray lines from 1 to 3.5 keV.

Figure 1(a) shows a schematic diagram of a flat-field grating spectrometer with a pre-focusing mirror. Light from a light source  $S_0$  passes through a bandpass filter  $F$  and irradiates a toroidal mirror  $M$  of tangential and sagittal radii of curvature 12000 and 28 mm, respectively, at an angle of incidence  $\varphi_M = 88.40^\circ$ . The light transmitted through an entrance slit  $S$  is incident onto a spherical VLS grating  $G$  at an angle of incidence  $\alpha = 88.53^\circ$ , where we have assumed the identical grating parameters to those of the previously described W/B<sub>4</sub>C multilayer grating, except for the coating: an effective grating constant of  $1/2400$  mm, a groove depth of 2.8 nm, a duty ratio of 0.5, and a radius of curvature of 11200 mm [1,3]. Note that this spectrometer, of which the length from  $S$  to  $\Sigma$  is approximately 0.5 m, is quite compact compared to other grating spectrometers being used in synchrotron radiation beamlines. Based on ray tracing results, it is found that the resolving power  $E/\Delta E$  varies from 400 to 1200 over the range 1 to 3.5 keV, and is dominant to the pixel size of the detector used, which means that the aberration from the grating and mirror is small enough.

Figure 1(b) shows a schematic diagram of an aperiodic Ni/C multilayer consisting of two blocks. One is a periodic Ni/C multilayer: the thickness of a Ni/C pair is  $D_1$ , the ratio of the C thickness to  $D_1$  is  $\gamma_1$ , and the number of layers is  $N_1$ . The other is an inverted C/Ni bilayer on the periodic multilayer: the thickness is  $D_2$ , the ratio of the C layer thickness to  $D_2$  is  $\gamma_2$ , and the number of layers is  $N_2 = 2$ . Just like the previous W/B<sub>4</sub>C multilayer, the aperiodicity of this multilayer originates from the topmost bilayer including the continuous  $N_1$ th and  $(N_1 + 1)$ th C layer, which cannot be distinguished. A conventional multilayer mirror with a constant period thickness exhibits high reflectivity, but the bandwidth is too narrow to cover the energy range 1–3.5 keV at a fixed angle of incidence. The reflectivity of the aperiodic Ni/C multilayer can be improved by optimizing the inverted C/Ni bilayer, resulting in  $D_1 = D_2 = 5.6$  nm,  $\gamma_1 = 0.5$ ,  $N_1 = 80$ , and  $\gamma_2 = 0.2$  for the grating; and  $D_1 = D_2 = 7.5$  nm,  $\gamma_1 = 0.5$ ,  $N_1 = 80$ , and  $\gamma_2 = 0.2$  for the toroidal mirror [3]. Multilayer films were deposited by ion beam sputtering on a gold-coated laminar VLS grating manufactured by Shimadzu Corporation and a toroidal substrate made of synthetic quartz. The multilayer periods corresponding to  $D_1$  were evaluated as 5.77 nm for the grating and 8.01 nm for the toroidal mirror.

Figure 1(c) shows a comparison of the measured first-order diffraction efficiencies of the aperiodic Ni/C multilayer grating (AMG) and the gold-coated grating (AuG) as a function of the incident X-ray energy. The large efficiency reduction at approximately 2.2 keV in the AuG completely disappears after the multilayer coating, and the diffraction efficiency has been improved in the wide range from 2.1 to 3.5 keV. It seems that the unmeasured data between 1.2 and 1.7 keV can be interpolated reasonably well; the AMG has a highly uniform diffraction efficiency over the 1–3.5 keV range. Similarly, the aperiodic Ni/C multilayer-coated toroidal mirror achieves sufficiently high reflectivity throughout the range of interest, although there is an unmeasured datapoint and a discrepancy between the calculation and experiment below 2 keV (not shown in this paper).

The performance of the flat-field grating spectrometer in combination with the pre-focusing mirror was evaluated by measuring various characteristic X-rays of materials, such as a Cu(In,Ga)Se<sub>2</sub>-based thin-film solar cell, which is referred to as CIGS and is one of the extensively researched photovoltaic thin-film solar cells [4]. Figure 1(d) shows the X-ray emission spectra from a CIGS solar cell specimen (EnerPlex) excited by electron beam with an 8-kV accelerating voltage:  $La$  and  $L\beta_1$  of Cu, Zn, and Mo;  $La$ ,  $L\beta_1$ ,  $L\beta_{3,4}$ ,  $Ll$ , and  $L\eta$  of Ga and Se; and  $La$  of In. Note that  $La$  denotes the  $La_{1,2}$  doublet. It is considered that Zn and Mo originate from the front and back electrodes of ZnO and Mo, respectively, which sandwich the CIGS absorber layer in the solar cell. The oxygen  $K\alpha$  line was also clearly observed (not shown in the figure). The full-widths at half maxima (FWHMs) of the  $La$  line are as follows: 4.9 eV for Cu; 26.1 eV for In; 4.6 eV for Ga; 6.1 eV for Se; 3.8 eV for Zn; 14.2 eV for Mo. They are summarized in Fig. 1(e). In addition, the FWHMs of the  $K\alpha$ ,

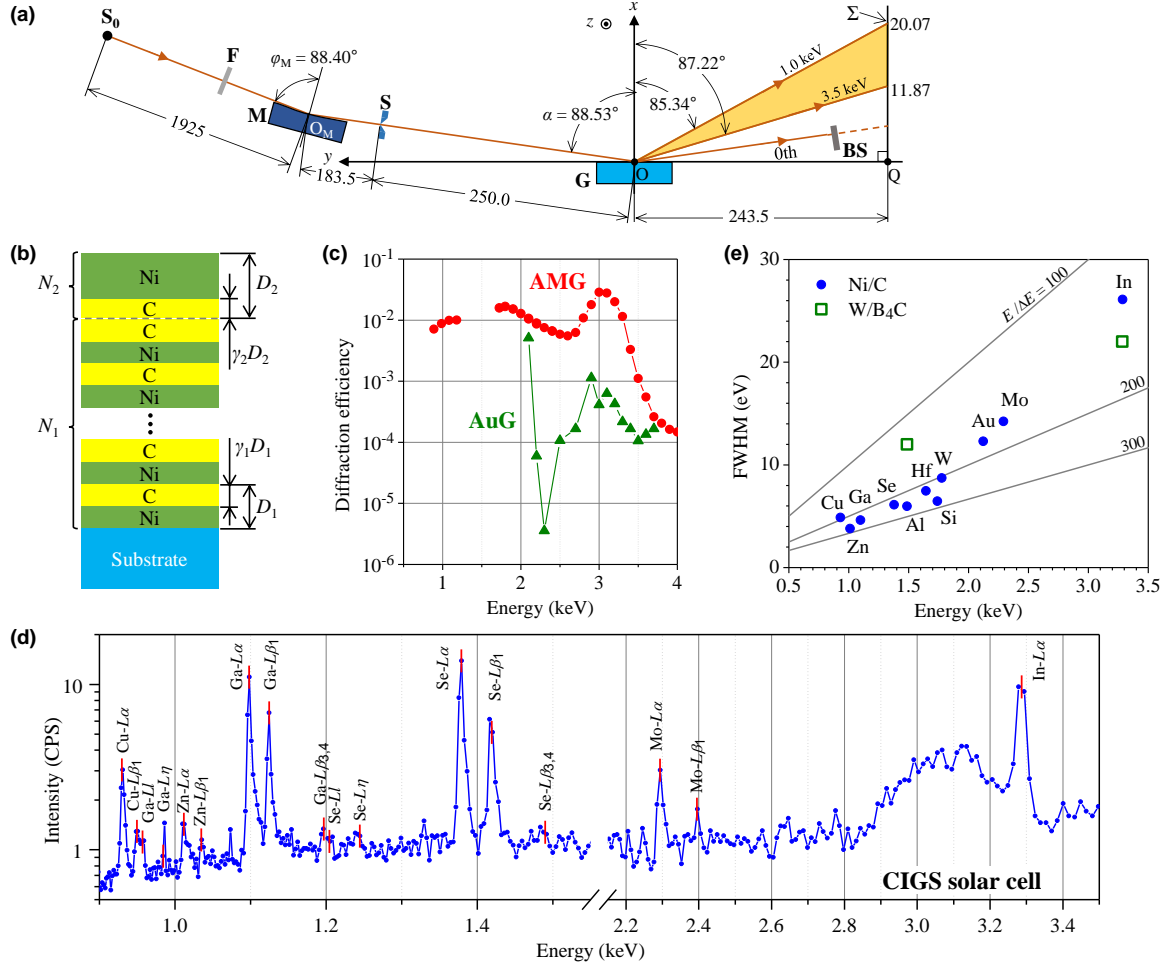


FIG. 1 (from Ref. [3]). (a) Schematic diagram (not to scale) of a flat-field grating spectrometer with a pre-focusing mirror. (b) Schematic diagram of an aperiodic Ni/C multilayer. (c) Comparison of the measured diffraction efficiencies of the aperiodic Ni/C multilayer grating (AMG) and the gold-coated grating (AuG). (d) Measured X-ray emission spectra from a CIGS solar cell specimen. (e) Plot of FWHMs of the  $K\alpha$ ,  $L\alpha$ , and  $M\alpha$  lines versus the centroid energy. The solid lines represent the linewidths corresponding to the energy resolutions  $E/\Delta E$  of 100, 200, and 300. The squares indicate the FWHMs of the Al- $K\alpha$  and In- $L\alpha$  spectra measured with the former spectrometer equipped with an aperiodic W/B<sub>4</sub>C multilayer grating for the 2–4 keV range [2].

$L\alpha$ , and  $M\alpha$  lines of other elements measured in this study are also plotted for comparison. The solid lines represent the bandwidths corresponding to energy resolutions  $E/\Delta E = 100, 200$ , and  $300$ . The spectral resolution is over 200 between 1.0 and 1.8 keV and achieves  $\sim 270$  at the Si- $K\alpha$  and Zn- $L\alpha$  lines. This value is one order of magnitude higher than that of a conventional energy-dispersive X-ray spectrometer (EDS) and twice as high as that measured with the former spectrometer equipped with an aperiodic W/B<sub>4</sub>C multilayer grating for the 2–4 keV range, as indicated by the squares [2]. The FWHM of the In- $L\alpha$  line broadens by 4.1 eV but can be regarded as almost equivalent. Thus, considering the fact that both the Ni/C and W/B<sub>4</sub>C multilayer gratings have the same grating parameters, it is determined that the flat-field spectrometer equipped with the Ni/C multilayer grating has been well optimized for low energy down to 1 keV, while maintaining high resolution near 3.5 keV. This indicates that high resolution as well as wide coverage over the 1–3.5 keV range has been successfully achieved. Furthermore, the energy resolution of this spectrometer can be relatively easily improved by replacing the detector with one of higher spatial resolution, but is still inadequate for ultrahigh-resolution spectroscopy applications, such as chemical shift detection and resonant inelastic X-ray scattering (RIXS) measurements.

In summary, we developed a flat-field grating spectrometer with a pre-focusing mirror for use in the 1–3.5 keV range. The

VLS grating and the toroidal mirror have been coated with aperiodic Ni/C multilayers to cover this range at constant angles of incidence. The spectrometer performance was evaluated by synchrotron radiation reflectometry and by measuring various characteristic X-ray lines. It is concluded that the spectrometer is a promising tender X-ray spectroscopy instrument, capable of clearly and simultaneously observing X-ray emissions in the 1–3.5 keV range without any mechanical movement, and provides a new opportunity to perform various XES studies, such as in situ/operando measurements and single-shot measurements.

## Acknowledgments

The author thanks R. Ukita, H. Nishihara, H. Sasai, and T. Nagano of Shimadzu Corporation for preparation of grating substrates. Part of this work was conducted under the approval of the Photon Factory Program Advisory Committee (2014G531). This study was supported financially in part by JSPS KAKENHI (25790060, 15K04685).

## References

1. T. Imazono *et al.*, *Proc. of SPIE* **8848**, 884812 (2013).
2. M. Terauchi *et al.*, *Microscopy* **62**, 391 (2013).
3. T. Imazono *et al.*, *Appl. Opt.* **57**, 7770 (2018).
4. M. A. Green *et al.*, *Prog. Photovolt. Res. Appl.* **25**, 668 (2017).



# Formation of ablation structures on aluminum films by picosecond soft X-ray laser pulses

Masahiko Ishino

X-ray Laser Group, Department of Advanced Photon Research

The development of short-pulse lasers with picosecond or femtosecond duration has advanced dramatically. The direct interaction of a laser pulse with matter is ablation. As a result of the interaction, laser pulses produce high temperature and pressure, light emission, and ablation structures. One of the attractive and important subjects in laser-matter interaction is soft X-ray laser (SXRL) ablation, because the ablation threshold of the SXRL is lower than that of optical- or long-pulse lasers [1] and the modification structures depend on the target materials [2, 3]. In addition, the wavelength of the SXRL is shorter than that of optical lasers, such that the SXRL has an ability to draw characteristic nanometer-scale patterns directly on the material surface. The low ablation threshold is connected to the possibility of efficient surface machining. Therefore, it is important to study the ablation phenomena of short-pulse lasers for nanometer-scale applications such as surface machining with three-dimensional structures. However, to study the ablation process more deeply and accurately, many similar types of samples have to be prepared. In this paper, we report on experimental results of SXRL ablation of Al film occurring in a relatively low-fluence region [4]. The ablation structures were compared with those on a bulk target. Based on the experimental results and theoretical predictions, we discuss the growth process of the ablation structure.

Al film targets were fabricated by a vacuum evaporation method. Si wafers and polished LiF crystals were used for substrates. The nominal thickness of the deposited film was observed by a quartz oscillator thickness monitor. The actual film thickness was measured by a stylus surface profiler, and the evaluated film thickness was approximately 0.6  $\mu\text{m}$ .

The SXRL irradiation experiment was performed at the X-ray laser facility at Kansai Photon Science Institute. The SXRL was generated from Ag plasma media using an oscillator-amplifier configuration. The characteristics of the SXRL pulse were 13.9 nm in wavelength and 7 ps in pulse width. The SXRL pulse was focused on the sample surface using a Mo/Si multilayer-coated spherical mirror. The full width at half maximum of the focal spot was 30–40  $\mu\text{m}$  in diameter. Zr filters with various thicknesses (for example, 0.1 or 0.2  $\mu\text{m}$ , or combinations thereof) were used as X-ray attenuators. Typical fluences on the target surfaces, which were evaluated as averaged values, were estimated to be 10–30  $\text{mJ}/\text{cm}^2$ . The average fluence was derived from the irradiation energy divided by the focal spot size.

Figure 1 shows the ablation structures on the Al film observed by a scanning electron microscope (SEM). The ablation structure was formed by a single-shot of the SXRL pulse with the average fluence of 30  $\text{mJ}/\text{cm}^2$ . Two types of structures, i.e., ablation holes and projections (or protuberances or nanoparticles) were confirmed. A hole was formed by the high-intensity portion, and projections appeared in the lower-intensity parts. The distribution of the features of the focal pattern represented the distribution of the gain structure in the SXRL plasma, because the spherical mirror reconstructs a reduced image of the SXRL source. Therefore, the ablation structure had complex features. In

the SXRL concentrated-energy part, deep holes formed. Around the holes, nanometer-scale structures with rims appeared. A low-fluence case around the ablation threshold ( $\sim 15 \text{ mJ}/\text{cm}^2$ ) is shown in Fig. 2. Around the ablation threshold region, nanometer-scale projections are confirmed in micrometer size-modified areas within rims. The rims have heights of several hundred nanometers, and the heights of the rims have almost constant values, independent of the deposited pulse energy. These rims may be the remains of domes, which are linked to the spallation process by the short-pulse laser irradiation.

Based on the experimental result and the theoretical discussion [4], we anticipate one possibility of the formation of the ablation structure, such a nanometer-scale projection in the modified area and rims, by the SXRL irradiation. Figure 3 shows a growth model of the ablation structure on the Al surface. When the SXRL pulse with a fluence of  $F$  irradiates onto the Al surface, the SXRL is absorbed and creation of a heat-affected zone (HAZ) starts during the laser duration. In the case of SXRL ablation, we can consider that the absorbed fluence,  $F_{\text{abs}}$ , is equal to  $F$  owing to the strong interaction of soft X-rays with matter. When  $F_{\text{abs}}$  is small and significantly below the ablation threshold,  $F_{\text{abl}}$ , the cooling of the HAZ proceeds quickly because of the conductive cooling between the HAZ and target body. If  $F_{\text{abs}}$  is larger than the nucleation threshold,  $F_{\text{nuc}}$ , but smaller than  $F_{\text{abl}}$  ( $F_{\text{nuc}} < F_{\text{abs}} < F_{\text{abl}}$ ), nucleation takes place and foam appears in the HAZ. This foam remains under the surface [5]. When  $F_{\text{abs}}$  is slightly above  $F_{\text{abl}}$  ( $F_{\text{abl}} \leq F_{\text{abs}}$ ), the foam inflates and this inflation causes the expansion of the surface and the appearance of a dome structure. The swelling of each region of foam perturbs the melting layer of the HAZ, which causes the appearance of nanometer-scale projection structures. Then, the roof of the dome separates from the bottom of the HAZ, and a spallation shell appears around the 100-ps timescale [2, 6]. Because of the strong thermal contact between the crater (bottom of the HAZ) and target body, nanometer-scale projection structures freeze under the spallation shell before they are smoothed by surface tension. In contrast, the cooling of the spallation shell proceeds much more slowly than that of the crater, because cooling proceeds through the ring around the crater, where the spallation shell contacts with the target body. If  $F_{\text{abs}}$  is insufficient, the spallation shell freezes while contacting the target body. However, if  $F_{\text{abs}}$  is significantly above  $F_{\text{abl}}$ , the spallation shell will fly away. The radiative cooling rate is much smaller than the conductive cooling rate, such that the temperature of the spallation shell remains in a hot liquid state for a long time interval. High pressure exists in the domes before breaking and exists in the remaining domes. In the growing domes during the SXRL irradiation, a non-equilibrium state, such as warm dense matter, is created. To confirm such a physical interpretation, a detailed study of SXRL ablation will be needed. After carrying out systematic ablation experiments by using film targets and a femtosecond SXRL source, such as an X-ray free electron laser, we will report on the results.

Previously, has been indicated that the modification of the Al surface formed by the low-fluence region may occur without

ablation [7]. The zone of surface modification with nanostructures was determined by the melting threshold. The nanoscale surface modification is due to the splash of molten metal under the fluence/temperature gradient of the laser beam [7–9]. Such a modification is more appreciable with an X-ray laser pulse, as local temperature gradients may be larger than for an optical pulse, and the modification is considered to be formed in the lower-limit region of the spallation/ablation threshold. The modified structure formed by picosecond SXRL pulse exposure is quite particular, especially in a relatively low-fluence region.

It must be stressed that ablation structures obtained by 0.6- $\mu\text{m}$ -thick Al film were the same as those on bulk targets. By using films of sufficient thickness ( $> 0.5 \mu\text{m}$ ), we can obtain the same results as with bulk targets. This method does not require expensive surface polishing of the bulk target.

In this study, we irradiated SXRL pulses onto Al film, and compared the differences in the ablation structures between on the film and bulk surfaces. The ablation structures appearing on 0.6- $\mu\text{m}$ -thick Al films were the same as those on bulk targets.

The irradiation of SXRL pulses around the ablation threshold formed nanometer-scale projection structures in a micrometer size-modified area with rims. The heights of the rims are independent of the SXRL fluence, and have nearly constant values. Based on the spallation phenomenon, we proposed a growth model of the ablation structure on the Al surface. When the absorbed fluence is larger than the nucleation threshold, nucleation takes place and foam appears in the HAZ. The foam inflates and causes the expansion of the surface. The swelling of each region of foam perturbs the melting layer of the HAZ, which causes the appearance of nanometer-scale projection structures. The expansion surface layer separates, and a spallation shell appears. Nanometer-scale projection structures freeze under the spallation shell before they are smoothed by surface tension, because of the strong thermal contact with the target body. In contrast, the cooling of the spallation shell proceeds much more slowly than that of the crater, because of the weak thermal contact with the target body through the ring around the crater. When the absorbed fluence is significantly above the ablation threshold, the spallation shell will fly away, which is called spallation.

## Acknowledgments

The author thanks Prof. N. Inogamov, Prof. S. Tamotsu, Dr. V. Zhakhovsky, Dr. N. Hasegawa, Dr. I. Skobelev, Prof. A. Faenov, Dr. T. Pikuz, Dr. K. Mikami, Dr. T. Kawachi, and Dr. M. Nishikino for their deep contribution to this work.

## References

1. A.Ya. Faenov *et al.*, Appl. Phys. Lett. **94**, 231107 (2009).
2. M. Ishino *et al.*, J. Appl. Phys. **109**, 013504 (2011).
3. M. Ishino *et al.*, Appl. Phys. A **110**, 179–188 (2013).
4. M. Ishino *et al.*, Appl. Phys. A **124**, 649 (2018).
5. N.A. Inogamov *et al.*, Eng. Fail. Anal. **47**, 328–337 (2015).
6. V. V. Zhakhovskii *et al.*, JETP Lett. **87**, 423–427 (2008).
7. S. V. Starikov *et al.*, Appl. Phys. B **116**, 1005–1016 (2014).
8. G. Norman *et al.*, J. Appl. Phys. **112**, 013104 (2012).
9. S. V. Starikov and V. V. Pisarev, J. Appl. Phys. **117**, 135901 (2015).

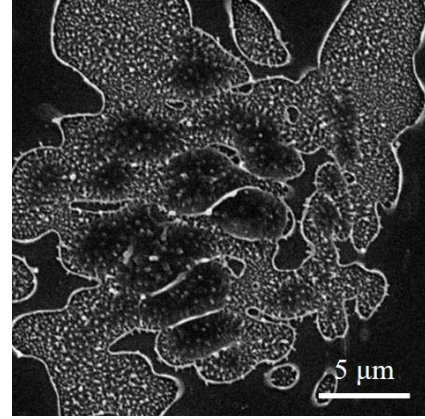


Fig. 1. SEM image of the ablation structure of Al film formed by the SXRL pulse with an average fluence of 30 mJ/cm<sup>2</sup>.

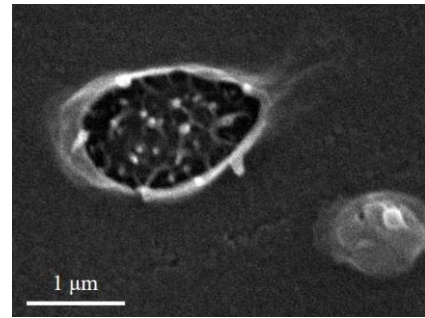


Fig. 2. Magnified SEM image of the ablation structures on Al film by the SXRL pulse with a fluence around the ablation threshold.

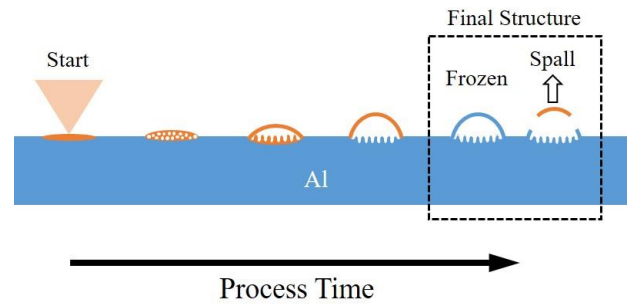


Fig. 3. Growth model of ablation structure on the Al surface. Absorption of the SXRL pulse energy causes the creation of the HAZ. If the  $F_{\text{abs}}$  is larger than  $F_{\text{nuc1}}$ , foam appears in the HAZ. When  $F_{\text{abs}}$  is slightly above  $F_{\text{abl}}$ , the inflation of the foam causes the expansion of surface and the appearance of the dome structure. If  $F_{\text{abs}}$  is insufficient, the spallation shell freezes on the surface. If  $F_{\text{abs}}$  is significantly above  $F_{\text{abl}}$ , then the spallation shell flies away.

# Research Activities in Department of Quantum Beam Life Science

Naoya Shikazono (Director)

## Department of Quantum Beam Life Science

---

In the Department of Quantum Life Science, the three laboratories use quantum beams, such as ionizing radiations and lasers, as well as computer simulations to advance fundamental research contributing to the development of life science and also applied research useful for society, such as medical care. Figure 1 shows an overview of the main focus of research in the department. Based on the very small and very fast processes after irradiation, groups in the department mainly study the molecular dynamics of cellular molecules and also cellular responses to various stimuli. The research contributes to basic life science, by proposing novel ideas in radiation biology, and revealing the underlying molecular mechanisms of various biological phenomena. Our activities are also expected to lead to innovative developments of laser equipment in medical care.

In the Radiation-Induced DNA Damage Group, in order to clarify the mechanism by which radiation affects living organisms, the members are now focusing on the development of an efficient detection method of a specific type of DNA damage that is considered to be difficult to repair by the cell. The group's interests are not only limited to the detection of DNA damage, but also relate to what is happening at the very early stages after irradiation. This time scale is well before the generation of DNA damage, and the group is mainly looking at the movement of secondary electrons with Monte-Carlo simulations. The latest findings regarding the effects of the heavy-ion track potential are shown in this annual report. Another topic shown in the report is on the configurational fluctuation of the water molecules. The behavior of water confined in a reverse micellar solution has been studied by absorption spectroscopy.

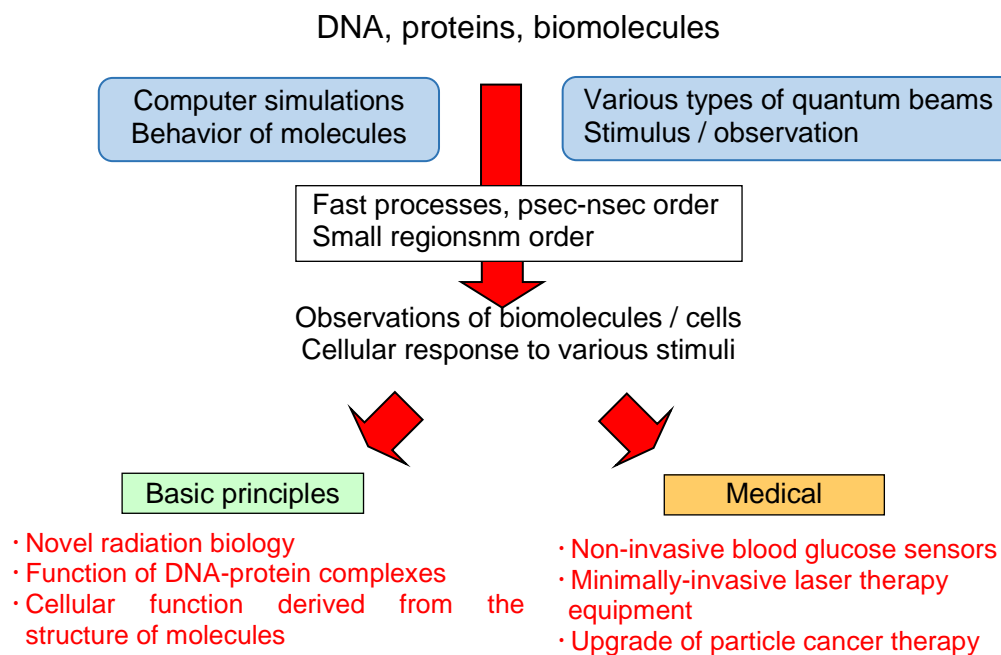
The Molecular Modeling and Simulation Group is aiming to understand the *in vivo* function of biomolecules from the atomic level. The group uses computer simulations and bioinformatics together with scattering data obtained by various types of radiation, such as X-rays, neutrons, and electrons. The main research target is to discover how the dynamics of protein/DNA/RNA complexes relate with transcription, translation, replication, and repair. The group has been working on the nucleosome dynamics and has found that the dimethylation of arginine has a strong effect thereon. The details are shown below in this annual report. Another topic with which the group has been engaged is the stability of the nucleosome. They found that the transcriptional direction strongly correlates with the DNA sequence wrapped around the nucleosome core. The results are also described later in this report.

One of the research targets of the Medical Laser Applications Group is to develop a palm-sized non-invasive blood glucose sensor by combining an advanced solid-state laser and optical parametric oscillation technology. The sensor would not require blood sampling, and would therefore need not to pierce the needle into one's finger or hand. The sensor device allows the measurement of blood glucose only by touching it with a finger. The development of such a device would greatly impact the field of medical care. Another main research target of this group is to develop a microspectroscopic imaging system for histopathology using a mid-IR laser. The apparatus aims to feasibly distinguish normal and tumor tissues in a sliced sample. The current status of the development of this imaging system is also presented in this annual report.



## Department of Quantum Beam Life Science

The department aims to contribute to the elucidation of the basic principles of life, as well as to the application in the field of medical care, using cutting-edge quantum beam technology and advanced computer simulations.



# Distinct Influence of Arginine Dimethylation on Nucleosome Dynamics using All-atom Simulation and Kinetic Analysis

Zhenhai Li and Hidetoshi Kono

Molecular Modeling and Simulation Group, Department of Quantum Beam Life Science

Eukaryotic cells store the genomic DNA in the repeating basic units, nucleosomes, each of which consists of a histone octamer core and DNA wrapped around the core  $\sim 1.7$  times. The core is formed by the globular domains of two copies each of the H3, H4, H2A, and H2B histone proteins[1]. The stability and dynamics of a nucleosome are regulated by the interaction between histone proteins and DNA, which sterically obstructs the access to the genes stored in the nucleosomal DNA and impedes both DNA transcription and replication[1–3]. Different mechanisms have been found to alter DNA–histone core interactions: replacement of canonical histones with their variants and post-translational modifications (PTM) in the histone core. Histone proteins are found to be heavily decorated with PTMs, including acetylation, methylation, phosphorylation, ubiquitinylation, etc. These PTMs either directly affect the histone–DNA interaction or provide a scaffold to recruit regulatory proteins, and eventually promote or repress gene expression and replication. The downstream events of the PTMs are determined by the types and locations of the modifications[4, 5]. Recently, certain PTMs in histone globular domains were identified, such as PTMs on Tyr 41, Arg 42 and Lys 56 of H3, and Lys 77 and Lys 79 of H4, which are all located at the DNA–histone interface, and Lys 91 and Lys 92 of H4 located at the histone–histone interface[4, 5], though numerous studies have focused on PTMs in the intrinsically unstructured histone tails[6, 7]. Among these amino acids, Arg 42 of H3 (referred to as R42), which is located at the entry/exit region of a nucleosome, is conserved across species[8] and was found to be dimethylated in mammalian cells[9, 10]. Casadio et al. showed that the asymmetric dimethylation of R42 (R42me2a) *in vitro* promotes gene transcription[9]. Later, Yaseen et al. found the R42 in a host cell nucleus can be dimethylated by a micobacteria-secreted protein, Rv1988, which in turn represses the host gene transcription, and eventually impedes the host immune response[10].

The arginine can be methylated twice symmetrically or asymmetrically, and owing to the possible rotation around the central carbon–nitrogen bond in the guanidinium group, two symmetric dimethylarginine stereoisomers, anti-syn and anti-anti symmetric dimethylarginine, exist [11]. However, because it is difficult to examine the atomic arrangement of dimethylated R42 experimentally and numerous molecular dynamics (MD) simulations have been performed to study the PTM in nucleosomes, showing the advantage of MD methods in this field[12–16], we carried out a series of replica-exchange molecular dynamics (REMD) simulations on a group of nucleosome variants, with and without modifications of R42. These include the unmodified R42, R42me2a, two stereoisomers of R42me2s (indicated by anti-anti R42me2s and anti-syn R42me2s), and a mutant, R42A (Fig. 1).

The REMD simulations clearly showed that the R42me2a and R42A (Arg was mutated to Ala) nucleosome adopted a relatively opened conformation compared to the unmodified

nucleosome (Fig. 1B, C&D). By adopting the methods of protein folding kinetics analysis with REMD, we obtained the opening/closing rates of the entry/exit DNA (Fig. 2A&B). The kinetics show that the asymmetric methylations and R42A mutation promoted the opening rate and impeded the closing rate of the nucleosome, which was not observed in the symmetrically methylated nucleosome (Fig. 2C). These findings

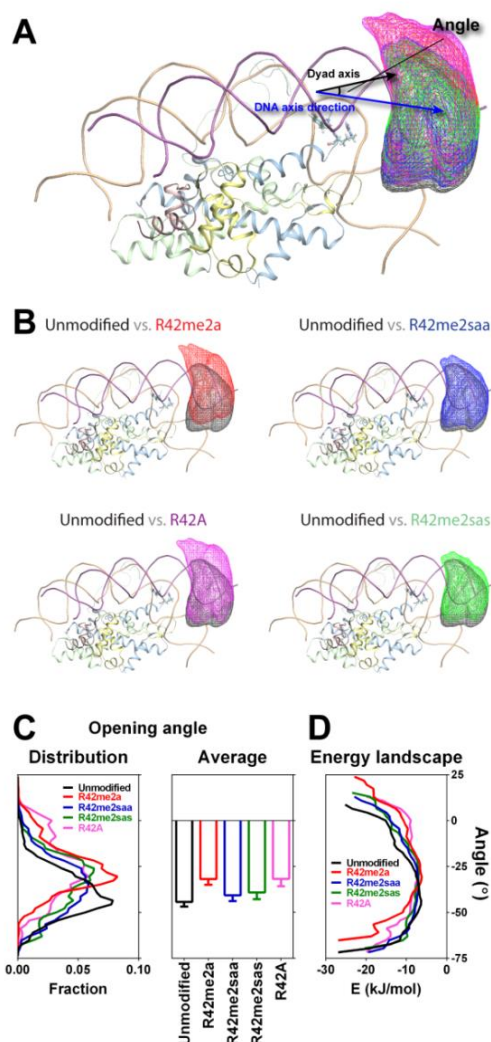


Fig. 1. Spatial distributions of linker DNA tip obtained by REMD simulations: (A) superposition of unmodified R42, R42me2a, R42A, R42me2saa, and R42me2sas nucleosome variants; (B) superposition of unmodified and each of them; (C) the opening angle distribution and average; (D) the energy landscape.

highlight the distinct effects of R42me2a and R42me2s modifications on the nucleosome structure and dynamics, which explains the distinct gene activities observed in previous studies[9,10]. Furthermore, this study unravels the delicate mechanism of nucleosome structure regulation by the dimethylation of R42 and provides an understanding of the different effects from the different dimethylation constitutional isomers on the atomic level.

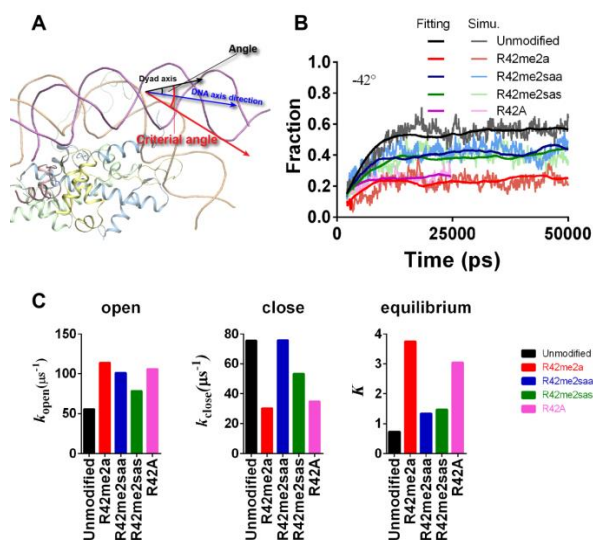


Fig. 2. A. A criterial angle is an angle between the selected criterial and the dyad axes, which defines the nucleosome DNA opening state. The nucleosomal DNA is defined as open when the DNA axis is above the criterial axis, and vice versa. B. Trajectories of the closed fraction of all the replicas (thinner lines) of the nucleosomal DNA with a criterial angle of  $-42^\circ$ . Different nucleosomes and the fitted fraction trajectories (thicker lines) are shown in different colors. C. Computed opening rates (left), closing rates (middle), and equilibrium constants (right) with a criterial angle at  $-42^\circ$ . The color code in (B, C) is the same as in Figure 1C.

## Acknowledgments

This research was funded by the Ministry of Education, Culture, Sports, Science and Technology (MEXT) Strategic Programs for Innovative Research, Computational Life Science and Application in Drug Discovery and Medical Development (hp140029, hp150233, hp160223, hp170255) and by JSPS KAKENHI (No. 25116003).

## References

1. Luger, K., et al., *Crystal structure of the nucleosome core particle at 2.8 Å resolution*. Nature, 1997. **389**(6648): p. 251-260.
2. Simpson, R.T., *Nucleosome positioning can affect the function of a cis-acting DNA element in vivo*. Nature, 1990. **343**(6256): p. 387-389.
3. Li, R. and M.R. Botchan, *Acidic transcription factors alleviate nucleosome-mediated repression of DNA replication of bovine papillomavirus type 1*. Proceedings of the National Academy of Sciences of the United States of America, 1994. **91**(15): p. 7051-7055.

4. Bowman, G.D. and M.G. Poirier, *Post-translational modifications of histones that influence nucleosome dynamics*. Chemical reviews, 2015. **115**(6): p. 2274-2295.
5. Lawrence, M., S. Daujat, and R. Schneider, *Lateral thinking: how histone modifications regulate gene expression*. Trends in Genetics, 2016. **32**(1): p. 42-56.
6. Musselman, C.A., et al., *Perceiving the epigenetic landscape through histone readers*. Nature structural & molecular biology, 2012. **19**(12): p. 1218-1227.
7. Bártová, E., et al., *Histone modifications and nuclear architecture: a review*. Journal of Histochemistry & Cytochemistry, 2008. **56**(8): p. 711-721.
8. Malik, H.S. and S. Henikoff, *Phylogenomics of the nucleosome*. Nature Structural & Molecular Biology, 2003. **10**(11): p. 882-891.
9. Casadio, F., et al., *H3R42me2a is a histone modification with positive transcriptional effects*. Proceedings of the National Academy of Sciences of the United States of America, 2013. **110**(37): p. 14894-14899.
10. Yaseen, I., et al., *Mycobacteria modulate host epigenetic machinery by Rv1988 methylation of a non-tail arginine of histone H3*. Nature communications, 2015. **6**: p. 8922.
11. Fuhrmann, J., K.W. Clancy, and P.R. Thompson, *Chemical biology of protein arginine modifications in epigenetic regulation*. Chemical reviews, 2015. **115**(11): p. 5413-5461.
12. Qiu, Y., et al., *Solution structure of the Pdp1 PWWP domain reveals its unique binding sites for methylated H4K20 and DNA*. Biochemical Journal, 2012. **442**(3): p. 527-538.
13. Collepardo-Guevara, R., et al., *Chromatin unfolding by epigenetic modifications explained by dramatic impairment of internucleosome interactions: a multiscale computational study*. Journal of the American Chemical Society, 2015. **137**(32): p. 10205-10215.
14. Grauffel, C., R.H. Stote, and A. Dejaegere, *Molecular dynamics for computational proteomics of methylated histone H3*. Biochimica et Biophysica Acta - General Subjects, 2015. **1850**(5): p. 1026-1040.
15. Ikebe, J., S. Sakuraba, and H. Kono, *H3 histone tail conformation within the nucleosome and the impact of K14 acetylation studied using enhanced sampling simulation*. PLoS computational biology, 2016. **12**(3): p. e1004788.
16. Shimojo, H., et al., *Extended string-like binding of the phosphorylated HPIa N-terminal tail to the lysine 9-methylated histone H3 tail*. Scientific reports, 2016. **6**: p. 22527.

# Transcriptional Direction is Likely to be Encoded by Sequence as in a Form of Nucleosome Stability

Luo Di and Hidetoshi Kono

Molecular Modeling and Simulation Group, Department of Quantum Beam Life Science

We have been studying the expression of eukaryotic genes in cell nuclei. In the nucleus, the genome is stored as chromatin, whose fundamental structural unit is a nucleoprotein, a so-called nucleosome. Differentiated cells express their specific genes though all the cells in our body essentially have a common genome. What mechanism determines or controls which genes are expressed? This is one of the central topics in biology. We realized that the base composition has a biasing in +1 nucleosomes of yeast. In nucleosomes, AA (or TT) or AAAA (or TTTT) sequences are rich in the first half of nucleosomal DNA (**Fig. 1**) [1]. This study investigates the meaning of these sequence patterns in the gene expression.

Eukaryotic genes are organized in arrays of nucleosomes initiated from their transcription starting sites (TSS). The first nucleosomes in these arrays, termed as +1 nucleosomes, are highly positioned, and lead to downstream nucleosomes (i.e., +2, +3 ...) of gradually decreased positioning. Such a pattern of nucleosome organization of genes has been found in many species, although the reason behind this is still under investigation.

As the first hurdle to DNA transcription, +1 nucleosomes have been found to play critical roles in gene regulation. It has been reported that +1 nucleosomes interfere in transcription elongation by enhancing RNA Polymerase II (Pol II) pausing at the promoter-proximal region. The stall enhanced by +1 nucleosomes can serve as a break to recruit factors for transcription elongation and pre-mRNA processing.

Furthermore, genome-wide analyses have shown that +1 nucleosomes, especially of active genes, are largely subjected to histone variant substitutions and histone modifications. The histone variant H2A.Z is found to be prevalent in the +1 nucleosomes of yeast; by replacing the canonical histone H2A, it can stimulate histone turnover and destabilize +1 nucleosomes

for gene activation. Histone modifications such as acetylation, methylation, and phosphorylation have been extensively studied in terms of their effects to perturb nucleosome structure and/or regulate molecular recognition by transcription factors and chromatin remodelers. The frequent presence of these modifications in the +1 nucleosomes is believed to play an important role in modulating DNA accessibility in nucleosomes and facilitating sequential binding events for Pol II transit. Nevertheless, spontaneous site exposures of nucleosomes have also been observed under physiological conditions *in vitro*, indicating the inherent dynamic nature of nucleosomes. DNA sequence, which can encode DNA-histone interactions and DNA bending mechanics, should also play a non-negligible role. In this work, we examined the role of DNA sequence on DNA accessibility in the +1 nucleosomes of budding yeast by using micrococcal nuclease (MNase).

MNase is an endo- and exo-nuclease, which can specifically break down the phosphodiester bond between adjacent nucleotides in the presence of calcium ions and in a pH range from 8.6 to 10.3. The crystal structure of MNase complexed with a 3', 5'-biphosphate thymidine shows that MNase engulfs the thymine base into a binding pocket and exposes the leaving phosphate group toward a calcium ion. MNase cleaves DNA in a single-stranded manner. When the substrate is a double helix, the original DNA base pairing and base stacking must be interrupted such that a single DNA base can be inserted into the binding pocket, forming a proper binding complex for cleavage. Because the dissociation of base pairing, deformation of base stacking, and accommodation of a DNA base at the binding pocket are apparently sequence-dependent, MNase exhibits evident sequence preference as reported earlier. Despite this, MNase has been successfully used as a probe to detect DNA accessibility in DNA foot-printing assays. Not only histones but also other DNA-binding proteins have demonstrated their ability to shield DNA from MNase digestion.

In this study, we designed a wet experiment in which we used MNase to probe the +1 nucleosomes of yeast *in vitro*, to investigate the correlation between DNA sequence and nucleosome site exposure mirrored by MNase digestion [1]. Specifically, we investigated the cleavages made by MNase on the nucleosome core structures. This topic may have been overlooked in studies where MNase was used for chromatin digestion and only the mononucleosomal-sized DNA fragments were sifted for nucleosome positioning mapping. One of the direct consequences is exemplified by the observed discrepancy of nucleosome positioning near the 5'-nucleosome-free region (NFR) at very low and high MNase concentrations. Because cleavages made on the nucleosome core structures could lead to an underestimated positioning, the features of nucleosomes that are both well-positioned and dynamically site-exposed may not be fully recognized. In short, our results depict how MNase cleaves nucleosomal DNA at base pair resolution. We find that the digestion is dictated by the MNase sequence preference at the end regions, whereas it is driven by a bending-resistant

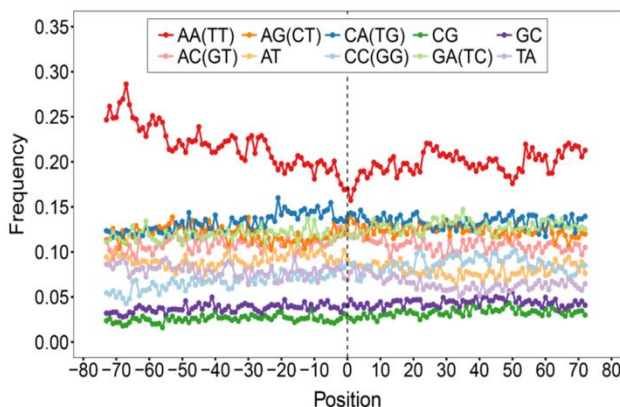


Fig. 1. Frequencies of occurrence of dinucleotide steps at each position in the +1 nucleosomes of yeast. The frequencies of the AA/TT dinucleotide step are distinctively higher than those of the other dinucleotide steps at all positions.



sequence element at the internal sites in the early stage of digestion. This bending-resistant sequence element is the AA or AAAA sequence.

To further demonstrate that AA or AAAA regions are digested by MNase more frequently, we carried out a mutation analysis. One +1 nucleosomal DNA sequence of yeast, “nuc19,” was selected as the wild type because it does not have these sequence features and did not exhibit characteristic digestion patterns in the digestion assays of the 20 +1 nucleosomes used in this study. Four mutants were designed by replacing the end (position: 0–15) and a further inward site (position: 14–29) on the “+” strand of nuc19 with TA-repeated and imperfect poly-A sequences, respectively. The wild type and four mutants were incubated with MNase individually for 1 and 3 min, and the digestion products were sequenced via the paired-end sequencing approach.

As shown in **Fig. 2** (upper panel) AAs at the internal site (mut\_4) were still evenly cleaved owing to nucleosome site exposure, and the digestion in this region was clearly more frequent than the digestion of the same region in the wild-type sequence.

Because AA/TT is abundant at the entry site of +1 nucleosomes in yeast, we propose that this sequence element might be utilized in gene regulation to facilitate DNA unwrapping for transcription. Here, we associate the transcription levels of yeast genes reported in an earlier study with the AA/TT contents in their +1 nucleosomes. As shown in [1], for the low-transcribed genes, for example, there are 368 of them associated with a +1 nucleosome of a greater AA/TT content in the entry-to-dyad region (than the exit-to-dyad region). On the contrary, there are 257 low-transcribed genes

with more AA/TTs in the exit-to-dyad region in their +1 nucleosomes. This difference in the numbers of genes gives a ratio of 1.43. It is found that when the transcription level advances, the ratio also increases. For the highly transcribed genes, the ratio reaches 1.99, indicating that nearly two thirds of the highly transcribed genes are coupled with a +1 nucleosome with more AA/TTs in the entry-to-dyad region. Similar results were obtained for the AAAA/TTTT element.

This analysis unveils a coincidence in the yeast genome that the highly transcribed genes are more likely to position more AA/TTs in the entry-to-dyad region than the exit-to-dyad region in their +1 nucleosomes. As AA/TT can induce nucleosome site exposure, this positioning could lower the overall DNA-histone affinities in the entry-to-dyad region of +1 nucleosomes to facilitate DNA dissociation for Pol II transit.

## Acknowledgments

The author is sincerely grateful to all the lab members for their critical comments and suggestions regarding this work. This research was funded by the Ministry of Education, Culture, Sports, Science and Technology (MEXT) Strategic Programs for Innovative Research, Computational Life Science and Application in Drug Discovery and Medical Development (hp170255, hp180191), by JSPS KAKENHI (No. 25116003), and by AMED (JP18am0101106).

## References

1. D. Luo, D. Kato, J. Nogami, Y. Ohkawa, H. Kurumizaka and H. Kono, *Nucleic Acids Res.* (2018) **35**, 39-50.

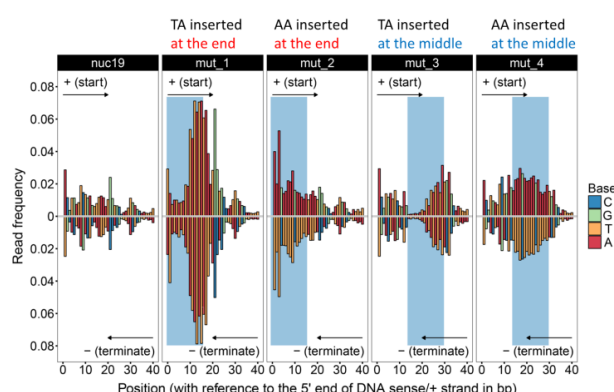


**Fig. 2.** Read frequencies of nuc19 and its four mutants from 1-min digestion assays. The digestion products were sequenced via the paired-end sequencing approach. The mutated regions are shaded in blue. The frequencies of reads starting from each position in the range from 0 to 40 on the “+” strand are shown in the upper panels. The frequencies of reads terminating at each position on the opposite strand (“-”) of the mutated regions are shown in the lower panels.

# Quantum physics of life: Water vitrifies in a cell-like confinement

Hiroshi Murakami

Radiation-Induced DNA Damage Group, Department of Quantum Beam Life Science

## 1. Introduction

Our research purpose is to study quantum mechanical effects, such as quantum coherence and entanglement, on biological functions in cells using a reverse micelle, which is a simplified model of cells (Fig.1). One of our foci is the thermal noise in cells, because quantum mechanical effects disappear with thermal noise and because there is a conventional supposition that the intracellular environment has high thermal noise due to the liquid state at high temperatures. This report addresses the supposition, and a top-line conclusion of the present study is that water can vitrify locally on the nanoscale in cells.

Recently, much attention has been paid to the fact that cytoplasm shows glass-like properties [1-3]. This is believed to be attributed to molecular crowding in cells [4]. This raises a question of how intracellular water contributes to the glassy behavior because water is a major constituent and essential for biological reactions. However, the glassy behaviors of cytoplasm have hardly been studied at the molecular level owing to the complexity of intracellular contents. A liquid-glass transition is a change from a liquid to a solid state while maintaining the structure of the liquid at the transition point, that is, random structures; various types of substances from liquids to biopolymers exhibit liquid-glass transitions; however, understanding of the transition has been one of the most important unsolved problems despite a long history of glasses [5].

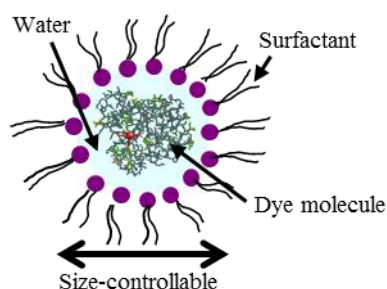


Fig.1. Schematic cross-section diagram of reverse micelles. The reverse micelle is a nanoscopic water droplet covered by a membrane formed by the self-assembly of surfactant molecules whose hydrophilic group faces the water. A water-soluble molecule such as a dye molecule can be dissolved in the water droplet.

In contrast with intracellular water, nanoconfined water using solid surfaces has been extensively studied at room temperature because nanoconfined water is ubiquitous and an important state of water in science and technology [6-9]; so far, it has been shown that the motion of nanoconfined water slows down to the millisecond scale, which is comparable with the motion in supercooled water, and that the water does not vitrify at room temperature. As for nanoconfined water in reverse micelles near the smallest size, that is, water-droplet sizes

around 2 nm, we have pointed out from absorption spectroscopy [10] that the water is in the glassy state at room temperature, and then definitively confirmed it using persistent spectral hole-burning (PHB) spectroscopy [11].

In the present study, we have made size-dependent measurements of PHB spectroscopy for a dye-molecular probe encapsulated in water/AOT/isooctane reverse micelle in order to examine a glassy state of nanoconfined water for larger sizes. PHB spectroscopy allows us to unambiguously determine whether or not the surroundings of the probe molecule are in the glassy state only by observing the site-selective effect, without any data analysis and fitting [12]. We define the glassy state of water in the reverse micelle by the fact that the water has a relaxation time longer than at least several minutes, that is, a laboratory time scale.

## 2. Methods

The dye-containing reverse micellar solution was prepared using the injection method [10, 13]. Rhodamine 6G, AOT [=bis (2-ethylhexyl) sulfosuccinate], isooctane, and sterile Millipore-filtered water were used as a dye, surfactant, oil, and water, respectively. The size of the reverse micelle was adjusted by the water-to-surfactant molar ratio ( $w_0$ ).

An optical parametric oscillator pumped with the third-harmonic pulse of a nanosecond Q-switched Nd:YAG laser was used as a variable-wavelength excitation source for PHB spectroscopy. PHB spectra were obtained by the difference between absorption spectra before and after the laser irradiation, where the absorption spectra were measured with an experimental system constructed by a combination of white light from a xenon lamp and spectrometer [11]. We reconstructed the PHB spectroscopy setup to increase the signal-to-noise ratio of the spectra, compared with that in the previous study [11], which allowed us to obtain PHB spectra with a larger site-selective effect, in other words, less saturation effect due to strong laser excitation.

## 3. Results and discussion

PHB spectra obtained with excitation at  $18182\text{ cm}^{-1}$  at  $w_0 = 2$  and 8 and at room temperature, together with the absorption spectra, are depicted in Fig.2. The PHB spectra do not agree with the absorption ones at the two  $w_0$  values. They are shifted to low frequencies from the absorption spectra. This is the site-selective effect with the low-frequency excitation due to the glassy state of the surroundings of the dye molecule. The electronic transition energy of the dye molecule depends on a site at which the molecule resides in the glassy system, because the atomic configurations of the surroundings of the molecule differ among the sites. Some of the dye molecules are resonantly excited by a narrow-band laser at the frequency, and then undergo a photobleaching. The PHB spectrum is originated from the dye molecules subjected to the site-selective excitation,



and so it is shifted from the absorption spectrum originated from all the dye molecules. On the other hand, if the system is in a liquid state, the shift of the PHB spectrum disappears owing to the relaxation process, that is, the PHB spectrum agrees with the absorption spectrum. Thus, the water surrounding the dye molecule is in a glassy state below at least  $w_0 = 8$ . We estimate the structural parameters such as the water-droplet size and the number of water molecules for the reverse micelle under the assumption that the dye molecule is a sphere of 1-nm diameter, following the method proposed by us [13]. The droplet diameter is  $\sim 1.6$  nm at  $w_0 = 2$  and  $\sim 3.3$  nm at  $w_0 = 8$ , and the number of water molecules is  $\sim 80$  at  $w_0 = 2$  and  $\sim 830$  at  $w_0 = 8$ .

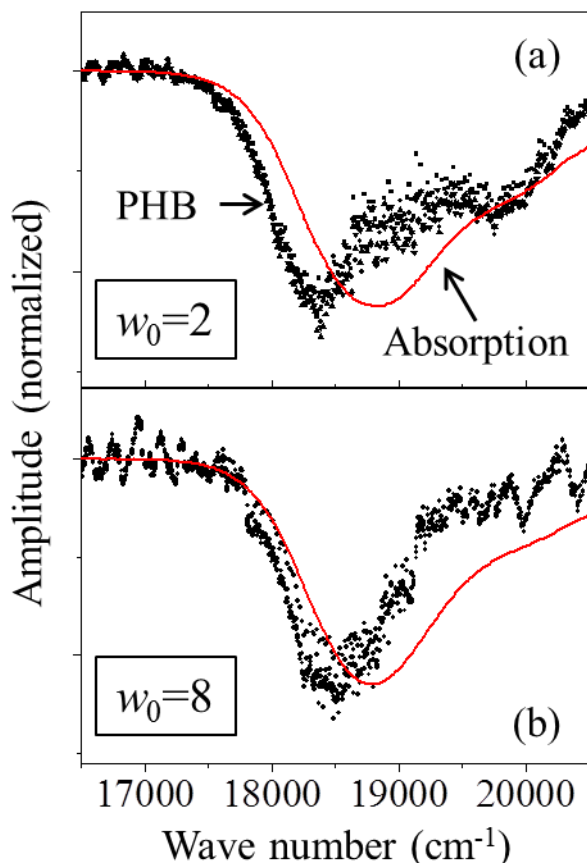


Fig.2. Comparison between PHB (dots) and absorption (line, inverted for comparison) spectra of R6G/RM at two  $w_0$  values and at ambient temperature. The PHB spectra were obtained at the excitation frequency of  $18182 \text{ cm}^{-1}$ .

It is surprising that the water in the reverse micelle vitrifies because the reverse micelle is dispersed not in a solid but in a liquid oil; hence, reverse micellar solutions are called soft materials. However, we consider that the nature of soft materials is responsible for the glassy state of nanoconfined water, where the flexibility in the molecular configuration of the dye and surfactant molecules associated for the confinement is a key factor for the formation of the glassy state. It is thought to be necessary for the glassy state that the water molecules network not only with each other but also with the interfacial molecules through hydrogen bonds. Moreover, the whole network will be formed if the configuration of the molecules involved is refined with the configurational flexibility. This is the case for R6G/RM. As for nanoconfined water using solid interfaces, the network between the water and interface would be incomplete because of a lack of the constituent atoms of the interface. This could be the

reason why the glassy state of nanoconfined water has never been observed in the confinement using solid interfaces although such nanoconfined water has extensively investigated.

Nanoconfined water between hydrophilic biopolymers will be ubiquitous in cells under the molecular crowding [4]. Therefore, the present result observed in a soft material leads to the idea that water can vitrify locally at the nanoscale in cells, and lets us recall the claim that studies of protein molecules in dilute reconstituted systems overlook a fundamental mechanism underlying the biological function in cells. In a dilute aqueous solution, the solvent water of proteins displays very fast motions on the picosecond scale, whereas it is considered from the present study that the water confined between proteins in cells exhibits significant slowing down in its motion. Thus, the next questions are how glass-like nanoscopic water appears in cells and how biopolymers behave in glass-like water at physiological temperatures, and finally it will be interesting to consider the quantum effect on biological functions from a viewpoint of “glass-like cells.”

### Acknowledgments

The author thanks Yuko Kanahara for her assistance with the experiments. This study was partly supported by Grants-in-Aid for Scientific Research (Kakenhi) (Grant No.26600017).

### References

1. Fabry et al., *Scaling the Microrheology of Living Cells*, Phys. Rev. Lett., **87**, 148102-1-4 (2001).
2. Zhou et al., *Universal behavior of the osmotically compressed cell and its analogy to the colloidal glass transition*, Proc. Natl. Acad. Sci. USA, **106**, 10632–10637 (2009).
3. Parry et al., *The Bacterial Cytoplasm Has Glass-like Properties and Is Fluidized by Metabolic Activity*, Cell, **156**, 183–194, (2014).
4. R. J. Ellis and A. P. Minton, *Join the crowd*, Nature **425**, 27–28 (2003).
5. C. A. Angell, *Formation of glasses from liquids and biopolymers*, Science **267**, 1924–1935 (1995); P. W. Anderson, in *Viewpoint: the future, through the glass lightly*, ibid. 1615–1616.
6. Gallo et al., *Glass transition and layering effects in confined water: A computer simulation study*, J. Chem. Phys. **113**, 11324–11335 (2000).
7. Li et al., *Nonlinear Viscoelastic Dynamics of Nanoconfined Wetting Liquids*, Phys. Rev. Lett. **100**, 106102-1–4 (2008).
8. Khan et al., *Dynamic Solidification in Nanoconfined Water Films*, Phys. Rev. Lett. **105**, 106101-1–4, (2010).
9. M. Kageshima, *Layer-resolved relaxation dynamics of confined water analyzed through subnanometer shear measurement*, Europhys. Lett., **107**, 66001-1–6 (2014).
10. Murakami et al., *Nanometer-scale water droplet free from the constraint of reverse micelles at low temperatures*, Phys. Rev. E **88**, 052304-1–8 (2013).
11. Hiroshi Murakami, *Persistent optical hole-burning spectroscopy of nano-confined dye molecules in liquid at room temperature: Spectral narrowing due to a glassy state and extraordinary relaxation in a nano-cage*, J. Chem. Phys. **148**, 144505-1–12 (2018).
12. *Persistent spectral hole-burning: science and applications*, edited by W. E. Moerner (Springer-verlag, Berlin, 1988).
13. Murakami et al., *Determination of Structural Parameters of Protein-Containing Reverse Micellar Solution by Near-Infrared Absorption Spectroscopy*, J. Phys. Chem. B **115**, 5877–5885 (2011).

# Effect of track potential on the motion and energy flow of secondary electrons created from heavy-ion irradiation

Kengo Moribayashi

Radiation-Induced DNA Damage Group, Department of Quantum Beam Life Science

## 1. Introduction

Cancer therapy using heavy ions is more body-friendly than treatments using any other types of radiation, such as  $\gamma$ -rays or protons, because the relative biological effectiveness (RBE) of heavy ions is higher; that is, a smaller dose is required with this therapy. In an effort to determine the reason for the higher RBE of heavy-ion beams, it has been postulated that heavy-ion irradiation creates more clustered DNA damage, which raises the rate of cell death. Here, clustered DNA damage is defined as multiple damaged sites within a region corresponding to a DNA length of several nanometers. However, it is still unclear when, where, and how such clustered DNA damage is created. We have therefore been studying the motion of secondary electrons using simulations in order to determine the spatial distribution of the energy deposition created by heavy-ion irradiation. Here, a secondary electron is defined as an electron created by incident-ion impact ionization. Because secondary electrons carry the energy deposited from the incident ion into the target, we expect the spatial distribution of the energy deposition produced by the secondary electrons to be related to the spatial distribution of DNA damage due to heavy-ion irradiation.

During irradiation by heavy ions, numerous molecules in the target are ionized along an incident heavy-ion path, and a strong electric field is formed by the positive charges of the molecular ions near this path. The potential produced from this electric field has been called the “track potential.” Kimura *et al.* [1] concluded from their measurements of secondary-electron yield that slow secondary electrons are trapped by the track potential. That is, the track potential affects the motion of the secondary electrons and thus changes the spatial distribution of energy deposition.

We incorporated the track potential into a simulation model and demonstrated that secondary electrons are trapped by the track potential [2,3]. In order to verify the validity of our model, we compare our simulations [2] with the measurements for secondary electron yield [1] when  $E_{ion} = 500$  keV/u, where  $E_{ion}$  is the energy of the incident ion. In this report, we treat cases with  $E_{ion} = 3$ –10 MeV/u and determine not only the number of secondary electrons [2, 3] but also the energy flow escaping the track potential, with the aim of elucidating the spatial distribution of energy deposition due to heavy-ion irradiation [3]. The energy flow simulations shown here are expected to enable us to quantitatively understand how our model produces the spatial distribution of energy deposition and the radial dose distribution [4] due to the irradiation of heavy ions.

## 2. Simulation model

The main advantage of our model is the incorporation of the track potential [2, 3], whereby we treat individual neutral

molecules, individual molecular ions, and individual free electrons in the target. In our model, the track potential is produced from the Coulomb interactions between individual charged particles and individual electrons. In contrast, conventional simulations employ a continuum target, and the track potential is ignored, to the best of our knowledge. We believe that our simulation model employed in this report has become possible in the 21<sup>st</sup> century because it takes a few days to simulate the irradiation of one heavy ion, even using modern super computers.

The procedures of our model are summarized here. (i) We set up positions of water molecules to obtain the liquid water density in this target. (ii) A heavy ion enters the target and the time  $t$  is set to 0. (iii) We consider the collision processes between this incident ion and individual molecules. (iv) When we judge that ion impact ionization occurs, we produce a molecular ion and a secondary electron. At the same time, the initial energy and emission angle of the secondary electron produced here are determined. (v) We also examine the change of states of water molecules due to electron impact. (vi) Procedure (iv) is executed after we judge that the electron impact ionization occurs. (vii) We reduce the energy of the electrons according to electron impact processes. (viii) The electron velocities are changed by the track potential. (ix) We add  $\Delta t$  to  $t$  and move the incident ion and the electrons. (x) Procedures (iii)–(ix) are executed. (xi) When  $t$  becomes larger than  $t_{max}$ , another ion irradiates onto a different position, where we take  $t_{max}$  to be 100 fs, that is, when the secondary electrons lose sufficient energy that they can no longer change the electronic states of the molecules.

## 3. Results and discussions

Figure 1 shows  $P_e$  as a function of  $\tau$  for  $E_{ion} = 3, 5$ , and 10 MeV/u, where  $P_e$  is the probability of the number of secondary electrons passing through a region with radius  $r = 6$  nm. We have found that  $P_e$  is approximately saturated after the secondary electrons pass through a region of radius  $r \sim 5$  nm. We have found from our simulations that the equation

$$P_e \sim \sqrt{\tau/\tau_0}, \quad (1)$$

with  $\tau_0 = 1.5$  nm, is approximately satisfied, regardless of  $E_{ion}$ , for  $\tau \leq 1$  nm, where  $\tau$  is the mean path between incident ion impact ionization events [2, 3]. This agrees well with the result shown in our previous paper [2], where  $E_{ion} = 500$  keV/u. This results from the fact that the track potential is mainly determined by  $\tau$ . We have also found that  $P_e$  hardly depends on  $E_{ion}$ . This results from the fact that the track potential is mainly determined by  $\tau$ .

In order to determine the spatial distribution of energy deposition, we need to analyze the energy flow escaping the track potential. Figure 2 shows  $P_{fo}$  as a function of  $\tau$  for  $E_{ion} = 3$  MeV/u, where  $P_{fo}$  is the probability of energy flowing through a

region of radius  $r = 6$  nm. The energy flow decreases owing to the track potential and electron impact processes. Therefore, we execute three types of simulations, that is, ignoring the effects of electron-impact processes and the track potential, and considering both effects. When ignoring the effect of electron impact processes (see symbols  $\diamond$ ), we have found that a large part of the energy flow escapes the track potential. Although the energies trapped by the track potential have been thought to be small, almost all these energies are concentrated in the very narrow region  $r \leq 1$  nm. Because the volume of a region with radius  $r \leq 1$  nm is so small, the energy deposition per unit mass—that is, the radial dose, which is produced from those energies, near the ion path—becomes very large [4]. Because the dose is correlated with the amount of DNA damage, we expect that the yield of clustered DNA damage will increase with increasing dose.

Figure 2 also shows the value of  $P_{fo}$  obtained from the following equation:

$$P_{fo} = \frac{\int_{E_{ie,min}}^{E_{ie,max}} E_{ie} f(E_{ie}) dE_{ie}}{\int_0^{E_{ie,max}} E_{ie} f(E_{ie}) dE_{ie}}, \quad (2)$$

where  $E_{ie}$  is the energy of the initial secondary electrons,  $f(E_{ie})$  is the distribution function of  $E_{ie}$ , and  $E_{ie,min}$  and  $E_{ie,max}$  are the minimum and the maximum values of  $E_{ie}$  that enable secondary electrons to escape the track potential, respectively. We have found that Eq. (2) agrees with the trend of  $P_{fo}$  vs.  $\tau$  from our simulation results to within 7 %. We have also found that  $P_{fo}$  has almost the same values for  $E_{ion} = 3, 5$ , and 10 MeV/u, to within 5 %, although  $P_{fo}$  increases slightly with increasing  $E_{ion}$  (not shown here for  $E_{ion} = 5, 10$  MeV/u).

In ignoring the effect of the track potential (see symbols  $\circ$ ), we have found that  $P_{fo}$  retains an almost constant value ( $\sim 80$  %) as a function of  $\tau$ , because the electron impact processes are almost independent of  $\tau$ . These simulations correspond to the case of using the conventional model. The difference between  $P_{fo}$  with ignoring and considering the track potential (symbols  $\circ$  and  $\times$ ) corresponds to the effect of the track potential and almost agrees with  $P_{fo}$  ignoring the electron impact processes (symbols  $\diamond$ ).

Even when considering both effects (see symbols  $\times$ ), more than 60 % of the energy flow escapes from the region with  $r = 6$  nm. Owing to the electron-impact processes, we have found that  $P_{fo}$  is reduced by almost a constant value of 3–4 % for each 1-nm step in the direction perpendicular to the path of the incident ion. This means that, in the region  $r \leq 1$  nm, the decrease in  $P_{fo}$  due to the track potential dominates at small  $\tau$ , because, owing to the track potential,  $P_{fo}$  is reduced by much more than 4 %. The secondary electrons trapped by the track potential collide with molecules again and again during their long stay in the region  $r \leq 1$  nm, until they have lost sufficient energy that they can no longer change the electronic states of the molecules. This produces a high dosage [4]. On the contrary, because the secondary electrons escaping the track potential collide with molecules only a few times, the radial dose produced by these escaping electrons becomes relatively small near the incident ion path.

#### 4. Conclusions

Aiming to determine the spatial distribution of energy deposition created from heavy-ion irradiation, we have studied the probabilities of the number ( $P_e$ ) and energy flow ( $P_{fo}$ ) of secondary electrons that escape the track potential. We have found that  $P_e$  and  $P_{fo}$  are mainly determined by the mean path  $\tau$  between ion impact-ionization events and are almost

independent of the energies  $E_{ion}$  of the incident ions. Although  $P_{fo}$  is large even at small  $\tau$ , almost all the trapped secondary electrons are concentrated in the very narrow region  $r \leq 1$  nm.

#### Acknowledgments

We wish to thank Dr. K. Akamatsu and Dr. N. Shikazono (QST) for their useful discussions. We used the super computer “PRIMERGY BX900” of the Japan Atomic Energy Agency. This work has been supported by JSPS KAKENHI Grant Number 25390131 and 16H02959.

#### References

1. K. Kimura, *et al.*, Nucl. Instr. Meth. Phys. Res. B **193**, 661 (2002).
2. K. Moribayashi, *J. Phys. Soc. Jpn.*, **86**, 024301 (2017).
3. K. Moribayashi, *Radiat. Phys. Chem.*, **148**, 68 (2018).
4. K. Moribayashi, *Radiat. Phys. Chem.*, **96**, 211 (2014).

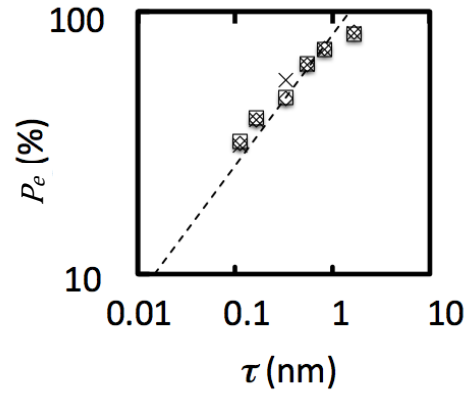


Fig. 1  $P_e$  (%) vs.  $\tau$  at  $E_{ion} = 3$  MeV/u ( $\square$ ), 5 MeV/u ( $\diamond$ ), and 10 MeV/u ( $\times$ ). The dashed line shows the results obtained from Eq. (1).

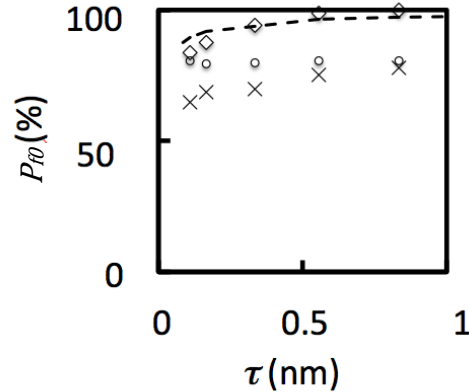


Fig. 2  $P_{fo}$  (%) vs.  $\tau$  at  $E_{ion} = 3$  MeV/u. Three types of simulations are executed, that is, ignoring the effect of the electron impact processes ( $\diamond$ ) and the effect of the track potential ( $\circ$ ), and considering both effects ( $\times$ ). The dashed line shows the results obtained from Eq. (2).

# Development of microspectroscopic imaging system for histopathology using mid-infrared laser

Makoto Aoyama<sup>1)</sup>, Takamitsu Morioka<sup>2)</sup>, Jin Xiaohai<sup>2)</sup>, Kanade Ogawa<sup>3)</sup>, Tatsuhiko Imaoka<sup>2,5)</sup>, Akinari Yokoya<sup>4,5)</sup>, Shizuko Kakinuma<sup>2)</sup> and Koichi Yamakawa<sup>1,5)</sup>

1) Medical Laser Applications Group, Department of Quantum Beam Life Sciences, 2) Department of Radiation Effects Research, 3) Light Touch Technology Inc., 4) Tokai Quantum Beam Science Center, 5) Group of Quantum and cellular Systems Biology, QST Advanced Study Laboratory

QST has developed various “quantum beams” for materials science, and some of these are beginning to be applied in life science. Spectroscopy has contributed greatly to the understanding of the physical sciences. It was able to provide information on the structure of the elements and the molecules that make up every subject of both the physical and biological sciences. Infrared (IR) spectroscopy has been widely applied to

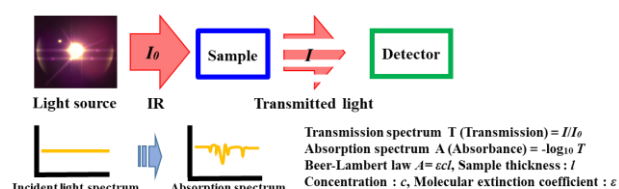


Fig.1. Basic principle of IR spectroscopy

detect the vibrational characteristics of chemical functional groups in diverse materials [1-2]. The basic principle of IR spectroscopy is shown in Fig.1. The superior contrast attained by functional group imaging and the selectivity found in the mid-IR region has been shown to be a powerful analytical tool (Fig.2 and

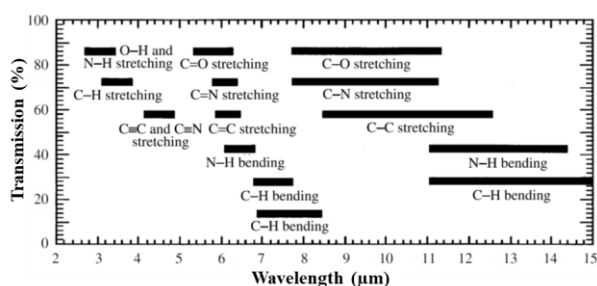


Fig.2. Correlations of various group molecular vibrations

RW. Waynant *et al.*, Philos. Trans. R. Soc. Lond. A, 359, 2001

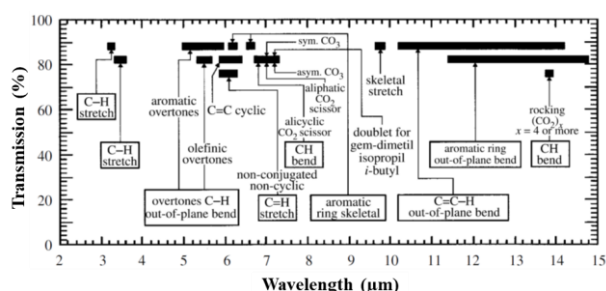


Fig.3. Characteristic IR absorption

RW. Waynant *et al.*, Philos. Trans. R. Soc. Lond. A, 359, 2001

3). Recently, the mid-IR has been a fruitful regime for medical research [3-4]. This is because many important biomolecules, such as proteins, lipids, and amides, exhibit strong characteristic vibrational transitions. Owing to the unique specificity of a biological molecule's spectrum in the mid-IR, lasers in this wavelength region have a unique advantage over ultraviolet (UV) and visible or near-IR lasers. In addition, mid-IR lasers have advantages of efficiency and adaptability for noninvasively investigating the chemical compositions of cells and tissues using a reagentless procedure and without the addition of dyes or labels for spectral determination. Hence, mid-IR lasers have great potential for medical applications, including tissue imaging.

Pathology is the study and diagnosis of diseases through the examination of organs, tissues and cells. Disease diagnosis by pathology generally involves gross and microscopic visual examination of tissues and cells with specialized stains employed to visualize specific proteins. Certain visualization techniques, such as special staining, immunohistochemistry, and electron microscopy have expanded the means by which pathologists can diagnose diseases. However, these techniques require complicated processes and time, and it is difficult to visually detect biochemical changes using them. Therefore, development of a simple analytical technique is desired. IR spectroscopy has a potential for application to visualization tools to aid pathologists in assessing tissue specimens.

In this study, we are investigating the discrimination of normal and malignant tissues of different organs using the mid-

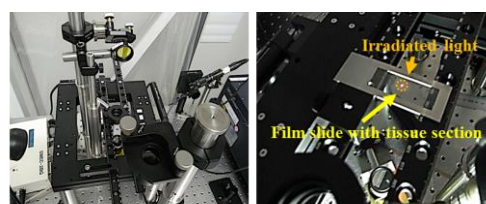
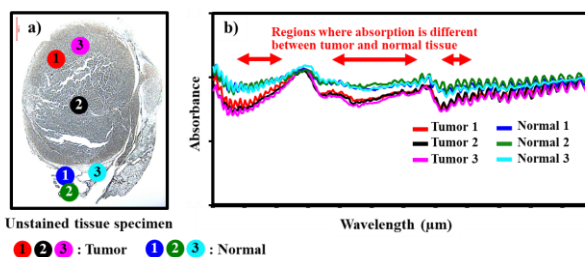


Fig.4. mid-IR microscopic system currently under development

IR laser. In our laboratory, a mid-IR microscopic system was constructed for the analysis of tissue specimens (Fig.4). Mouse lung tumor and normal lung tissue were analyzed by comparing them with the absorbance obtained from an unstained tissue specimen (Fig.5). Figure 5b illustrates the mid-IR spectra of the lung tumor and normal lung tissue from three different sites in tumor (Tumor 1-3) and normal (Normal 1-3) areas, and shows that the spectral patterns in the tumor differed from those in the normal tissue. The most changes in absorbance were observed in the three different regions. Next, this study conducted microscopic mapping of lung tumor tissue to obtain information



**Fig.5. The spectra from unstained tissue specimen by mid-IR laser**

Optical micrograph of the unstained lung tumor tissue specimen (a) and the corresponding absorbance mid-IR spectra of the unstained same tissue at three different sites in tumor and normal (b).

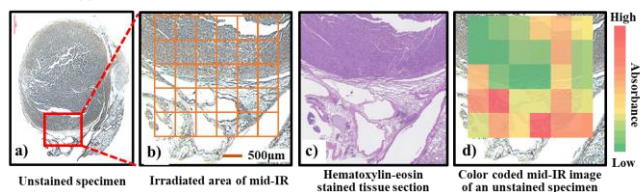


**Fig.6. Visible image using mid-IR microscopy and their corresponding map of lung tumor tissue.**

- Optical micrograph of the unstained lung tumor tissue specimen.
- Each square is irradiation area of mid-IR laser.
- Histopathological findings of irradiated area in lung tumor and normal tissue. Hematoxyline and eosin stain
- The mid-IR imaging of tumor and normal tissue.

on the absorbance of tumor cells. The lung tumor area for the mapping was determined by examining the mid-IR microscopic field (Fig.6b) compared with the corresponding histopathological view (Fig.6). Figure 6d displays the mid-IR absorbance map of lung tumor tissue. The color classification based on the mid-IR absorbance changes segmented the two main parts: lung tumor and normal lung tissue represented by the green and red ends, respectively. This study indicates that the mid-IR spectroscopic technique is useful for the diagnosis and discrimination of the differences between tumor and normal tissues based on the mid-IR absorption. Although there are several advantages of mid-IR spectroscopy, it is not yet known whether the spectral information from our device is able to satisfy the pathological diagnostic requirements and assist the pathologists' diagnoses. Thus, further investigations and improvements of our mid-IR spectroscopy are necessary to make these approaches applicable to routinely use in histopathological analysis. In addition, *in vivo* diagnostic tools using the mid-IR laser are highly required in many fields of medicine. These include endoscopy for guidance of surgical interventions to delineate lesion margins, or to replace random biopsies of suspicious tissues by targeted biopsies which would reduce unnecessary tissue excisions and biopsy-associated risks, or for a detection device in a much earlier stage of carcinogenesis. Future improvements in the mid-IR laser technology and data analysis will further extend the biomedical applicability and finally result in the implementation of these innovative techniques in the medical field.

## Acknowledgments

The authors thank Ms. M. Kaminishi, Y. Nishimura, and M. Shinagawa from the Department of Radiation Effects Research for the preparation of histological samples.

## References

- Meier RJ. 2005. *Chem Soc Rev* 34:743-52
- Grasselli JG, Mehicic M, Mooney JR. 1986. *Fresen Z Anal Chem* 324:537-43.
- Toor F, Jackson S, Shang XM, Arafin S, Yang HN. 2018. *Biomed Opt Express* 9:6255-7.
- Waynant RW, Ilev IK, Gannot I. 2001. *Philos T Roy Soc A* 359:635-44.



# Research Activities at the Synchrotron Radiation Research Center

Yoshinori Katayama (Director)

Synchrotron Radiation Research Center

At the SRRC (Synchrotron Radiation Research Center), we continue to develop a wide range of x-ray techniques for investigating the structural and electronic properties of matter using as major equipment the two QST beamlines at SPring-8, a large synchrotron radiation facility. Table 1 gives an overview of the objectives of the center. As well as precise measurements of high-quality crystalline samples, we have been concentrating on developing techniques which are applicable to inhomogeneous materials, which play important roles in determining the functions of many practical materials. We conduct leading research projects which demonstrate the ability of these techniques, and aim at gaining fundamental understanding of functional materials such as semiconductors, superconductors, magnetic materials, dielectric materials, hydrogen storage materials and catalysts. The equipment which we develop is open for public use, and in 2018 we accepted 38 research proposals as a member institute of the Nanotechnology Platform Japan [1].

The center consists of three experimental groups, one theory group, and a beamline operation office (Table 2). The research activities of each research group are summarized below.

Highly-brilliant synchrotron/FEL X-ray/VUV facilities are being constructed throughout the world at quite a pace. In the **Coherent X-ray Research Group**, to stay at the forefront of synchrotron/FEL science, we continue to develop advanced measurement/analysis techniques for the effective use of these new advanced light sources.

The use of spatially coherent X-rays from highly-brilliant synchrotron/FEL light sources has made it possible to visualize the inhomogeneity inside matter. We are now constructing an apparatus for coherent X-ray diffraction and applying it to the study of inhomogeneous functional materials such as ferroelectrics and relaxor ferroelectrics.

With the goal of exploiting the temporal coherence and intensity offered by next-generation light sources at short wavelengths, we are aiming at developing new nonlinear and quantum optical techniques using simple atomic systems. This year we used SACLA's soft X-ray beamline to observe the phenomenon of 'superfluorescence' at extreme ultraviolet wavelengths for the first time [2]. The coherent laser-like pulses

can be potentially controlled with a trigger laser, and could be the key to new pump-probe techniques using multi-colour short wavelength pulses.

Using a surface X-ray diffractometer coupled with a molecular beam epitaxy chamber, we have carried out in situ measurements of crystal truncation rod (CTR) scattering to investigate the atomic structure of gallium nitride surfaces under growth conditions. From CTR profile analysis, we could experimentally confirm the existence of a pseudo 1x1 structure, and also determine the structure parameters (interlayer distance, coverage, temperature factor).

The research objectives of the **High Pressure Science and Stress Research Group** are (i) the development of experimental techniques for in-situ measurements under extreme conditions, including high pressure, compressed hydrogen gas environments, and elasto-plastic stress fields, and (ii) fundamental and applied studies of advanced functional materials, such as highly hydrogen-containing materials, using these techniques. Group members focus on the study of the local structures of functional materials, and the high-pressure synthesis of novel hydrogen-rich compounds.

For studying functional materials, local structural studies are carried out using rapid-acquisition atomic pair-distribution function (RA-PDF) measurements. This method is applied to investigate various functional materials, for example, hydrogen absorbing alloys and negative thermal expansion materials. By collaborating with the National Institute for Materials Science, the method was used for the structure determination of magadiite. Magadiite is a natural layered silicate used as an additive in the TiO<sub>2</sub> photocatalytic system for oxidizing toluene to synthesize benzoic acid efficiently. However, the mechanism of this photocatalytic system was previously unclear due to the lack of structural information for magadiite, which has a low crystallinity. We succeeded in determining the detailed crystal structure of magadiite using the PDF measurement system, and clarified the photocatalytic mechanism [3].

In parallel, research into the high-pressure synthesis and crystal structure determination of novel aluminum-based hydrogen-containing compounds proceeded, and some novel compounds were synthesized. To further studies on hydrogen-containing materials, two group members joined the JSPS KAKENHI Grant-in-Aid for Scientific Research on Innovative Areas "Hydrogenomics" project, which started in FY2018, as co-investigators.

In many functional materials and devices, ranging from high-*T<sub>c</sub>* superconducting oxides to spintronics devices, the spin degrees of freedom of electrons play important roles. In the **Magnetism Research Group**, in order to unveil the functionality of such materials and devices, advanced x-ray spectroscopic techniques, such as nuclear resonant scattering (NRS), resonant inelastic scattering (RIXS), magnetic Compton scattering, and x-ray magnetic circularly polarized emission (XMCPPE), are developed. For NRS, a nuclear Bragg monochromator in operation since 2009 has enabled us to measure frequency-domain Mössbauer spectra using synchrotron radiation. The

Table 1. Objectives of SRRC

Development of advanced synchrotron radiation techniques	Quantum condensed matter physics
Integrated use of synchrotron radiation and other quantum beams	Inhomogeneous materials
Shared use (Nanotechnology platform)	Fundamental understanding of functional materials



recent development of a nuclear Bragg monochromator with controllable band-width and its application are presented elsewhere in this annual report [4]. For RIXS, energy resolution better than 50 meV has been achieved and applied to observe low-energy spin excitation, as well as charge and orbital excitations, in strongly correlated transition-metal compounds. The RIXS technique was also used for operando measurements of electronic states of functional materials for batteries. XMCPE is a brand-new magnetic spectroscopy in the hard x-ray regime, which has the distinctive feature of a large flipping ratio ( $\sim 10\%$ ) for Fe  $K\alpha$  emission. A scanning magnetic microscope using XMCPE has been developed in 2018. Machine learning and its applications to magnetic circular dichroism measurements were also studied.

The **Condensed Matter Theory Group** develops advanced simulation methods based on quantum mechanics, for investigating theoretically condensed matter by using supercomputers such as K-computer, and performing numerical simulations aiming at understanding various properties of materials such as magnetism, high- $T_c$  superconductivity, and catalytic activity, in collaboration with experiments using X-rays from, for example, SPring-8. Current activities include (i), the development of advanced simulation techniques for chemical reactions based on first principles molecular dynamics and their application to the research of the mechanisms of phenomena such as catalytic reactions, (ii), the clarification of the electronic properties and the excitation spectra of transition metal oxides by using numerical techniques such as exact diagonalizations on small cluster systems, with a particular focus on the theoretical prediction of the spectral features of resonant inelastic x-ray scattering (RIXS) on compounds such as high- $T_c$  cuprates and nickelates, (iii), the clarification of the electronic excitation processes in highly-correlated electron systems such as high- $T_c$  superconductors via theoretical analysis of RIXS by using precisely-calculated electronic structures, and (iv), theoretical investigations using large-scale numerical exact diagonalization of frustrated quantum spin systems such as the kagome-lattice antiferromagnet, the triangular-lattice antiferromagnet, and the

spin nanotube, which can exhibit quantum spin liquid properties related to high- $T_c$  superconductivity.








## Acknowledgments

The author thanks all members of SRRC for their contribution to this article.

## References

1. <http://www.kansai.qst.go.jp/nano/>
2. J. R. Harries, *et al.*, Phys Rev. Lett. **121**, 263201 (2018).
3. Y. Ide, *et al.*, Chem. Sci. **9**, 8637 (2018).
4. T. Mitsui, *et al.*, J. Phys. Soc. Jpn. **87**, 093001 (2018).

Table 2. Groups at the Synchrotron Radiation Research Center

Group	Coherent X-ray Research Group	High Pressure Science and Stress Research Group	Magnetism Research Group	Condensed Matter Theory Group
<b>Members</b>	(T. Watanuki (GL)), M. Takahashi, K. Ohwada, J. Harries, T. Sasaki	T. Watanuki (GL), A. Machida, H. Saitoh, A. Shiro, (R. Yasuda)	T. Inami (GL), T. Mitsui, A. Agui, K. Ishii, T. Ueno	(T. Sakai (GL)), T. Ikeda, K. Tsutsui, T. Nomura
<b>Typical Techniques &amp; apparatuses</b>	Surface X-ray diffraction  Coherent X-ray scattering  Quantum optics in EUV region	High-pressure and high-temperature X-ray diffraction  Pair distribution function analysis 	Mössbauer spectroscopy  Resonant inelastic X-ray scattering  X-ray magnetic circularly polarized emission	Numerical simulations 
<b>Research objective</b>	nitride semiconductors, ferroelectrics	Hydrogen containing materials, negative thermal expansion materials	Magnetism, Spintronics, High- $T_c$ superconductivity, catalysis	Magnetism, High- $T_c$ superconductivity, catalysis
Beamline Operation Office/ Y. Katayama, Y. Teraoka, Y. Tomisugi, K. Sugawara				

# Application of pair distribution function analysis to determine unsolved structure of layered silicate, magadiite

Akihiko Machida and Tetsu Watanuki

High Pressure Science and Stress Research Group, Synchrotron Radiation Research Center

## 1. Introduction

Structural information of a functional material provides important knowledge to understand its properties. Many functional materials are inherently inhomogeneous in their compositions or structures. X-ray diffraction (XRD) analysis is the most popular method to determine a crystal structure. We can obtain an average structure by analyzing the XRD profile. However, this method is insufficient for the analysis of inhomogeneous or heavily disordered structures. An atomic pair distribution function (PDF) stands for an interatomic atomic distribution within a material, and is a function in real space. By analyzing the PDF profile, we can obtain the probability of finding atom pairs at a distance  $r$ . Generally, this method is suitable to analyze the local- to middle-range structure, and is applied to the structural analysis of nanocrystalline and crystalline materials, as well as noncrystalline materials such as liquids and amorphous. Recently, it has been recognized as a powerful tool to investigate the structure of a crystalline material with inhomogeneity or significant disorder.

We developed the rapid-acquisition (RA)-PDF measurement<sup>1)</sup> system in BL22XU at SPring-8 and applied the PDF method to investigate various functional materials, such as hydrogen-absorbing alloys<sup>2-5)</sup> and negative thermal expansion materials<sup>6-8)</sup>. Magadiite is a natural layered silicate used for various applications, such as an adsorbent and catalyst<sup>9)</sup>. A group at the National Institute for Materials Science (NIMS) has found that benzoic acid is efficiently synthesized by using a  $\text{TiO}_2$  photocatalytic system oxidizing toluene, where magadiite is used as an additive<sup>10)</sup>. However, the mechanism of this photocatalytic system is unclear owing to the lack of the crystal structure of magadiite. It has been difficult to determine the crystal structure of magadiite because of its low crystallinity, that is, its crystal habit forms fine, lamellar crystallites, which tend to have stacking faults. Detailed PDF measurements using synchrotron radiation X-rays enable us to determine the structure of magadiite<sup>10)</sup>.

## 2. Rapid acquisition PDF system and its improvement

PDFs are obtained by a Fourier transformation of the total scattering data of specimens. BL22XU enables us to perform RA-PDF experiments using a large-area two-dimensional (2D) detector and high-energy X-rays up to 70 keV (wavelength of approximately 0.177 Å). By using an amorphous-Si flat panel detector (XRD1621, PerkinElmer), a 2D image is collected at short exposure time, in the sub-second range in the most rapid case. To analyze the collected 2D image and one-dimensional (1D) total scattering data, the PIXIA and MaterialsPDF program<sup>11)</sup> developed by Dr. Tominaka were installed. The PIXIA program is a pixel-based image analyzer for converting 2D image data into 1D total scattering data. The obtained 1D total scattering data exhibit good signal-to-noise ratio and high

counting statistics, even at higher scattering angles. By collaborating with Dr. Tominaka, the parameters of the PIXIA program were optimized for the BL22XU system. MaterialsPDF is a program for transforming the total scattering data into the PDF data. Thanks to these programs, the quality of the total scattering data is improved, and as a result the quality of the PDF data is also improved. Under the standard PDF measurement setup in BL22XU, the maximum  $Q$  range of the obtained total scattering pattern reaches  $Q_{\text{max}} = 25.5 \text{ \AA}^{-1}$ , indicating that the spatial resolution of PDF reaches  $\Delta r \sim 0.25 \text{ \AA}$ . The obtained total scattering pattern has good angular resolution, enabling the analysis of the long-range region in real space. In fact, the obtained PDF of a standard sample of  $\text{CeO}_2$  powder (NIST SRM674b) shows peaks even above 100 Å (see Fig. 1). The high spatial resolution and wide  $r$ -range region are advantages of BL22XU. Such features of the BL22XU system that can analyze the local- to-long range structure are suitable for the structural analysis of low-crystallinity materials, which have stacking disorders, such as magadiite.

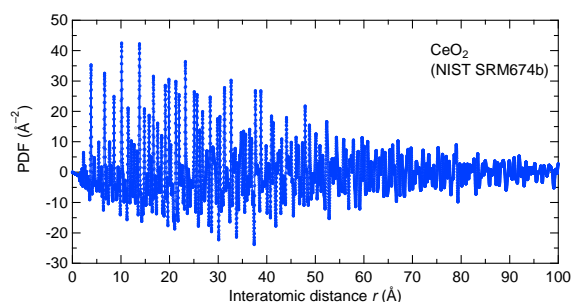


Figure 1. PDF data of standard sample of  $\text{CeO}_2$  powder loaded into polyimide capillary with inner diameter of 1 mm.

## 3. Structural determination of magadiite

Two types of magadiite were measured by collaborating with the NIMS group. One is the natural form containing Na ions, named “Na-magadiite,” and the other is its protonated form, “H-magadiite.” The PDF profiles analyze with the help of other analyses, such as composition analysis, XRD, and solid-state nuclear magnetic resonance (NMR). The local structure was analyzed by curve-fitting the PDF profile simulated using the PDFfit2 program<sup>12)</sup>. Figure 2 shows the results of the PDF analysis for Na- and H-magadiites. The obtained structural models are shown in Fig. 3. Structural analysis reveals the presence of microchannels consisting of an eight-membered ring of the  $\text{SiO}_4$  network in the thick silicate layers (see Fig. 3(c) and (d)). In Na-magadiite, Na ions coordinated by water molecules are filled in these microchannels. After removing the Na ions, the microchannels remain in H-magadiite. The structural information obtained by PDF analysis clarifies the mechanism of this photocatalytic reaction, which produces benzoic acid by oxidizing toluene. The

discovered microchannels of magadiites play an important role in this  $\text{TiO}_2$  photocatalytic system. Thus, our RA-PDF measurement system in BL22XU contributed to determining the unsolved structures of magadiites and to clarify the role of H-magadiite as an additive in the  $\text{TiO}_2$  photocatalytic system.

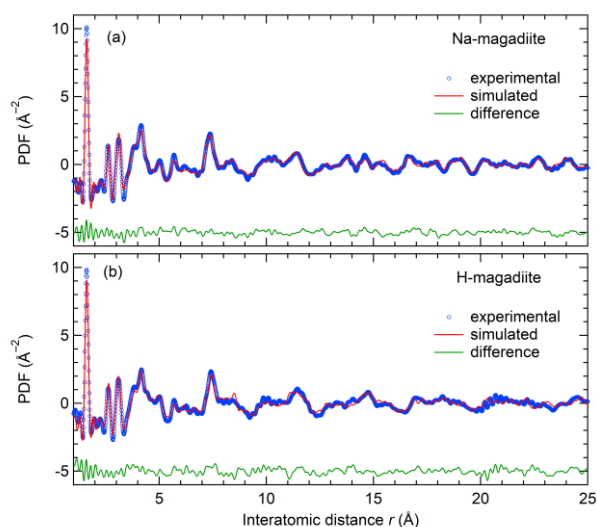


Figure 2. Results of PDF analysis of (a) Na-magadiite and (b) H-magadiite by curve fitting.

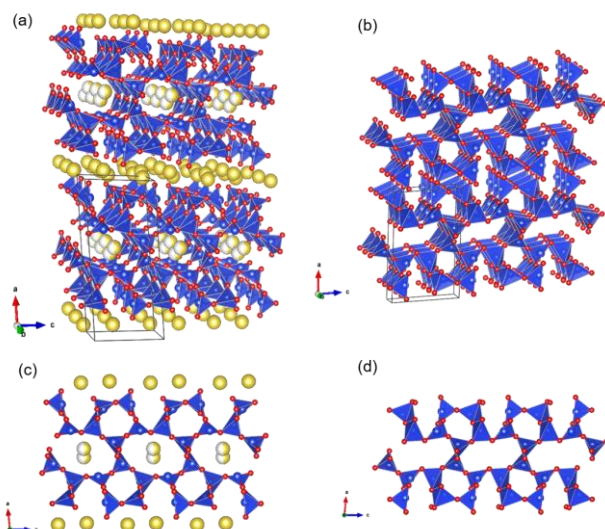


Figure 3. Structural models of (a) Na-magadiite and (b) H-magadiite obtained by the PDF analysis. The blue, red, and yellow spheres represent Si, O, and Na, respectively. (c) and (d) are parallel views along the  $b$ -axis. The structures were visualized using the VESTA program<sup>13)</sup>.

## Acknowledgments

This work was partially supported by the Photon and Quantum Basic Research Coordinated Development Program from the Ministry of Education, Culture, Sports, Science and Technology of Japan. This study was performed in collaboration with Dr. Tominaka of NIMS.

## References

1. P. J. Chupas, X. Qiu, J. C. Hanson, P. L. Lee, C. P. Grey, and

- S. J. L. Billinge, *J. Appl. Crystallogr.* **36**, 1342 (2003).
2. H. Kim, K. Sakaki, H. Ogawa, Y. Nakamura, J. Nakamura, E. Akiba, A. Machida, T. Watanuki, and T. Proffen, *J. Phys. Chem. C*, **117**, 26543 (2013).
3. K. Sakaki, N. Terashita, H. Kim, E. H. Majzoub, A. Machida, T. Watanuki, S. Tsunokake, Y. Nakamura, and E. Akiba, *J. Phys. Chem. C*, **118**, 6697 (2014).
4. K. Sakaki, H. Kim, A. Machida, T. Watanuki, Y. Katayama, and Y. Nakamura, *J. Appl. Crystallogr.* **51**, 796 (2018).
5. K. Asano, H. Kim, K. Sakaki, K. Jimura, S. Hayashi, Y. Nakamura, K. Ikeda, T. Otomo, A. Machida, and T. Watanuki, *Inorg. Chem.*, **57**, 11831 (2018).
6. R. Yu, H. Hojo, T. Watanuki, M. Mizumaki, T. Mizokawa, K. Oka, H. J. Kim, A. Machida, K. Sakaki, Y. Nakamura, A. Agui, D. Mori, Y. Inaguma, M. Schlipf, K.Z. Rushchanskii, M. Ležaić, M. Matsuda, J. Ma, S. Calder, M. Isobe, Y. Ikuhara and M. Azuma: *J. Am. Chem. Soc.*, **137**, 12719 (2015).
7. K. Nakano, K. Oka, T. Watanuki, M. Mizumaki, A. Machida, A. Agui, H.J. Kim, J. Komiyama, T. Mizokawa, T. Nishikubo, Y. Hattori, S. Ueda, Y. Sakai, and M. Azuma, *Chem. Mater.*, **28**, 6062 (2016).
8. T. Nishikubo, Y. Sakai, K. Oka, M. Mizumaki, T. Watanuki, A. Machida, N. Maejima, S. Ueda, T. Mizokawa, and M. Azuma, *Appl. Phys. Express*, **11**, 061102 (2018).
9. Y. Ide, N. Ochi, and M. Ogawa, *Angew. Chem. Int. Ed.*, **50**, 654 (2011).
10. Y. Ide, S. Tominaka, H. Kono, R. Ram, A. Machida, and N. Tsunoji, *Chem. Sci.*, **9**, 8637 (2018).
11. S. Tominaka, H. Yamada, S. Hiroi, S. I. Kawaguchi, and K. Ohara, *ACS Omega*, **3**, 8874 (2018).
12. C. L. Farrow, P. Juhas, J. W. Liu, D. Bryndin, E. S. Bozin, J. Bloch, T. Proffen, and S. J. L. Billinge, *J. Phys.: Condens. Matter*, **19**, 335219 (2007).
13. K. Momma and F. Izumi, *J. Appl. Crystallogr.*, **44**, 1272 (2011).

# First observation of superfluorescence at extreme ultra-violet wavelengths (164 nm and 30.4 nm)

James R. Harries

Coherent X-ray Research Group, Synchrotron Radiation Research Centre

The phenomenon of ‘superradiance’ was first introduced by Dicke in 1954 [1] as ‘coherence in spontaneous radiation processes’, arising from quantum correlations between excited atoms which interact through an electromagnetic field of wavelength  $\lambda$ , all located within a spatial region of dimension  $\lambda$ . The interaction leads to an enhancement (superradiance) or suppression (subradiance) of emission. Pure superradiance as initially described is difficult to realise in practice, but it was later found that spontaneous emission can induce a related process in initially uncorrelated atoms, even in an extended medium (where interatomic spacing remains comparable to  $\lambda$ , but the excited atoms extend over a region in space much larger). This process was termed ‘superfluorescence’ [2], although the distinction between superradiance and superfluorescence is often no longer made. Superfluorescence was first observed on rotational transitions in the HF molecule at microwave wavelengths [3], and subsequently at visible wavelengths following the widespread availability of lasers (see for example reference [4] for an overview). Phenomena related to superradiance have potential applications such as guide stars [5], and recently the initial stages of superradiance have been observed at X-ray wavelengths [6], and in diamond colour centres [7].

In a striking difference to spontaneous emission, the peak intensity of superradiant emission scales as  $N^2$ , where  $N$  is the number of interacting atoms. Since the total number of emitted photons is the same, the temporal width of the emission scales as  $1/N$ . In experimental realisations,  $N$  can be of the order of  $10^{10}$ , leading to very short, intense pulsed emission. For superfluorescence, where the initial excitation is incoherent, there is a characteristic time delay for a macroscopic polarization to develop, which also scales as  $1/N$ . In contrast to amplified spontaneous emission, superradiant decay can completely deplete the upper level. A characteristic superfluorescence timescale can be defined as  $\tau = 8\pi/(3\lambda^2 A_{ki} N_a L)$ , where  $\lambda$  and  $A_{ki}$  are the wavelength and the Einstein A coefficient of the transition,  $N_a$  the number density of excited atoms, and  $L$  the length of the medium. For superfluorescence to occur on a particular transition this time must be shorter than all other population or decoherence decay mechanisms. Further, the atoms must be excited on a timescale shorter than the delay time in order to observe pure superfluorescence. The observation of superradiant processes at short wavelengths thus presents challenges, since shorter wavelengths in general require higher number densities. Further, suitable atomic transitions are difficult to find, since, for example, inner shell transitions must compete with fast processes such as Auger decay. The lack of suitable materials for windows and optical elements at short wavelength introduces further technical constraints.

We have recently overcome these challenges to observe superfluorescence at vacuum ultraviolet (164 nm) and extreme ultraviolet (30.4 nm) wavelengths for the first time. A suitable atomic level scheme is found in helium ions, a high density of which can be rapidly created by ionisation with free-electron laser pulses at photon energies greater than the neutral helium ionisation potential of  $\sim 25$  eV. Since windows cannot be used to

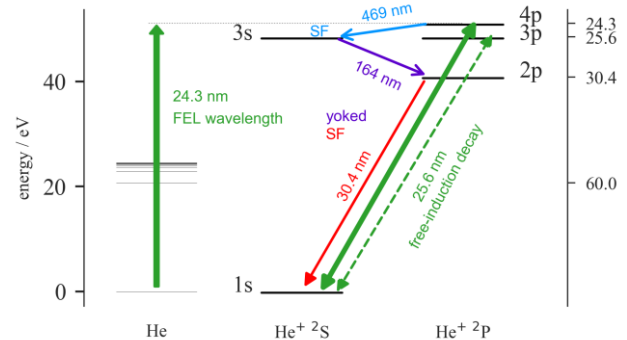


Figure 1: Partial level scheme. Helium atoms are ionised and then excited by the same FEL pulse, which is resonant with the 1s-4p transition in  $\text{He}^+$ . Due to the high density of excited 4p ions, superfluorescence occurs on the route 4p-3s-2p-1s, with the 2<sup>nd</sup> and 3<sup>rd</sup> steps ‘yoked’ due to the initial coherence of the 1s-4p excitation.

provide a high gas density isolated from the laser beamline, we use a pulsed valve to inject neutral helium into a small differentially-pumped gas cell with 1 mm apertures through which the FEL beam passes. Neutral helium densities of up to  $10^{23} \text{ m}^{-3}$  (pressure  $\sim 0.01$  atm) can be reached. At a central wavelength of 24.3 nm, essentially all of the neutral helium atoms along the FEL beam’s path through the gas cell are ionised. Since 24.3 nm is resonant with excitation of the 4p electronic state of the ion (see figure 1), a large density of excited ions is created within the  $< 100$  fs pulse. This results in superfluorescent decay on the 4p-3s transition at a wavelength of 469 nm.

Experimentally this was observed as highly-directional blue flashes of light (see figure 2). Using a fast photodiode, it was confirmed that the pulses had temporal widths of the order of picoseconds, and picosecond delays with respect to the incident FEL pulse. Both the temporal width and the delay were found to scale as  $1/P$ , with  $P$  the backing pressure behind the pulsed nozzle, which is expected to be proportional to instantaneous number density. These experimental results unequivocally confirm the observation of superfluorescence on this transition. With sufficiently strong superfluorescent emission, significant population can be transferred to the 3s state (see figure 1), which can undergo further superfluorescence decay (wavelength 164 nm) to the 2p state. Observations with a grazing-incidence spectrometer (figure 2) confirmed highly-directional emission at this wavelength. Since superfluorescence requires a population inversion to proceed, further superfluorescence on the 2p-1s transition (see figure 1) at 30.4 nm would not be expected, however we also observed highly-directional emission at this wavelength (figure 2). Superradiant emission is only possible on this transition as *yoked* superfluorescence [9], which can occur if the initial excitation imparts sufficient coherence to the atomic system. In this case, an initial coherence between 1s and 4p can be transferred by the 4p-3s and 3s-2p transitions, resulting in a coherence between the 1s and 2p states. The 3s-2p and 2p-1s



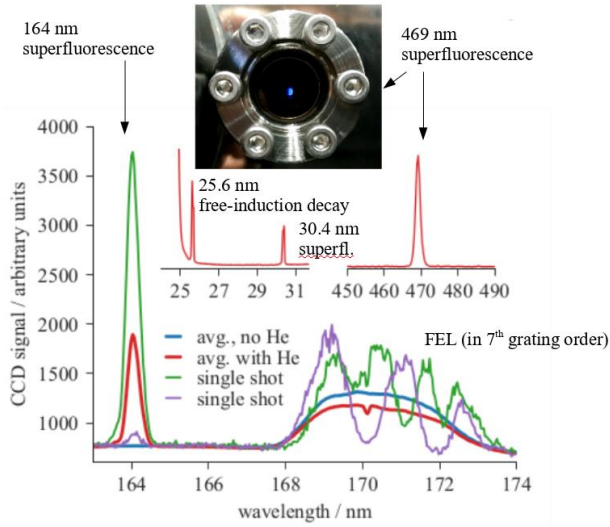


Figure 2. Overview of experimental results. Strong, highly-directional emission was observed at wavelengths of 469 nm, 164 nm, 30.4 nm, and 25.6 nm.

transitions are thus *yoked*, since they cannot occur independently. In this case the transition parameters are such that superfluorescence can occur from the  $3s$  state to the  $1s$  state ‘through’ the  $2p$  state, with emission at 164 nm and 30.4 nm appearing simultaneously. While we were unable to confirm this interpretation experimentally due to the lack of detectors with both sufficient sensitivity and sufficient time resolution in the required wavelength regions, the high intensity and high directionality of the observed emissions strongly support our conclusions.

Further evidence is provided from semi-classical numerical simulations of the propagation of free-electron laser pulses through a dense target of helium ions (figure 3). We used the Maxwell-Liouville equations [10], with 16 atomic levels and time and spatial step-sizes of 6.5 as and 3.0 nm to model the propagation of 70-fs-long pulses through 50  $\mu\text{m}$  of helium ions. These simulations are computationally intensive, and were performed in parallel on multiple single nodes of JAEA’s supercomputer. The partial coherence of the SACLA FEL pulses was modelled using a random phase approximation [11]. Results for a single pulse are shown in figure 3, where the rolling Fourier transform of the electric field at the output of the medium is plotted as a function of time. The spectrally broad FEL pulse is seen vertically at  $t = 167$  fs (50  $\mu\text{m}/c$ ), and free-induction decay (and Burnham-Chiao ringing [12]) is seen as a spectrally narrow

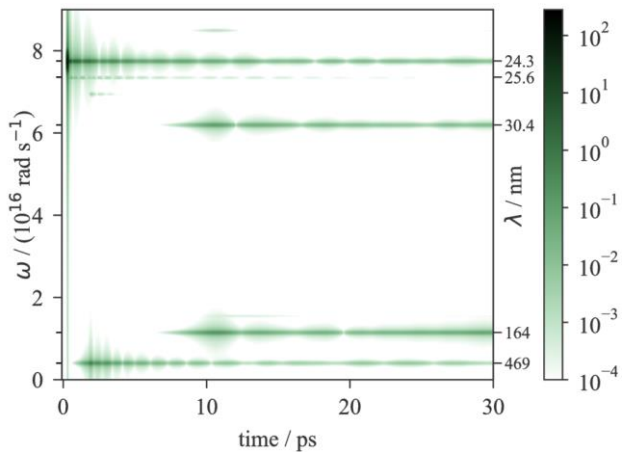


Figure 3. Simulation results. Rolling Fourier transform (20 fs window) of the electric field at the output of the medium.

tail at the  $1s$ - $4p$  resonant frequency. Similar emission is also seen at a wavelength of 25.6 nm, on the  $1s$ - $3p$  transition. Following a short delay ( $\sim 3$  ps), emission is seen at a wavelength of 469 nm, which can be interpreted as superfluorescence on the  $4p$ - $3s$  transition. Following a further delay (at  $t \sim 10$  ps), emission is seen simultaneously at wavelengths of 164 nm ( $3s$ - $2p$ ) and 30.4 nm ( $2p$ - $1s$ ). This is consistent with our interpretation of the experimental results as indicating yoked superfluorescence on these transitions. A similar plot for the electric field emitted in the backwards direction (shown in [8]) reveals that the 30.4 nm emission only appears in the forward direction. This is again consistent with yoked superfluorescence, which requires phase matching. Weaker signal can also be seen at wavelengths corresponding to four-wave mixing between the various wavelengths present in the medium, although these were not observed experimentally.

The observation of yoked superfluorescence is of particular interest since it only arises due to the coherence of the exciting pulse, which for SACLA BL1 is only partial. Simulations with different random phase seeding show that the process is sensitive to the degree of coherence, and a more detailed numerical study is underway. From the point of view of applying coherent processes at short wavelengths, this is an important result. Whereas seeding technology can be used to generate coherent FEL pulses at the wavelengths used here (FERMI [13]), shorter wavelength FELs still rely on the SASE process.

Superfluorescence provides a route to laser-like, coherent pulses of light with timing characteristics that can be controlled by varying number density, and also by a ‘trigger’ laser. For the scheme used here, a femtosecond laser pulse at a wavelength of 469 nm (timed to pass through the target following the FEL, but before superfluorescence develops spontaneously) could be used to trigger the emissions at 164 nm and 30.4 nm, suggesting application as a jitter-free pump-probe scheme.

The extension to even shorter wavelengths presents the challenge of finding suitable level schemes and generating even higher target densities. One approach we are pursuing is to use nanoparticles such as clusters or superfluid liquid helium droplets, which offer number densities similar to the solid phase. Further, molecules or clusters attached to large liquid helium droplets could provide suitable level schemes, and by varying the size of the droplets the inter-molecular spacing (and hence characteristic superfluorescence time) can be controlled.

## Acknowledgments

This work was a collaboration with H Iwayama and E Shigemasa (Institute of Molecular Science), S Kuma and I Inoue (RIKEN), M Iizawa, N Suzuki and Y Azuma (Sophia University), and S Owada and T Togashi (JASRI), with the support of K Tono (JASRI) and M Yabashi (RIKEN). The experiments were carried out at SACLA BL1, and the simulations using JAEA’s SGI ICE supercomputer. We are grateful to the SACLA staff and SPring-8 Services for technical support.

## References

1. R H Dicke *Phys. Rev.* **93**(1) 99 (1954)
2. Bonifacio and Lugiato *Phys. Rev. A* **11**(5) 1507 (1975)
3. Skribanowitz et al. *Phys. Rev. Lett.* **30**(8) 309 (1973)
4. *Superradiance: Multiatomic Coherent Emission*, edited by M G Benedict (CRC Press, Bristol, Philadelphia, 1996)
5. J V Thompson et al. *New J. Phys.* **16**(10) 103017 (2014)
6. A I Chumakov et al. *Nat. Phys.* **14**(3) 261 (2018)
7. A Angerer et al., *Nat. Phys.* **14**(12) 1168 (2018)
8. J R Harries et al. *Phys. Rev. Lett.* **121**, 263201 (2018).
9. J H Brownell et al. *Phys. Rev. Lett.* **75**, 3265 (1995)
10. R Marskar and U Österberg, *Opt. Express* **19**, 16784 (2011)
11. T Pfeifer et al., *Opt. Lett.* **35**, 3441 (2010)
12. D C Burnham and R Y Chiao, *Phys. Rev.* **188**, 667 (1969)
13. E Allaria et al. *New J. Phys.* **12**, 075002 (2010)

# Effect of B-site randomness on the antiferroelectric/relaxor nature of the ground state

Kenji Ohwada

Coherent X-ray Research Group, Synchrotron Radiation Research Center

Relaxor ferroelectrics exhibit many unique and useful properties, such as large dielectric and piezoelectric coefficients with a broad range of temperature and frequency dependencies. They have attracted intense scientific and industrial interest over the past few decades, because they often show complex multiscale structures and puzzling mechanisms. They also show strong potential for industrial applications such as transducers, based upon their good piezoelectric properties. Despite intensive research, arguments about the intrinsic mechanism underlying the unique properties of lead-based relaxors are still unsettled. One of the main reasons for this is that it is necessary to deal with the nanometer- to micrometer-scale heterogeneity intrinsic to relaxors.

Typical relaxors have  $\text{PbB}^{\text{B}}\text{O}_3$  complex perovskite structures, where two different ions occupy the perovskite B site stoichiometrically to conserve the average charge of 4+, e.g.,  $\text{Pb}(\text{Mg}_{1/3}^{2+}\text{Nb}_{2/3}^{5+})\text{O}_3$  (PMN) and  $\text{Pb}(\text{In}_{1/2}^{3+}\text{Nb}_{1/2}^{5+})\text{O}_3$  (PIN). However, the arrangement strongly depends on the actual materials. The randomness at the B site is commonly accepted to be intrinsic to the appearance of the relaxor state.

PIN [1, 2] is one of the best materials for investigating the effect of the randomness at the B site (B-site randomness) on the relaxor nature. Annealing PIN crystals causes the In and Nb atoms to order along the  $\langle 111 \rangle$  direction, whereas quenching leads to disorder. PIN with a large In-Nb ordered region (ordered-PIN: O-PIN) transforms into an antiferroelectric (AFE) state, whereas PIN with a large In-Nb disordered region (disordered-PIN: D-PIN) becomes a relaxor. The dielectric constant  $\epsilon'(T)$  exhibits a small but sharp drop at the transition temperature  $T_N \sim 430$  K in O-PIN, and in contrast, a large and broad peak around  $T_{\text{max}}$  near room temperature ( $\sim 300$  K) in D-PIN, where  $T_{\text{max}}$  strongly depends on the frequency of the electric field.

It has been reported that the structure and dynamics of relaxors can be understood in terms of fractals, which can deal well with a broad distribution of length and time scales [3–5]. We are interested in the dynamic nature of the PIN materials depending upon the B-site randomness.

In this study, we have investigated the effect of B-site randomness on the AFE/relaxor nature of the ground state by studying diffuse and inelastic X-ray scattering (IXS) from O- and D-PIN single crystals [6]. The diffuse scattering measurement of O-PIN, which is AFE at low temperatures, shows that the ferroelectrically interactive local polarization exists in the cubic phase, above the transition temperature  $T_N$ . As shown in Fig. 1, IXS analysis of the diffuse scattering shows that the transverse acoustic (TA) and transverse optic (TO) modes are dominant at high temperatures ( $\sim 800$  K), whereas the central peak (CP) and TA modes, which are coupled, are major contributors to diffuse scattering near  $T_N$ , and show critical behavior at temperatures close to  $T_N$ . The TO mode shows no anomaly at temperatures close to  $T_N$ . Furthermore, the phonon spectra are broad, indicating that a strong damping mechanism exists even in the sample with weak chemical disordering, O-PIN. No clear difference between O- and D-PIN is observed at temperatures above  $\sim 500$  K. Here,

the major difference between them is the property of the CP mode, which shows no drop, and increases rapidly with decreasing temperatures in D-PIN. The CP mode is thought to be directly related to the local polarization, and considered to originate in a combination of Pb-flipping and the TO mode. The B-site is considered to control the AFE/FE instability of lead-based perovskite materials. Finally, the B-site randomness is discussed in terms of suppressing the AFE instability, and enhancing the polarization fluctuation [2].

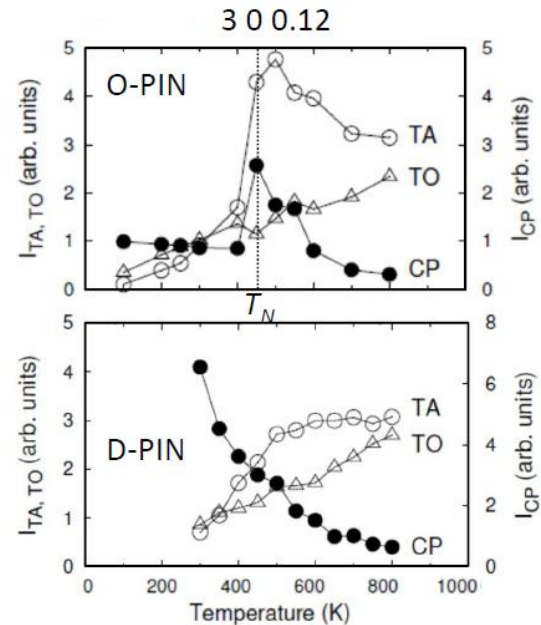


Figure 1: Obtained CP, TA, and TO components in the diffuse scattering from O-PIN and D-PIN as functions of temperature.

## Acknowledgments

We would like to thank Drs. S. Tsukada (Shimane University), T. Fukuda (JAEA), S. Tsutsui (JASRI), A. Q. R. Baron (RIKEN), J. Mizuki (Kwansei Gakuin University), H. Ohwa, N. Yasuda (Gifu University), and H. Terauchi (Kwansei Gakuin University) for their collaboration.

## References

1. A. A. Bokov, I. P. Raevskii, and V. G. Smotrakov, *Sov. Phys. Solid State* **26**, 1708 (1984).
2. K. Ohwada and Y. Tomita, *J. Phys. Soc. Jpn.* **79**, 011012 (2010).
3. S. Vakhrushev, A. Nabereznov, S. K. Sinha, Y. P. Feng, T. Egami, *J. Phys. Chem. Solids* **57**, 1517–1523 (1996).
4. A. Koreeda, H. Taniguchi, S. Saikan, M. Itoh, *Phys. Rev. Lett.* **109**, 197601 (2012).



5. S. Tsukada, K. Ohwada, H. Ohwa, S. Mori, S. Kojima, N. Yasuda, H. Terauchi, and Y. Akishige, *Sci. Rep.* **7**, 17508 (2017).
6. K. Ohwada, S. Tsukada, T. Fukuda, S. Tsutsui, A. Q. R. Baron, J. Mizuki, H. Ohwa, N. Yasuda, H. Terauchi, *Phys. Rev. B* **98**, 054106 (2018).

# Variable-bandwidth $^{57}\text{Fe}$ Synchrotron Mössbauer Source

Takaya Mitsui

Magnetism Research Group, Synchrotron Radiation Research Center

A synchrotron Mössbauer source (SMS) is a powerful tool for the local analysis of iron-based materials. The SMS filters the single-line  $^{57}\text{Fe}$ -Mössbauer radiation from synchrotron radiation (SR) using pure nuclear Bragg reflection (PNBR) of the  $^{57}\text{FeBO}_3$  crystal near the Néel point ( $T_N$ ), and it allows us to conduct conventional  $^{57}\text{Fe}$  Mössbauer spectroscopy, whereby information on the local magnetic state, valence, and electron density can be obtained via the electron nuclear hyperfine couplings. Additionally, the high degree of polarization, low divergence, and small beam size of SR enables an advanced Mössbauer experiment [1]. Moreover, SMS has great potential to improve the radiation properties because the magnetic control of  $^{57}\text{FeBO}_3$  crystal significantly affects the PNBR. As a first attempt, we have developed a new method of varying the bandwidth of SMS by controlling the magneto-acoustic vibrations in a  $^{57}\text{FeBO}_3$  crystal [2]. The scheme is as follows. Below the  $T_N$ , nuclear Zeeman splitting is observed in  $^{57}\text{FeBO}_3$ . In this case, the PNBR has a multiline resonance structure, corresponding to the four absorption lines of  $\Delta m = \pm 1$  nuclear transitions. At room temperature, the resonance energies spread in the region of  $\sim 10^{-6}\text{eV}$ , and the photon flux is more than 10 times larger than that of single-line PNBR from the  $^{57}\text{FeBO}_3$  crystal near the  $T_N$ . However, multiline PNBR is not suitable as a probe in spectroscopy. To solve this problem, a radio frequency magnetic field ( $H_{\text{RF}}$ ) is applied to the temperature-controlled  $^{57}\text{FeBO}_3$  crystal to excite magneto-acoustic vibrations. In this case, the random vibrations of  $^{57}\text{Fe}$  atoms are excited in the crystal via magneto-elastic coupling [3], and single-line PNBR below the  $T_N$  is obtained by the collapse of nuclear Zeeman splitting in  $^{57}\text{FeBO}_3$ . The linewidth is controllable in the range of  $10^{-8}$  to  $10^{-6}\text{eV}$  by adjusting the  $H_{\text{RF}}$  and the crystal temperature. Figure 1(a) shows the optical system of variable bandwidth  $^{57}\text{Fe}$ -SMS. The  $\sigma$ -polarized X-rays were monochromatized to a bandwidth of 2.5 meV at the  $^{57}\text{Fe}$  nuclear resonance energy (14.4keV) by a high-resolution monochromator consisting of Si(511) and (975) crystals. It was incident on the RF vibrating  $^{57}\text{FeBO}_3$  (95% enriched in  $^{57}\text{Fe}$ ): the magneto-acoustic vibrations were excited by the  $H_{\text{RF}}$  of  $f = 8.0$  MHz and of variable amplitude (0–3.6 Oe); the  $H_{\text{RF}}$  was generated by a Helmholtz coil ( $\phi 20\text{mm}$ ); the crystal temperature was controlled in the range of 25–76 °C.  $^{57}\text{Fe}$  Mössbauer radiation was filtered from the SR by the  $^{57}\text{FeBO}_3$  (333) PNBR and the bandwidth (energy distribution) of the PNBR was evaluated by measuring the Mössbauer spectra of a Doppler-vibrating 90%  $^{57}\text{Fe}$ -enriched 2 $\mu\text{m}$ -thick stainless-steel (SS) foil.

The observed spectra are shown in Figure 1(b). At a glance, one can see that the results give clear evidence that single-line absorption profiles with different linewidths are obtained by adjusting the  $H_{\text{RF}}$  and the crystal temperature: the bandwidths of SMS show continuous variation in the range of  $10^{-8}$  to  $10^{-6}\text{eV}$ , depending on  $H_{\text{RF}}$  and  $T$ ; the photon flux markedly increases with linewidth-broadening. Table 1 summarizes the linewidth and beam flux of the RF collapsed  $^{57}\text{Fe}$ -SMS.

The variable-bandwidth  $^{57}\text{Fe}$ -SMS provides new application

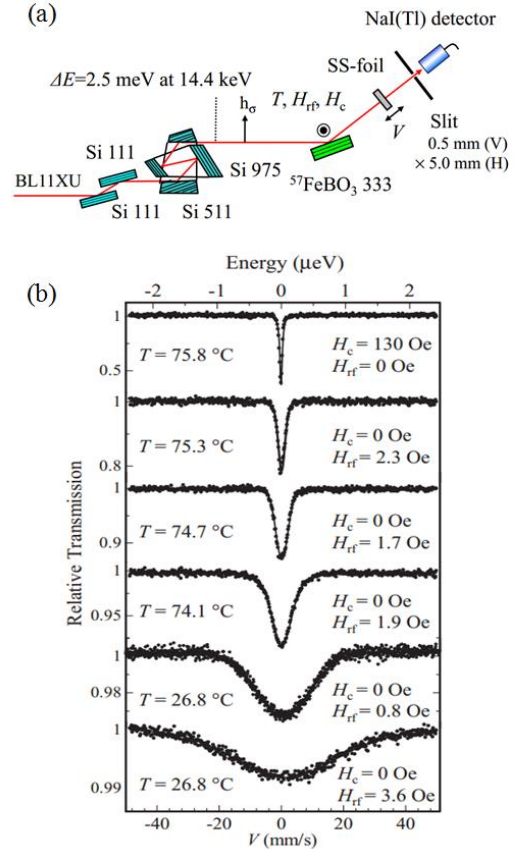


**Figure 1.** Variable-bandwidth  $^{57}\text{Fe}$ -SMS.

(a) Optical system. (b) Energy distribution of  $^{57}\text{Fe}$ -SMS under RF field at various temperatures.

possibilities of SR-Mössbauer experiments. As the first feasible application, quasielastic  $\gamma$ -ray scattering of liquid glycerol was measured. Figure 2(a) shows the experimental setup: the  $H_{\text{RF}}$  (0.75Oe, 8 MHz) was applied to the  $^{57}\text{FeBO}_3$  crystal at  $T = 25^\circ\text{C}$ . The glycerol was placed on the Cu-stage in a  $\text{LN}_2$ -cryostat; the  $^{57}\text{Fe}$ -SR-Mössbauer radiation, whose bandwidth was  $\sim 1\mu\text{eV}$ , was incident on the sample and a Mössbauer reference absorber (MRA), whose absorption linewidth was 50neV, was used to detect the linewidth broadening of the scattered radiation.

Initially, to obtain an instrumental function, the absorption

**Table 1.** Linewidth vs beam flux of the RF collapsed  $^{57}\text{Fe}$ -SMS.

$T$ (°C)	$H_c$ (Oe)	$H_{\text{RF}}$ (Oe)	Linewidth (neV)	Beam flux (cps)
75.8	130	0	15.1(1)	$1.8 \times 10^4$
75.3	0	2.3	97.4(3)	$5.0 \times 10^4$
74.7	0	1.7	187.9(4)	$1.1 \times 10^5$
74.1	0	1.9	344.9(6)	$1.2 \times 10^5$
26.8	0	0.8	$0.99(1) \times 10^3$	$1.6 \times 10^5$
26.8	0	3.6	$1.83(3) \times 10^3$	$1.6 \times 10^5$

spectrum of an MRA placed in the forward direction was measured with no sample. As shown in the upper part of Figure 2(b), the spectrum was a single-line profile and was well fitted by the Voigt function with a linewidth of  $\sim 1 \mu\text{eV}$ . Subsequently, the quasielastic  $\gamma$ -ray scattering of glycerol was observed at  $-123$  and  $25^\circ\text{C}$ . The former was below the glass-transition temperature  $T_g \sim 115^\circ\text{C}$  and the latter was over the melting point  $T_m \sim 17^\circ\text{C}$ . The quasielastic  $\gamma$ -ray photons scattered by the sample were transmitted through the MRA placed at the scattering angle of  $12^\circ$ . The results in Figure 3(b) show that the spectrum of glycerol at  $-123^\circ\text{C}$  is almost the same as that of the instrumental function, meaning that the line broadening of the quasielastic scattering of polycrystallized glycerol at a low temperature ( $T < T_g$ ) is too small to be measured with the resolution of this spectrometer. In contrast, the spectrum at  $T = 25^\circ\text{C}$  shows a marked linewidth broadening. Considering the linewidth of the instrumental function, the line broadening due to atomic vibration is estimated to be  $\sim 1 \mu\text{eV}$ .

3. T. Mitsui et al., Nucl. Instr. and Meth. B. **199** (2003) 75.

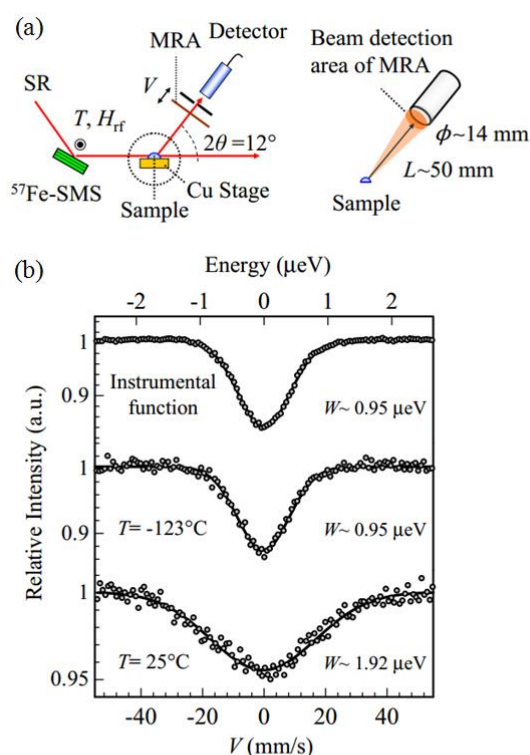


**Figure.2.** Quasielastic  $\gamma$ -ray scattering of liquid glycerol.

(a) Experimental setup. (b) Velocity spectra displaying quasielastic line broadening in scattering from glycerol.

This result shows that the variable-bandwidth  $^{57}\text{Fe}$ -SMS has a high potential to determine the energy transfer of soft condensed matter (e.g., proteins, colloids, or polymers). The bandwidth-controllable single-line  $^{57}\text{Fe}$ -SMS will open new possibilities of SR-based Mössbauer studies with an ultrahigh resolution of  $10^{-8}$  to  $10^{-6} \text{ eV}$ .

## Acknowledgments

This work was supported by the Grants-in-Aid for Scientific Research (B,25287086) from the Japan Society for the Promotion of Science (JSPS).

## References

1. T. Mitsui et al., J. Synchrotron Radiat. **16** (2009) 723.
2. T. Mitsui et al., J. Phys. Soc. Jpn. **87** (2018) 093001.



# Publication List

## [Original Papers]

1. “Spectral characterisation of aperiodic normal-incidence Sb/B<sub>4</sub>C multilayer mirrors for the  $\lambda < 124 \text{ \AA}$  range”  
E. A. Vishnyakov, I. A. Kopylets, V. V. Kondratenko, A. O. Kolesnikov, A. S. Pirozhkov, E. N. Ragozin, A. N. Shatokhin  
*Quantum Electronics* **48**(3), 189 - 196 (2018); DOI:10.1070/QEL16574
2. “Spectral weight of resonant inelastic X-ray scattering in doped cuprates: Effect of core-hole lifetime”  
T. Tohyama, K. Tsutsui  
*International Journal of Modern Physics B* **32**(17), 1840017 (2018); DOI:10.1142/S0217979218400179
3. “Heat treatment of transparent Yb:YAG and YAG ceramics and its influence on laser performance”  
K. Fujioka, T. Mochida, Y. Fujimoto, S. Tokita, J. Kawanaka, M. Maruyama, A. Sugiyama, N. Miyanaga  
*Optical Materials* **79**, 353 – 357 (2018); DOI:10.1016/j.optmat.2018.03.047
4. “In situ synchrotron X-ray diffraction study on epitaxial-growth dynamics of III–V semiconductors”  
M. Takahashi  
*Japanese Journal of Applied Physics* **57**, 050101 (2018); DOI:10.7567/JJAP.57.050101
5. “Reduction and oxidation annealing effects on Cu K-edge XAFS for electron-doped cuprate superconductors”  
S. Asano, K. M. Suzuki, D. Matsumura, K. Ishii, T. Ina, M. Fujita  
*Journal of Physics: Conference Series* **969**, 012051 (2018); DOI:10.1088/1742-6596/969/1/012051
6. “鉛系ペロブスカイト型酸化物で「電荷ガラス」を発見”  
綿貫 徹, 町田 晃彦, Hyunjeong Kim, Runze Yu, 東 正樹, 水牧 仁一朗  
*放射光*, **31**(3), 202 - 211 (2018)
7. “軟X線レーザーによるフェムト秒レーザーアブレーション過程の観察”  
長谷川 登, 錦野 将元  
*Journal of Plasma Fusion Research* **94**(5), 261 – 265 (2018)
8. “Gapless spin excitations in the S=1/2 Kagome- and triangular-lattice Heisenberg antiferromagnets”  
Toru Sakai, Hiroki Nakano  
*Physica B* **536**, 85 - 88 (2018); DOI:10.1016/j.physb.2017.08.058
9. “Numerical-Diagonalization Study of Magnetization Process of Frustrated Spin-1/2 Heisenberg Antiferromagnets in Two Dimensions: -Triangular- and Kagome-Lattice Antiferromagnets-“  
H. Nakano, T. Sakai  
*Journal of the Physical Society of Japan* **87**(6), 1063706 (2018); DOI:10.7566/JPSJ.87.063706
10. “Loss-of-function mutations in Zn-finger DNA-binding domain of HNF4A cause aberrant transcriptional regulation in liver cancer”  
H. Taniguchi, A. Fujimoto, H. Kono, M. Furuta, M. Fujita, H. Nakagawa  
*Oncotarget* **9**(40), 26144 - 26156, (2018); DOI:10.18632/oncotarget.25456
11. “Development of in situ synchrotron X-ray total scattering setup under pressurized hydrogen gas”  
K. Sakaki, H. Kim, A. Machida, T. Watanuki, Y. Katayama, Y. Nakamura  
*Journal of Applied Crystallography* **51**(3), 796 - 801, (2018); DOI:10.1107/S1600576718005101
12. “Commensurate versus incommensurate charge ordering near the superconducting dome in Ir<sub>1-x</sub>PtxTe<sub>2</sub> revealed by resonant x-ray scattering”  
K. Takubo, K. Yamamoto, Y. Hirata, H. Wadati, T. Mizokawa, R. Sutarto, F. He, K. Ishii, Y. Yamasaki, H. Nakao, Y. Murakami, G. Matsuo, H. Ishii, M. Kobayashi, K. Kudo, M. Nohara  
*Physical Review B* **97**(20), 205142 (2018); DOI:10.1103/PhysRevB.97.205142



13. “Development of density measurement for metals at high pressures and high temperatures using X-ray absorption imaging combined with externally heated diamond anvil cell”  
Y. Takubo, H. Terasaki, T. Kondo, S. Mitai, S. Kamada, T. Kikegawa, A. Machida  
*Comptes Rendus Geoscience*, (2018); DOI:10.1016/j.crte.2018.04.002
14. “The Heidelberg compact electron beam ion traps”  
P. Micke, S. Kühn, L. Buchauer, J. R. Harries, T. M. Bücking, K. Blaum, A. Cieluch, A. Egl, D. Hollain, S. Kraemer, T. Pfeifer, P. O. Schmidt, R. X. Schüssler, Ch. Schweiger, T. Stöhlker, S. Sturm, R. N. Wolf, S. Bernitt, J.R.Crespo López-Urrutia  
*Review of Scientific Instruments* **89**(6), 063109 (2018); DOI:10.1063/1.5026961
15. “High-Speed Terahertz Waveform Measurement for Intense Terahertz Light Using 100-kHz Yb-Doped Fiber Laser”  
M. Tsubouchi, K. Nagashima  
*Sensors* **18**, 1936 (2018); DOI:10.3390/s18061936
16. “Coherent, Short-Pulse X-ray Generation via Relativistic Flying Mirrors”  
M. Kando, T. Zh. Esirkepov, J. K. Koga, A. S. Pirozhkov, S. V. Bulanov  
*Quantum Beam Science* **2**(2), 9 (2018); DOI:10.3390/qubs2020009
17. “Interstitial-atom-induced phase transformation upon hydrogenation in vanadium”  
K. Sakaki, H. Kim, K. Iwase, E. H. Majzoub, A. Machida, T. Watanuki, Y. Nakamura  
*Journal of Alloys and Compounds* **750**, 33 - 41 (2018); DOI:10.1016/j.jallcom.2018.03.345
18. “Influence of short pulse duration of carbon-dioxide lasers on extreme ultraviolet emission from laser produced plasmas”  
R. Amano, T.-H. Dinh, A. Sasanuma, G. Arai, H. Hara, Y. Fujii, T. Hatano, T. Ejima, W. Jiang, A. Sunahara, A. Takahashi, D. Nakamura, T. Okada, K. Sakaue, T. Miura, G. O’Sullivan, T. Higashiguchi  
*Japanese Journal of Applied Physics* **57**(7), 070311 (2018); DOI:10.7567/JJAP.57.070311
19. “Metamagnetic jump in the spin-1/2 antiferromagnetic Heisenberg model on the square kagome lattice”  
Y. Hasegawa, H. Nakano, T. Sakai  
*Physical Review B* **98**(1), 014404 (2018); DOI:10.1103/PhysRevB.98.014404
20. “Emission of water-window soft x-rays under optically thin conditions using low-density foam targets”  
H. Hara, H. Kawasaki, T. Tamura, T. Hatano, T. Ejima, W. Jiang, H. Ohashi, S. Namba, A. Sunahara, A. Sasaki, M. Nishikino, G. O’Sullivan, T. Higashiguchi  
*Optics Letters* **43**(15), 3750 – 3753 (2018); DOI:10.1364/OL.43.003750
21. “Review of HPLSE special issue on target fabrication”  
C. Spindloe, Y. Fukuda, P. Fitzsimmons, K. Du, C. Danson  
*High Power Laser Science and Engineering* **6**, e13 (2018); DOI:10.1017/hpl.2018.10
22. “Transition from nonlocal electron transport to radiative regime in an expanding blast wave”  
A. Marocchino, A. Rivasio, A. Levy, L. Lancia, Y. Fukuda, S. Jinno, S. Atzeni, D. Doria, C. Prigent, E. Lamour, D. Vernhet, M. Borghesi, L. Romagnani  
*Applied Physics Letters* **112**, 264104 (2018); DOI:10.1063/1.5022698
23. “Mutagenic potential of 8-oxo-7,8-dihydroguanine (8-oxoG) is influenced by nearby clustered lesions”  
N. Shikazono, K. Akamatsu  
*Mutation Research* **810**, 6 – 12 (2018); DOI:10.1016/j.mrfmmm.2018.05.001
24. “Development of a multialkali photocathode dc gun for a Smith-Purcell terahertz free-electron laser”  
N. Nishimori, R. Nagai, M. Sawamura, R. Hajima  
*Particles* **1**(1), 166 - 174 (2018); DOI:10.3390/particles1010012

25. “Collimated gamma rays from laser wakefield accelerated electrons”  
M.H. Li, L.M. Chen, D. Li, K. Huang, Y. Li, Y. Ma, W. Yan, M. Tao, J. Tan, Z. Sheng, J. Zhang  
*Matter and Radiation at Extremes* **3(4)**, 188 - 196 (2018); DOI:10.1016/j.mre.2018.03.002
26. “Relativistically upshifted higher harmonic generation via relativistic flying mirrors”  
J. K. Koga, S. V. Bulanov, T. Zh. Esirkepov, M. Kando, S. S. Bulanov, A. S. Pirozhkov  
*Plasma Physics and Controlled Fusion* **60(7)**, 074007 (2018); DOI:10.1088/1361-6587/aac068
27. “Aperiodic reflection diffraction gratings for soft X-ray radiation and their application”  
E. A. Vishnyakov, A. O. Kolesnikov, A. S. Pirozhkov, E. N. Ragozin, A. N. Shatokhin  
*Quantum Electronics* **48(10)**, 916 - 929 (2018); DOI:10.1070/QEL16707
28. “Study of damage structure formation on aluminum film targets by picosecond soft X-ray laser ablation around threshold region”  
M. Ishino, N. A. Inogamov, S. Tamotsu, V. V. Zhakhovsky, N. Hasegawa, I. Yu. Skobelev, A. Ya. Faenov, T.A. Pikuz, K. Mikami, T. Kawachi, M. Nishikino  
*Applied Physics A* **124**, 649 (2018); DOI:10.1007/s00339-018-2072-9
29. “Variable-bandwidth  $^{57}\text{Fe}$  Synchrotron Mössbauer Source”  
T. Mitsui, R. Masuda, M. Seto, N. Hirao  
*Journal of the Physical Society of Japan* **87**, 093001 (2018); DOI:10.7566/JPSJ.87.093001
30. “Extraction of Physical Parameters from X-ray Spectromicroscopy Data Using Machine Learning”  
Y. Suzuki, H. Hino, T. Ueno, Y. Takeichi, M. Kotsugi, K. Ono  
*Microscopy and Microanalysis* **24(S2)**, 478 - 479 (2018); DOI:10.1017/S1431927618014629
31. “Optimal Design of Experiment for X-Ray Spectromicroscopy by Machine Learning”  
T. Ueno, H. Hino, K. Ono, *Microscopy and Microanalysis* **24(S2)**, 134 – 135 (2018); DOI:10.1017/S1431927618013065
32. “MNase, as a probe to study the sequence-dependent site exposures in the +1 nucleosomes of yeast”  
D. Luo, D. Kato, J. Nogami, Y. Ohkawa, H. Kurumizaka, H. Kono  
*Nucleic Acids Research* **46(14)**, 7124 - 7137 (2018); DOI:10.1093/nar/gky502
33. “Observation of coherent undulator radiation in THz region”  
S. Kashiwagi, T. Abe, H. Saito, F. Hinode, K. Kanomata, S. Miura, T. Muto, I. Nagasawa, K. Nanbu, S. Ninomiya, N. Nishimori, Y. Saito, K. Takakashi, H. Hama  
*Infrared Physics & Technology* **93**, 335 - 339 (2018); DOI:10.1016/j.infrared.2018.08.011
34. “Cs 吸着バーミキュライトの軟 X 線放射光光電子分光”  
寺岡 有殿  
SPRING-8/SACLA 利用研究成果集 **6(2)**, 219 - 222 (2018); DOI:10.18957/rr.6.2.219
35. “水素貯蔵合金の水素ガス圧力下における水素化反応過程その場 X 線回折測定用の新規試料容器の検討”  
町田 晃彦, 綿貫 徹, 榑 浩司, Hyunjeong Kim, 浅野 耕太, 中村 優美子  
SPRING-8/SACLA 利用研究成果集 **6(2)**, 185 - 189 (2018); DOI:10.18957/rr.6.2.185
36. “High-contrast high-intensity repetitive petawatt laser”  
H. Kiriya, A. S. Pirozhkov, M. Nishiuchi, Y. Fukuda, K. Ogura, A. Sagisaka, Y. Miyasaka, M. Mori, H. Sakaki, P. N. Dover, K. Kondo, J. K. Koga, T. Zh. Esirkepov, M. Kando, K. Kondo  
*Optics Letters* **43(11)**, 2595 – 2598 (2018); DOI:10.1364/OL.43.002595
37. “Ce Substitution and Reduction Annealing Effects on Electronic States in  $\text{Pr}_{2-x}\text{Ce}_x\text{CuO}_4$  Studied by Cu *K*-edge X-ray Absorption Spectroscopy”  
S. Asano, K. Ishii, D. Matsumura, T. Tsuji, T. Ina, K. M. Suzuki, M. Fujita  
*Journal of the Physical Society of Japan* **87(9)**, 094710 (2018); DOI:10.7566/JPSJ.87.094710

38. “Optimized negative thermal expansion induced by gradual intermetallic charge transfer in  $\text{Bi}_{1-x}\text{Sb}_x\text{NiO}_3$ ”  
T. Nishikubo, Y. Sakai, K. Oka, M. Mizumaki, T. Watanuki, A. Machida, N. Maejima, S. Ueda, T. Mizokawa, M. Azuma  
*Applied Physics Express* **11**(6), 061102 (2018); DOI:10.7567/APEX.11.061102
39. “Effect of *B*-site randomness on antiferroelectric/relaxor nature of ground state: diffuse and inelastic X-ray scattering study of  $\text{Pb}(\text{In}_{1/2}\text{Nb}_{1/2})\text{O}_3$ ”  
K. Ohwada, S. Tsukada, T. Fukuda, S. Tsusui, A. Q. R. Baron, J. Mizuki, H. Ohwa, N. Yasuda, H. Terauchi  
*Physical Review B* **98**, 054106 (2018); DOI:10.1103/PhysRevB.98.054106
40. “Structural Variation of Self-Organized Mg Hydride Nanoclusters in Immiscible Ti Matrix by Hydrogenation”  
K. Asano, H. Kim, K. Sakaki, K. Jimura, S. Hayashi, Y. Nakamura, K. Ikeda, T. Otomo, A. Machida, T. Watanuki  
*Inorganic Chemistry* **57**(18), 11831 - 11838 (2018); DOI:10.1021/acs.inorgchem.8b02015
41. “Performance of a flat-field grating spectrometer for tender X-ray emission spectroscopy”  
T. Imazono, R. Ukita, H. Nishihara, H. Sasai, T. Nagano  
*Applied Optics* **57**(27), 7770 -7777 (2018); DOI:10.1364/AO.57.007770
42. “Spectral dynamics of soft X-ray emission in dual-laser-produced medium-Z plasma”  
H. Ohashi, H. Hara, G. Arai, T. Hatano, T. Ejima, C. Suzuki, S. Namba, A. Sasaki, M. Nishikino, G. O'Sullivan, T. Higashiguchi,  
*Appl. Phys. B* **124**, 193 (2018); DOI:10.1007/s00340-018-7061-3
43. “Radiocesium interaction with clay minerals: Theory and simulation advances Post-Fukushima”  
M. Okumura, S. Kerisit, I. C. Bourg, L. N. Lammers, T. Ikeda, M. Sassi, K. M. Rosso, M. Machida  
*Journal of Environmental Radioactivity* **189**, 135 - 145 (2018); DOI:10.1016/j.jenvrad.2018.03.011
44. “Ground-State Phase Diagram of an Anisotropic  $S = 1/2$  Ladder with Different Leg Interactions”  
T. Tonegawa, T. Hikihara, K. Okamoto, S. Furuya, T. Sakai  
*Journal of the Physical Society of Japan* **87**(10), 104002 (2018); DOI:10.7566/JPSJ.87.104002
45. “Precise Estimation of the  $S = 2$  Haldane Gap by Numerical Diagonalization”  
H. Nakano, T. Sakai  
*Journal of the Physical Society of Japan* **87**(10), 105002 (2018); DOI:10.7566/JPSJ.87.105002
46. “Deep-hole drilling of amorphous silica glass by extreme ultraviolet femtosecond pulses”  
T. Shibuya, T. Takahashi, K. Sakaue, T.-H. Dinh, H. Hara, T. Higashiguchi, M. Ishino, Y. Koshiba, M. Nishikino, H. Ogawa, M. Tanaka, M. Washio, Y. Kobayashi, R. Kuroda  
*Applied Physics Letters* **113**, 171902 (2018); DOI:10.1063/1.5046125
47. “Intense water-window soft x-ray emission by spectral control using dual laser pulses”  
G. Arai, H. Hara, T. Hatano, T. Ejima, W. Jiang, H. Ohashi, S. Namba, A. Sunahra, A. Sasaki, M. Nishikino, G. O'Sullivan, T. Higashiguchi  
*Optics express* **26**(21), 27748 - 27756 (2018); DOI:10.1364/OE.26.027748
48. “Investigating the Influence of Arginine Dimethylation on Nucleosome Dynamics Using All-Atom Simulations and Kinetic Analysis”  
Z. Li, H. Kono  
*The Journal of Physical Chemistry B* **122**(42), 9625 - 9634 (2018); DOI:10.1021/acs.jpcb.8b05067
49. “X-ray Absorption Study of Platinum Nanoparticles on an Ion-Irradiated Carbon Support”  
K. Kakitani, T. Kimura, T. Yamaki, S. Yamamoto, D. Matsumura, T. Taguchi, T. Terai  
*Radiation Physics and Chemistry* **153**, 152 - 155 (2018); DOI:10.1016/j.radphyschem.2018.09.017
50. “On annihilation of the relativistic electron vortex pair in collisionless plasmas”  
K. V. Lezhnin, F. F. Kamenets, T. Zh. Esirkepov, S. V. Bulanov  
*Journal of Plasma Physics* **84**(6), 905840610 (2018); DOI:10.1017/S0022377818001162

51. “Nuclear Bragg reflection of  $^{57}\text{FeBO}_3$  in radio-frequency magnetic field observed with Si-APD linear array detector”  
S. Kishimoto, R. Haruki, R. Masuda, M. Tanaka, T. Mitsui  
*Japanese Journal of Applied Physics* **58**, 016501 (2018); DOI:10.7567/1347-4065/aae89c
52. “Lattice parameter evolution during heating of Ti-45Al-7.5Nb-0.25/0.5C alloys under atmospheric and high pressures”  
X. Li, R. Dippenaar, A. Shiro, T. Shobu, Y. Higo, M. Reid, H. Suzuki, K. Akita, K. Funakoshi, K.-D. Liss  
*Intermetallics* **102**, 120-131 (2018); DOI:10.1016/j.intermet.2018.08.011
53. “Third Boundary of the Shastry-Sutherland Model by Numerical Diagonalization”  
H. Nakano, T. Sakai  
*Journal of the Physical Society of Japan* **87**(12), 123702 (2018); DOI:10.7566/JPSJ.87.123702
54. “非侵襲の光血糖計測”  
山川 考一  
*糖尿病* **61**(12), 812 - 814 (2018); DOI:10.11213/tonyoby.61.812
55. “Hydration structures of the human protein kinase CK2 $\alpha$  clarified by joint neutron and X-ray crystallography”  
C. Shibasaki, S. Arai, R. Shimizu, M. Saeki, T. Kinoshita, A. Ostermann, T. R. Schrader, Y. Kurosaki, T. Sunami, R. Kuroki, M. Adachi  
*Journal of Molecular Biology* **430**(24), 5094 - 5104 (2018); DOI:10.1016/j.jmb.2018.09.018
56. “Electronic properties and compressional behavior of Fe-Si alloys at high pressure”  
K. Seiji, S. Nanami, M. Fumiya, H. Naohisa, H. Maki, O. Eiji, M. Ryo, T. Mitsui, O. Yasuo, S. Nakano  
*American Mineralogist: Journal of Earth and Planetary Materials* **103**, 1959 - 1965 (2018); DOI:10.2138/am-2018-6425
57. “Crystal rotation and microstructures in an aluminum single-slip system under tensile loading”  
Y. Yoshida, J. Shibano, K. Fukuda, K. Terabayashi, M. Eguchi, K. Kajiwar, T. Shobu, A. Shiro  
*Materials Characterization* **146**, 121 - 126 (2018); DOI:10.1016/j.matchar.2018.10.001
58. “Superfluorescence, free-induction decay, and four-wave mixing: propagation of free-electron laser pulses through a dense sample of helium ions”  
J. R. Harries, H. Iwayama, S. Kuma, M. Iizawa, N. Suzuki, Y. Azuma, I. Inoue, S. Owada, T. Togashi, K. Tono, M. Yabashi, E. Shigemasa  
*Physical Review Letters* **121**(26), 263201 (2018); DOI:10.1103/PhysRevLett.121.263201
59. “Variations of lattice constants and thermal expansion coefficients of indium at high pressure and high temperature”  
Y. Takubo, H. Terasaki, T. Kondo, S. Mitai, S. Kamada, T. Kikegawa, A. Machida  
*High Pressure Research* **38**(4), 406 - 413 (2018); DOI:10.1080/08957959.2018.1499903
60. “Zeolitic interlayer microchannels of magadiite, a natural layered silicate, to boost green organic synthesis”  
Y. Ide, S. Tominaka, H. Kono, R. Ram, A. Machida, N. Tsunoji  
*Chemical Science* **9**(46), 8637 - 8643 (2018); DOI:10.1039/c8sc03712d
61. “Improvement study on heat resistance of multilayer-coated replica gratings”  
T. Imazono, H. Nishihara, R. Ukita, H. Sasai, T. Nagano  
*The American Institute of Physics (AIP) Conference Proceedings* **2054**, 060020 (2019); DOI:10.1063/1.5084651
62. “Mo-overcoated grating-based beam intensity monitor for 13.9 nm X-ray laser”  
T. Imazono, H. Nishihara, R. Ukita, H. Sasai, T. Nagano  
*The American Institute of Physics (AIP) Conference Proceedings* **2054**, 060050 (2019); DOI:10.1063/1.5084681
63. “64- and 128-pixel Si-APD linear array X-ray detectors with 0.5 ns time resolution”  
S. Kishimoto, T. Mitsui, R. Haruki, S. Shimazaki, M. Tanaka  
*AIP Conference Proceedings* **2054**, 060068 (2019); DOI:10.1063/1.5084699

64. “Superconductivity of the hydrogen-rich metal hydride  $\text{Li}_5\text{MoH}_{11}$  under high pressure”  
D. Meng, M. Sakata, K. Shimizu, Y. Iijima, H. Saitoh, T. Sato, S. Takagi, S. Orimo  
*Physical Review B* **99**, 024508 (2019); DOI:10.1103/PhysRevB.99.024508
65. “Resonant-Auger-state-selected dissociation dynamics and dissociation limits of  $\text{N } 1s \rightarrow \pi^*$  core excited  $\text{N}_2$  molecules studied using a two-dimensional Auger-electron-photoion coincidence method”  
H. Iwayama, J. R. Harries  
*Journal of Electron Spectroscopy and Related Phenomena* **232**, 40 - 44 (2019); DOI:10.1016/j.elspec.2019.01.005
66. “Quasimonoenergetic Proton Bunch Acceleration Driven by Hemispherically Converging Collisionless Shock in a Hydrogen Cluster Coupled with Relativistically Induced Transparency”  
R. Matsui, Y. Fukuda, Y. Kishimoto  
*Physical Review Letters* **122**(1), 014804 (2019); DOI:10.1103/PhysRevLett.122.014804
67. “Brilliant gamma-ray beam and electron–positron pair production by enhanced attosecond pulses”  
Y.-J. Gu, O. Klimo, S. V. Bulanov, S. Weber  
*Communications Physics* **1**(93), 1 - 9 (2019); DOI:10.1038/s42005-018-0095-3
68. “Analysis on the longitudinal field strength formed by tightly-focused radially-polarized femtosecond petawatt laser pulse”  
T. M. Jeong, S. V. Bulanov, S. Weber, G. Korn  
*Optics Express* **26**(25), 33091 - 33107 (2019); DOI:10.1364/OE.26.033091
69. “In Situ Time-Resolved XAFS Studies on Laser-Induced Particle Formation of Palladium Metal in an Aqueous / EtOH Solution”  
M. Saeki, D. Matsumura, T. Yomogida, T. Taguchi, T. Tsuji, H. Saitoh, H. Ohba  
*Journal of Physical Chemistry C* **123**(1), 817-824 (2019); DOI:10.1021/acs.jpcc.8b09532
70. “Theory for the electron excitation in dielectrics under an intense linear and circularly polarized laser field”  
T. Otobe, Y. Shinohara, S. A. Sato, K. Yabana  
*Journal of the Physical Society of Japan* **88**, 024706 (2019); DOI:10.7566/JPSJ.88.024706
71. “First principles isothermal-isobaric centroid molecular dynamics simulation of high pressure ices”  
T. Ikeda  
*Chemical Physics Letters* **717**, 141 - 146 (2019); DOI:10.1016/j.cplett.2019.01.008
72. “SALMON: Scalable Ab-initio Light-Matter simulator for Optics and Nanoscience”  
M. Noda, S. A. Sato, Y. Hirokawa, M. Uemoto, T. Takeuchi, S. Yamada, A. Yamada, Y. Shinohara, M. Yamaguchi, K. Iida, I. Floss, T. Otobe, K.-M. Lee, K. Ishimura, T. Bok, G. F. Bertsch, K. Nobusada, K. Yabana  
*Computer Physics Communications* **235**, 356 (2019); DOI:10.1016/j.cpc.2018.09.018
73. “Polarization rotation associated with phonon dynamics in monoclinic C phase near morphotropic phase boundary studied by diffuse and inelastic X-ray scattering from a Ti-composition-gradient  $\text{Pb}[(\text{Mg}_{1/3}\text{Nb}_{2/3})_{1-x}\text{Ti}_x]\text{O}_3$  single crystal”  
K. Ohwada, T. Tsukada, M. Matsuura, S. Tsutsui, A. Q. R. Baron, J. Mizuki, K. Namikawa  
*Ferroelectrics* **532**, 100 - 110 (2019); DOI:10.1080/00150193.2018.1430430
74. “Effect of Cu intercalation and pressure on excitonic interaction in  $1T\text{-TiSe}_2$ ”  
S. Kitou, A. Nakano, S. Kabayashi, K. Sugawara, N. Katayama, N. Maejima, A. Machida, T. Watanuki, K. Ichimura, S. Tanda, T. Nakamura, H. Sawa  
*Physical Review B* **99**(10), 104109 (2019); DOI:10.1103/PhysRevB.99.104109
75. “Development of CdTe Pixel Detectors for Energy-resolved X-ray Diffractions”  
H. Toyokawa, C. Saji, M. Kawase, K. Ohara, A. Shiro, R. Yasuda, T. Shobu, A. Suenaga, H. Ikeda  
*JPS Conference Proceedings* **24**, 011015 (2019); DOI:10.7566/JPSCP.24.011015

76. “Enhancement of water-window soft x-ray emission from laser-produced Au plasma under low-pressure nitrogen atmosphere”  
C. John, M. Kishimoto, T. Johzaki, T. Higashiguch, N. Kakunaka, Y. Matsumoto, N. Hasegawa, M. Nishikino, T. Ejima,  
A. Sunahara, T. Endo  
*Optics Letters* **44**(6), 1439 - 1442 (2019); DOI:10.1364/OL.44.001439
77. “Anisotropy and polarization dependence of multiphoton charge carrier generation rate in diamond”  
M. Kozák, T. Otobe, M. Zukerstein, F. Trojanek, P. Maly  
*Physical Review B* **99**, 104305 (2019); DOI:10.1103/PhysRevB.99.104305
78. “Pressure-induced collapse of the spin-orbital Mott state in the hyperhoneycomb iridate  $\beta$ -Li<sub>2</sub>IrO<sub>3</sub>”  
T. Takayama, A. Krajewska, A. S. Gibbs, A. N. Yaresko, H. Ishii, H. Yamaoka, K. Ishii, N. Hiraoka, N. P. Funnell, C. L. Bull,  
H. Takagi  
*Physical Review B* **99**(12), 125127 (2019); DOI:10.1103/PhysRevB.99.12512



## [Proceedings]

1. “Ground state with nonzero spontaneous magnetization of the two-dimensional spin-1/2 Heisenberg antiferromagnet with frustration”  
T. Sakai, H. Nakano  
*AIP Advances* **8**, 101408 (2018); DOI:10.1063/1.5042780
2. “電気光学効果を用いたレーザー加速電子の パルス長・タイミングの計測”  
神門 正城, 黄 開, エシロケポフ ティムル, コーガ ジェームズ, 小瀧 秀行, 森 道昭, 林 由紀雄,  
中新 信彦, プラノフ セルゲイ  
*Proceedings of the 15th Annual Meeting of Particle Accelerator Society of Japan*, 637 – 639 (2018)
3. “レーザー打音法の道路トンネルにおける実証試験について”  
長谷川 登, 岡田 大, 近藤 修司, 三上 勝大, 北村 俊幸, 錦野 将元, 河内 哲哉, 倉橋 慎理, 島田 義則  
*レーザー学会第 523 回研究会報告* **18(21)**, 19 - 22 (2018)
4. “X-ray emission from stainless steel foils irradiated by femtosecond petawatt laser pulses”  
M. A. Alkhimova, A. Ya. Faenov, T. A. Pikuz, I. Yu. Skobelev, S. A. Pikuz, M. Nishiuchi, H. Sakaki, A. S. Pirozhkov,  
S. Sagisaka, N. P. Dover, K. Kondo, K. Ogura, Y. Fukuda, H. Kiriya, T. Esirkepov, S. V. Bulanov, A. Andreev, M. Kando,  
A. Zhidkov, K. Nishitani, T. Miyahara, Y. Watanabe, R. Kodama, K. Kondo  
*Journal of Physics: Conference Series* **946(1)**, 012018 (2018); DOI:10.1088/1742-6596/946/1/012018
5. “Application of simple formulas to track potential in heavy-ion-beam simulation”  
K. Moribayashi  
*Transactions of the Material Research Society of Japan* **43(5)**, 267 - 270 (2018); DOI:10.14723/tmrj.43.267
6. “Spontaneous Magnetization of the Spin-1/2 Heisenberg Antiferromagnet on the Triangular Lattice with a Distortion”  
A. Shimada, T. Sakai, H. Nakano, K. Yoshimura  
*Journal of Physics: Conference Series* **969(1)**, 012126 (2018); DOI:10.1088/1742-6596/969/1/012126
7. “Quantum Spin Fluid Behaviors of the Kagome- and Triangular-Lattice Antiferromagnets”  
T. Sakai, H. Nakano  
*Journal of Physics: Conference Series* **969(1)**, 012127 (2018); DOI:10.1088/1742-6596/969/1/012127
8. “Generation of 1-MeV Quasi-Monochromatic Gamma-Rays for Precise Measurement of Delbrück Scattering by Laser Compton Scattering”  
H. Zen, T. Kii, H. Ohgaki, T. Hayakawa, T. Shizuma, J. K. Koga, E. Salehi, M. Fujimoto  
*Proceedings of IPAC2018* **1067**, 092003 (2018); DOI:10.1088/1742-6596/1067/9/092003
9. “Development of soft x-ray laser irradiation beamline for ablation and damage study”  
M. Ishino, T.-H. Dinh, N. Hasegawa, K. Sakaue, T. Higashigushi, S. Ichimaru, M. Hatayama, M. Washio, M. Nishikino  
*Proceedings of SPIE* **10905**, 109051C (2019)

## [表彰]

1. 遠藤 友随：「光・量子ビーム科学合同シンポジウム 2018 ベストポスター賞」（2018年5月9日）  
“Branching ratio control of Coulomb explosion of OCS by two-color laser fields”
2. 稲見 俊哉：「理事長表彰 研究開発功績賞特賞」（2018年7月3日）  
“X線の新しい磁気光学効果に関する研究”
3. 綿貫 徹：「理事長表彰 模範賞」（2018年7月3日）  
“独自開発した先端的放射光利用技術の提供による高い成果の創出”
4. 森井 厚作「応用物理学会放射線分科会 学生ポスター賞」（2018年9月21日）  
“固体飛跡検出器 CR-39 を用いた水素クラスターのクーロン爆発で加速される MeV 級陽子線の計測”
5. 石田 恒：「HPCI システム利用研究課題 優秀成果賞受賞」（2018年11月2日）  
“分子シミュレーションによるヌクレオソーム結合様式の網羅的探索”
6. 藤原 孝将, 三井 隆也：「International Workshop on New Developments and Prospects for the Future of Mössbauer Spectroscopy (IWMS2018) ポスター賞」（2018年11月16日）  
“Development and application for Mobile Type Nuclear Monochromator of 57-iron”
7. 谷上 真惟：「水素化物に関わる次世代学術・応用展開研究会 若手研究者表彰 最優秀賞」（2018年11月22日）  
“難水素化金属からなる Al-Fe 系合金の高温高压水素化”
8. 藤尾 昂司：「第2回 QST 国際シンポジウム ベストポスター賞」（2018年11月29日）  
“Fundamental study of phase-control-free coherent-beam combining toward femtosecond-pulse amplification in bulk medium”

## [特許登録]

1. 「レーザー装置」, 特許番号：6341596（登録日 2018年5月25日）  
山川 考一, 赤羽 温
2. 「血中物質濃度測定装置及び血中物質濃度測定方法」、特許番号：6415606（登録日 2018年10月12日）  
山川 考一

## [特許出願]

1. 「組織識別装置、組織識別システム、組織識別方法、内視鏡システム、組織識別プログラムおよび記録媒体」（特願 2018-90871）  
山川 考一, 青山 誠, 森岡 孝満, 今岡 達彦
2. 「水素吸蔵材、水素化水素吸蔵材の製造方法および水素吸蔵合金の製造方法」（特願 2018-094658）  
齋藤 寛之, 谷上 真惟, 森本 勝太, 綿貫 徹
3. 「レーザー装置、光源および測定装置」（PCT/JP2018/031387）  
赤羽 温, 青山 誠, 小川 奏, 山川 考一
4. 「インプラント設置強度評価方法、インプラント設置強度評価装置、およびプログラム」（PCT/JP2018/033978）  
錦野 将元, 長谷川 登, 三上 勝大, 北村 俊幸, 近藤 修司, 岡田 大
5. 「血中物質濃度測定装置及び血中物質濃度測定方法」（特願 2018-187388）  
山川 考一
6. 「磁性体観察方法、磁性体観察装置」（PCT/JP2019/010467）  
稲見 俊哉, 安田 良, 綿貫 徹, 上野 哲朗
7. 「計測装置、計測システム、移動体、および計測方法」（PCT/JP2019/13302）  
錦野 将元, 長谷川 登, 三上 勝大, 北村 俊幸, 近藤 修司, 岡田 大, 河内 哲哉

# The Kids' Science Museum of Photons

## 概要

4月16日～22日の科学技術週間では、磁石やコイル、DNA模型などの工作に加え、機械部品をモチーフにした、メカスーパーボールやメカレジン工作を楽しんでいただきました。また、映像ホールの新メニュー「恐竜の記憶」は躍動感のある素晴らしいコンテンツで、一日に連続2回上映することもあったほど、多くの方々にご観賞いただきました。

5月27日には、日本宇宙少年団（YAC）によるイベントが多目的ホール棟で開催され、ふおとん来館者からもコラボ工作の「ソーラーハウス」に参加されました。

7月6日、梅雨明け前の豪雨は館内マルチホール（工作室）の床に浸水し、工務課、庶務課、水用掃除機を貸してくださった方々のご支援の下、開館準備を整えたものの、翌日七夕の土曜日もあわせて大雨警報発令のため、休館となってしまいました。8日の日曜日には、500人超のお客様にご来館いただきました。

今年の夏も、人気の恐竜シリーズ、海賊船、星座表、レジンなど盛りだくさんの工作を企画し、子どもたちに楽しんでいただきました。8月8日～8月15日には、ふおとん OG・OB と関西研の研究員にご支援いただいて、DNA模型や磁石、偏光フィルム、紙コップカメラなどの工作も行い、また、奈良女子大からの2名の学芸員実習生にもご協力いただき、メインイベントを大いに盛り上げていただきました。さらに、ロビー工作では、ふおとんボランティア OB と夏休み期間限定業務補助員の方々に、サマースタッフとしてお手伝いいただきました。お盆明けには、アマチュア無線社団局に参画いただき、免許不要の無線機の貸し出しによる「無線ごっこ」を来館者に体験いただきました。

秋分の日（9/23）の YAC とのコラボ工作（第2弾）「どうして飛行機は飛ぶの？」では、YAC ならではの飛行のしくみのお勉強のあと、工作、実験、滑走記録会もあり、1.5時間のとても充実したイベントになりました。

10月28日の施設公開日には、研究所での実験・工作と科学館でのハロウィンイベントの両方を楽しもう！とスケジュールを事前に考えてきてくれた子どもたちで賑わいました。またこの日には、人気映画「恐竜の記憶」を3回上映し、それを目当てに来館されたお客様にも喜んでいただくことができました。

11月、ハロウィンの翌日から、館内の飾りはすっかりクリスマス。週末の工作ももちろんクリスマス仕様となりましたが、中でも23日（金・祝）の「クリスマスレジン」には冷え込む朝から列ができ、開館20分後には午後の工作分まで満席になりました。

12月、映像ホールにて幼児向け新番組「こぐま座のティオ」を上映しました。クイズに答えたり歌をうたったりと参加しながら楽しめるので、人気の高いイベントとなりました。

新年のイベントは1月4日から元気にスタートしましたが、空調設備更新のため、1月15日から3月27日まで休館しました。これにともない、1月17日より（3月27日まで）、関西光科学研究所「多目的ホール」にて、工作を中心とした「ミニふおとん」をオープンしました。3月28日より、科学館での通常運用を再開しました。

## I. 2018 年度の活動

### 1. 主な行事

#### <2018 年>

4 月 1、7、8、14、15、21、22、28～30 日	Photons de Science & Technology 2018
5 月 3～6、12、13、19、20、26、27 日	Photons Festival 2018
6 月 2、3、9、10、16、17、23、24、30 日	Photons de DINOSAUR
7 月 1、8、14～16、21、22、25～29 日	Photons de UNIVERSE
8 月 1～5、8～15、18、19、22～26、29～31 日	Photons de 親子工作夏休み
8 月 8～15 日	博物館（学芸員）実習生・科学館研修生（インターンシップ）として、 奈良女子大学より学生 2 名受入れ
9 月 1、2、8、9、15～17、22～24、29 日	Photons de Happy Halloween 1 <sup>st</sup> 2018
10 月 8、13、14、20、21、27、28 日	Photons de Happy Halloween 2 <sup>nd</sup> 2018
11 月 3、4、10、11、17、18、23～25 日	Photons Merry Christmas 1 <sup>st</sup> 2018
12 月 1、2、8、9、15、16、22～24、27、28 日	Photons Merry Christmas 2 <sup>nd</sup> 2018
12 月 1～24 日	つくばエキスポセンター第 20 回全国ジュニア発明展（巡回展示）

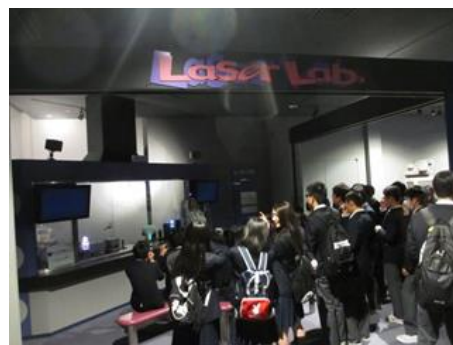
#### <2019 年>

1 月 4～6、12～14 日	ふおとん de はっぴい NewYear 2019
1 月 17 日～3 月 27 日（月・火曜日除く*）	ミニふおとん
*2 月 11 日（月・祝）オープン 2 月 12、13 日クローズ	

### 2. 事業内容（実験・工作・映像）

#### （1）レーザーラボ

Nd:YAG や He-Ne レーザー、分光器等を用いた光及びレーザーのライブ実験を行っています。通常スケジュール、（午前）10:30～10:50 と 11:40～12:00、（午後）15:00～15:20、に加え、団体見学者用に適宜実施しました。2018 年度（2019 年 1 月 14 日までと 3 月 28 日から 31 日まで）の観覧者総数は 8,000 人。



レーザーラボ実績（2018 年 4 月 1 日～2019 年 1 月 14 日及び 3 月 28 日～31 日）

年 月	実施日数	実施回数	観覧者数	累積観覧者数
2018 年 4 月	15 日	26 回	548 人	548 人
5 月	15 日	28 回	743 人	1,291 人
6 月	15 日	26 回	692 人	1,983 人
7 月	18 日	39 回	1,123 人	3,106 人
8 月	23 日	69 回	2,291 人	5,397 人
9 月	14 日	33 回	744 人	6,141 人



10 月	14 日	30 回	514 人	6,655 人
11 月	17 日	34 回	409 人	7,064 人
12 月	15 日	32 回	453 人	7,517 人
2019 年 1 月	7 日	19 回	379 人	7,896 人
2 月	-	-	-	-
3 月	4 日	6 回	104 人	8,000 人
年度合計	157 日	342 回	8,000 人	-

## (2) レーザー加工体験

木製ブロックに、レーザーで文字や絵を刻印する「レーザー加工」を体験いただいています。主に、土日祝日等イベント開催日の10:30～11:30、14:00～14:45に加え、団体見学者用に適宜実施しました。2018年度(2019年1月14日までと3月28日から31日まで)の体験者総数は440人。なお、8月は夏休みイベントのためお休みしました。



レーザー加工体験実績(2018年4月1日～2019年1月14日及び3月28日～31日)

年 月	実施日数	実施回数	体験者数	累積体験者数
2018 年 4 月	5 日	5 回	8 人	8 人
5 月	4 日	4 回	8 人	16 人
6 月	6 日	6 回	14 人	30 人
7 月	4 日	4 回	12 人	42 人
8 月	-	-	-	-
9 月	7 日	7 回	101 人	143 人
10 月	8 日	8 回	67 人	210 人
11 月	8 日	8 回	33 人	243 人
12 月	6 日	6 回	48 人	291 人
2019 年 1 月	6 日	6 回	52 人	343 人
2 月	-	-	-	-
3 月	4 日	8 回	97 人	440 人
年度合計	58 日	62 回	440 人	-

## (3) 実験・工作教室

主に小学生を対象とした実験・工作教室をマルチホールとロビーにおいて開催しました。マルチホールでは、10:30～11:00、13:00～13:30と15:00～15:30、ロビーでは随時実施しました。

実験・工作教室実績（2018年4月1日～2019年1月14日及び3月28～31日）

年 月	実施日数		マルチホール実験・工作		ロビー工作
	マルチ	ロビー	実施回数	参加者数	参加者数
2018年4月	18日	20日	43回	422人	1,864人
5月	17日	20日	48回	594人	1,801人
6月	16日	21日	40回	298人	1,955人
7月	18日	19日	46回	400人	2,711人
8月	23日	23日	85回	846人	5,436人
9月	17日	19日	44回	496人	2,414人
10月	16日	18日	41回	409人	1,015人
11月	18日	20日	39回	291人	1,036人
12月	20日	20日	49回	603人	1,186人
2019年1月	8日	9日	19回	175人	768人
2月	-	-	-	-	-
3月	4日	4日	11回	103人	446人
年度合計	175日	193日	465回	4,637人	20,632人

（4）映像コンテンツの上映

光の映像ホール（ドーム型全天周映像ホール）において、通常スケジュール、11:10～11:30、14:00～14:30 と 15:40～16:00 に加え、団体見学者用に適宜、以下のコンテンツから1日あたり2～3作品の上映を行いました。2018年度（2019年1月14日までと3月28日から31日まで）の観覧者総数は32,930人でした。

1）映像コンテンツ

①プラネタリウム絵本「こぐま座のティオ」～星空だいぼうけん～（27分）

プラネタリウムに来てくれた君、ぼくと一緒に天の川のピンチを助けに行こう。春夏秋冬の星座のお友だちと力を合わせて、さあ、ポンプ座まで星空だいぼうけんの始まり！（2018年12月22日より上映開始）

②恐竜の記憶（25分）

国立科学博物館が収蔵する、ティラノサウルスとトリケラトプスの骨格標本を精確に三次元デジタル計測し、学術的監修のもとにバーチャルリアリティ映像としてコンテンツ化した立体感と奥行きのある高精細映像を投影。

③宇宙～その大きさを感じてみよう～（25分）

太陽系惑星の大きさ、距離、銀河系の大きさ、宇宙大規模構造等を学習する。

④ふと気になる宇宙（25分）

どこからが宇宙？宇宙の大きさって？等宇宙の話題について考える。

⑤THE MOON 月の不思議（25分）

月の満ち欠け、月面の様子、地球からの距離や大きさの比較、月の生成、誕生の歴史を学習する。

⑥ブラックホールの謎 (25 分)

ブラックホールや太陽系外惑星などを電磁波の旅で探る。

⑦今日の星空 (15 分)

今日の木津川市の星空を紹介する。



①

②

③

④

⑤

⑥

⑦

2) 上映実績 (2018 年 4 月 1 日～2019 年 1 月 14 日及び 3 月 28 日～31 日)

年 月	上映日数	上映回数	観覧者数	累積観覧者数
2018 年 4 月	18 日	52 回	3,068 人	3,068 人
5 月	21 日	55 回	3,350 人	6,418 人
6 月	20 日	54 回	2,807 人	9,225 人
7 月	19 日	67 回	4,487 人	13,712 人
8 月	23 日	82 回	7,276 人	20,988 人
9 月	20 日	60 回	3,703 人	24,691 人
10 月	19 日	53 回	2,100 人	26,791 人
11 月	21 日	49 回	1,832 人	28,623 人
12 月	20 日	56 回	2,066 人	30,689 人
2019 年 1 月	9 日	28 回	1,509 人	32,198 人
2 月	-	-	-	-
3 月	4 日	13 回	732 人	32,930 人
年度合計	194 日	569 回	32,930 人	-

### 3. 実験・工作実施例



磁石で前にならえ



コイルモーター



DNA 模型



メカレジン



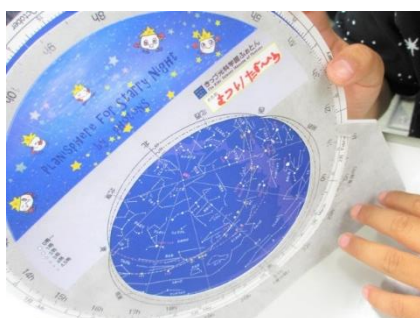
こいのぼりレジン



こいのぼりプラバン



母の日レジン



星座表を作ろう



ソーラータウン（日本宇宙少年団工作）



木津高校生（理科ー物理選択）来館



パタパタ ダイナソー

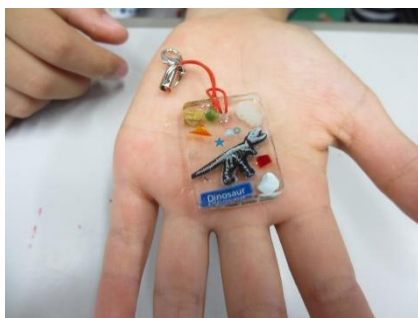


ダイナソースーパーボール





父の日レジン&プラバン



ダイナソーレジン



七夕飾り



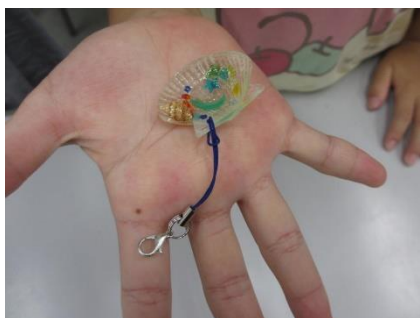
ミニミニ七夕



ユニバースプラバン



ユニバーススコープ



海の日レジン



ユニバースレジン



夏プラバン



The 海賊船



hey! らっしやい! (ミニ寿司工作)



ダイナソーフレーム



恐竜探検隊



恐竜探検隊ダイナソープラバン



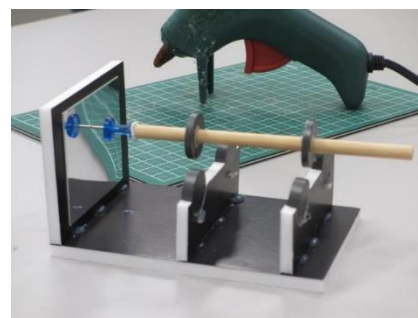
ダイナソーポラライザー



箱庭の宇宙



New スコープ



リニアの世界



ガウス加速器実験



プラバンミニ



パクパク紙コップ



スライム C



ハロウィンプラバン



ハロウィンスーパーボール





ハロウィンレジン



ハロウィンスコープ



クリスマスプラバン



クリスマススーパーボール



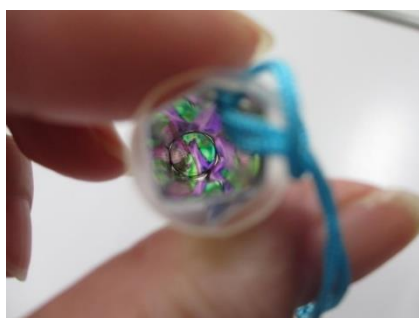
クリスマススコープ



クリスマスレジン



クリスマスリース



ミニミニスコープ



おせちレジン



福笑いプラバン

#### 4. ミニふおとん

##### (1) 光のミニラボ

多目的ホールの小ホールにおいて、光の三原色灯や偏光板、絵の具等を用いた“色の不思議”を体験していただくコーナーを開催しました。

実施実績（2019年1月17日～3月27日）

年 月	実施日数	実施回数	観覧者数	累積観覧者数
2019年1月	8日	38回	199人	199人
2月	19日	158回	761人	960人
3月	18日	264回	1,177人	2,137人
合計	45日	460回	2,137人	-

##### (2) ミニ工作

多目的ホールの中ホールとロビーにおいて、小さいお子様から参加できる工作教室を開催しました。

実施実績（2019年1月17日～3月27日）

年 月	実施日数		中ホール工作		ロビー工作
	中ホール	ロビー	実施回数	参加者数	参加者数
2019年1月	10日	8日	33回	212人	341人
2月	18日	18日	61回	553人	926人
3月	18日	18日	74回	796人	1,423人
合計	46日	44日	168回	1,561人	2,690人

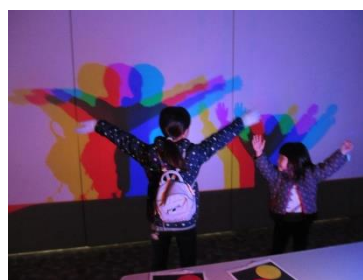
##### (3) 実施風景



ロビー



中ホール



小ホール

## Ⅱ. 2018 年度利用状況

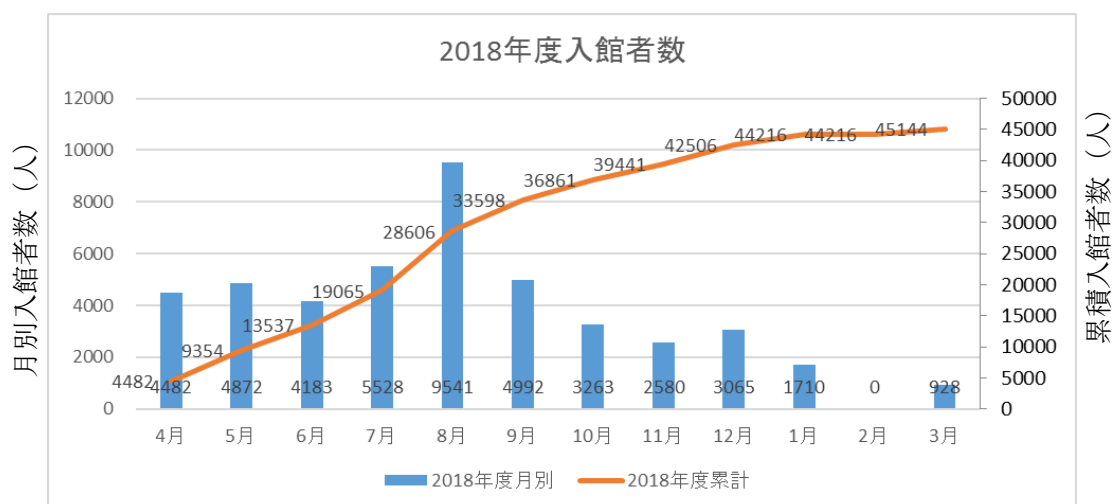
### 1. 入館者状況

平日は主に幼児連れのお客様や・学校・自治体による団体見学の利用が中心ですが、土・日・祝日や夏休みなどには多くのご家族に利用いただいています。特に、8 月は年間を通じて月間入館者数が最も多く、2018 年は 9,541 人と今年も前年を上回る数字となりました。2019 年 1 月 14 日までの入館者総数は 44,216 人と、年度途中ながら昨年度を少し上回りました。1 月 17 日～3 月 27 日の「ミニふおとん」には 3,512 人ご入場いただき、通常運用再開後 3 月 28 日～31 日の入館者数は 928 人でした。

入館者数（2018 年 4 月 1 日～2019 年 1 月 14 日及び 3 月 28 日～31 日）

		開館日数	入館者数	
			月別	累計
2018	4 月	22 日	4,482 人	4,482 人
	5 月	21 日	4,872 人	9,354 人
	6 月	22 日	4,183 人	13,537 人
	7 月	19 日	5,528 人	19,065 人
	8 月	23 日	9,541 人	28,606 人
	9 月	21 日	4,992 人	33,598 人
	10 月	19 日	3,263 人	36,861 人
	11 月	22 日	2,580 人	39,441 人
	12 月	20 日	3,065 人	42,506 人
2019	1 月	9 日	1,710 人	44,216 人
	2 月	-	-	-
	3 月	4 日	928 人	45,144 人
年度合計		202 日	45,144 人	-

### 2. 月別及び累積入館者数分布（2018 年 4 月 1 日～2019 年 1 月 14 日及び 3 月 28 日～3 月 31 日）



ミニふおとん入場者数（2019 年 1 月 17 日～2019 年 3 月 27 日）

		開館日数	入館者数	
			月別	累計
2019	1 月	11 日	665 人	665 人
	2 月	20 日	1,181 人	1,846 人
	3 月	19 日	1,666 人	3,512 人
合計		50 日	3,512 人	-



# Appendix



## 共同研究課題、施設共用課題

### 1) 木津地区

#### 【共同研究課題】

共同研究先	共同研究課題名	担当研究グループ
NTT アドバンステクノロジー(株)	高耐力軟X線光学素子に関する基礎研究	X線レーザー研究グループ
宇都宮大学、広島大学、東北大学	水の窓高輝度軟X線発生に関する基礎研究	X線レーザー研究グループ
慶應義塾大学、(株)ユニタック	レーザーを活用した整形外科インプラント設置強度評価機構の開発	X線レーザー研究グループ
東京学芸大学	リラクサー強誘電体のドメイン形成に関する研究	X線レーザー研究グループ
(株)島津製作所	高耐性光学デバイスの開発研究	X線レーザー研究グループ
大阪大学レーザー科学研究所	光学材料、光学薄膜の損傷機構のパーコレーションモデル	X線レーザー研究グループ
京都大学	レーザー誘起弾性波を用いた道路橋床板の非破壊検査に関する研究	X線レーザー研究グループ
(株)フォトン応用計測研究所	レーザー誘起振動波計測技術の小型化に関する研究	X線レーザー研究グループ
九州大学	高効率フェムト秒レーザーアブレーションに関する基礎研究	X線レーザー研究グループ
自然科学研究機構核融合科学研究所、東北大学	分子動力学シミュレーションを用いたフェムト秒レーザーアブレーションに関する研究	X線レーザー研究グループ
京都大学	高強度レーザーと構造的媒質との相互作用に関する研究	先端レーザー技術開発グループ
神戸大学	固体飛跡検出器を用いた高エネルギーイオン検出手法開発	先端レーザー技術開発グループ
大阪大学	宇宙物理の手法に基づく粒子加速・電磁放射に関する研究	先端レーザー技術開発グループ
東京大学、神戸大学	水素クラスターをターゲットとした100MeVを超えるレーザー陽子加速の実証	先端レーザー技術開発グループ
理化学研究所	テラヘルツパルス光源による高分子高次構造の制御	超高速光物性研究グループ
大阪大学	高強度テラヘルツパルス光源による新規物質創成と新規物性発現に関する研究	超高速光物性研究グループ
奈良先端科学技術大学院大学	有機マイクロキャビティを用いた強結合状態の観測と制御に関する基盤技術開発	超高速光物性研究グループ

日本電信電話株式会社 NTT 物性科学基礎研究所	アト秒パルスの波形計測と時間分解計測 に関わる基盤技術開発	超高速光物性 研究グループ
兵庫県粒子線医療センター	量子メスを目指した粒子線照射計測・制御 技術に関する研究	高強度レーザー科学 研究グループ
大阪大学	高安定レーザー電子加速に関する研究	高強度レーザー科学 研究グループ
ライトタッチテクノロジー 株式会社	中赤外レーザー顕微鏡の開発	レーザー医療 応用研究グループ
日本原子力研究開発機構	中性子散乱による生体高分子のダイナミ クス解析に関する研究	生体分子シミュ レーショングループ
理化学研究所	物理、化学、計算科学を統合した動的構造 生物学の確立	生体分子シミュ レーショングループ

### 【施設共用課題】

平成 30 年度全期施設共用課題

課題番号	利用 区分	施設装置	利用課題
2018A-K01	公開	X 線レーザー 実験装置	ダブルパルス照射による基板表面励起加工過程の 調査に関する研究
2018A-K02	公開	J-KAREN レーザー装置	無衝突衝撃波による準単色イオン加速物理の解明
2018A-K03	公開	J-KAREN レーザー装置	極短パルス高強度レーザーを用いた極限プラズマ の研究

### 2) 播磨地区

### 【共同研究課題】

共同研究先	共同研究課題名	担当研究グループ
高エネルギー加速器研究機 構	機能磁性材料の微細構造観察・解析手法 の開発	磁性科学研究グループ
兵庫県立大学	反応性ガスクラスタイオンビームによ る新規化合物の創製と電子状態の解析	磁性科学研究グループ
京都大学	同位体特定による局所状態解明のための 先進的メスバウアー分光法の開発研究	磁性科学研究グループ
広島大学	コヒーレント X 線を利用した強誘電体一 粒子計測	コヒーレント X 線 利用研究グループ
物質・材料研究機構	原子二体分布関数法による機能性材料の 先進的ナノ構造研究	高圧・応力科学 研究グループ

# 【施設共用課題】

播磨地区では関西研では 2012 年度より文部科学省のナノテクノロジープラットフォーム事業を受託しており、放射光科学研究施設を成果公開型課題で利用する外部研究者に対して、特に専用ビームラインにおける研究支援を強化しています。課題は年 2 回、SPring-8 を運営する公益財団法人高輝度光科学研究センターの一般課題募集時期（5 月及び 11 月）に合わせて募集しています。

## 平成 30 年度前期施設共用課題

課題番号	利用区分	利用装置	研究課題
2018A-H01	公開	放射光メスbauer分光装置	元素融合ナノ粒子の物性解明を目指した99Ru放射光メスbauer吸収分光法の開発
2018A-H02	公開	放射光メスbauer分光装置	Sm(Fe <sub>1-x</sub> Co <sub>x</sub> ) <sub>12</sub> 薄膜の内部磁場の温度依存性
2018A-H03	公開	共鳴X線非弾性散乱装置	水加ヒドラジン酸化触媒の「その場高分解能」XAFS解析
2018A-H04	公開	表面X線回折計	RF-MBE法による窒化物半導体成長初期過程のXRDその場観察
2018A-H05	公開	表面X線回折計	データサイエンス手法を応用した薄膜局所ひずみ分布測定
2018A-H06	公開	表面X線回折計	Si基板上GaAs成膜における歪緩和過程のその場X線構造解析
2018A-H07	公開	表面X線回折計	GaN薄膜上へのInGaNヘテロ成長におけるin-situ構造特性観察：格子極性の効果
2018A-H08	公開	表面X線回折計	その場X線回折測定を用いたグラフェン析出成長メカニズムの検討
2018A-H09	公開	表面X線回折計	グラフェン上でのGaN結晶成長過程のX線回折によるリアルタイム解析
2018A-H10	公開	表面X線回折計	InGaN量子構造形成におけるその場X線回折測定
2018A-H12	公開	高温高圧プレス装置	曲げ試験片を用いた高強度鋼薄板の水素脆化特性評価のための応力状態の解析
2018A-H13	公開	高温高圧プレス装置	高水素配位錯イオンを含む高密度水素化物の形成機構解明
2018A-H14	公開	単色X線実験用高温高圧プレス装置	鉄ニッケル融体の音速・密度に与える2軽元素の影響とその圧力変化：水星核の軽元素の検証
2018A-H15	公開	ダイヤモンドアンビルセル回折計	巨大負熱膨張関連物質の圧力誘起相転移の観察

2018A-H17	公開	ダイヤモンド アンビルセル回折計	X線PDF解析による加熱前後のセメント硬化体中のCa(OH) <sub>2</sub> 及びCSH変形挙動の解明
2018A-H18	公開	ダイヤモンド アンビルセル回折計	水素吸蔵合金の劣化メカニズムの解明 ～ 回復焼鈍による局所構造と水素吸蔵特性の回復挙動の観察 ～
2018A-H19	公開	ダイヤモンド アンビルセル回折計	拡張ナノ空間の溶液X線回折測定による水の構造解析と物性発現機構の解明
2018A-H21	公開	大型X線回折計	RNi <sub>3</sub> Al <sub>9</sub> (R=Tb,Dy,Ho)におけるらせん磁気および多極子秩序構造
2018A-H22	公開	大型X線回折計	強いスピン相互作用を持つ超格子薄膜の磁気秩序の解明
2018A-H23	公開	ダイヤモンド アンビルセル回折計	X線二対分布関数を用いた金属核発生過程のin situ解析

平成 30 年度後期施設共用課題

課題番号	利用 区分	施設装置	利用課題
2018B-H01	公開	放射光メスバウアー 分光装置	単分子磁石の微視的状態解明を目指したGd放射光メスバウアー吸収分光法の開発
2018B-H02	公開	放射光メスバウアー 分光装置	Sm(Fe <sub>1-x</sub> Cox) <sub>12</sub> 薄膜の内部磁場の温度依存性
2018B-H03	公開	放射光メスバウアー 分光装置	高感度放射光メスバウアー回折装置の開発
2018B-H04	公開	放射光メスバウアー 分光装置	軟磁性材料の放射光メスバウアー分光測定
2018B-H05	公開	共鳴非弾性X線 散乱装置	X線磁気円偏光発光法を用いた方向性珪素鋼板の内部磁区観察
2018B-H06	公開	表面X線回折計	放射光X線を用いた格子不整合III-V族化合物半導体混晶のリアルタイム構造解析
2018B-H07	公開	表面X線回折計	データサイエンス手法を活用した高速な位置特定と局所構造評価
2018B-H09	公開	表面X線回折計	その場X線回折測定を用いたグラフェン析出成長メカニズムの検討
2018B-H10	公開	表面X線回折計	単層二硫化モリブデンを中間層としたGaN結晶成長過程のX線回折によるリアルタイム解析
2018B-H11	公開	表面X線回折計	InGaN量子構造形成におけるその場X線回折測定

2018B-H12	公開	高温高圧プレス装置	異種材料溶接継手界面凝固部の攪拌状態と金属間化合物の非破壊測定
2018B-H13	公開	高温高圧プレス装置	白色X線を利用した二重露光法によるひずみマッピング技術の開発
2018B-H14	公開	高温高圧プレス装置	Mo系高水素配位錯体水素化物の形成機構解明
2018B-H15	公開	高温高圧プレス装置	低合金TRIP鋼の水素脆化メカニズム解明のための残留オーステナイト変態挙動の解析
2018B-H16	公開	高温高圧プレス装置	高エネルギー密度負極活物質C2Liの生成過程のその場観察
2018B-H17	公開	単色X線実験用 高温高圧プレス装置	外熱式DACを用いた高温高圧下におけるX線吸収法による密度測定
2018B-H19	公開	ダイヤモンド アンビルセル回折計	Mechanism for the destabilization of MgH <sub>2</sub> in a thin film form
2018B-H20	公開	ダイヤモンド アンビルセル回折計	異常散乱現象から得られる元素選択的二体分布関数解析を用いた異なる無機カチオン種がゼオライトの結晶化に与える影響の解明
2018B-H22	非公開	大型X線回折計	鋼鉄溶接部・せん断部周辺の残留応力評価

## 関西光科学研究所での各種シンポジウム・施設公開・出展・アウトリーチ活動

関西研（木津地区、播磨地区）では、各種シンポジウム、セミナー、ワークショップ、研究会等を開催しています。また、研究所として参加した会合についても、主なものを記載しています。その他、関西研では、施設公開（播磨地区1回（毎年4月ごろ）、木津地区1回（毎年10月ごろ））や研究成果のわかり易い公表、光科学の基礎についての出前授業、科学啓発イベント等への出展を積極的に進めています。

ここでは主なものを記載し、「きつづ光科学館ふおとん」、S-cube（スーパーサイエンスセミナー）については別途記載しています。

### 【木津地区】

1	8-April-2018	高崎量子応用研究所（群馬県高崎市）	主催：高崎量子応用研究所
	第41回花と緑の見学会		
2	8-9-May-2018	関西光科学研究所（木津地区：京都府木津川市）	主催：量研関西光科学研究所、大阪大学レーザー科学研究所
	光・量子ビーム科学合同シンポジウム 2018 OPTO2018 Symposium on Photon and Beam Science		
3	6-8-June-2018	関西光科学研究所（木津地区：京都府木津川市）	主催：化学反応討論会実行委員会
	第34回化学反応討論会		
4	3-July-2018	関西光科学研究所（木津地区：京都府木津川市）	主催：公益社団法人日本分光学会関西支部
	日本分光学会 関西支部 平成30年度 第1回講演会・見学会		
5	28-29-July-2018	科学技術館（東京都千代田区）	主催：日本科学技術振興財団
	青少年のための科学の祭典 2018		
6	2-3-August-2018	インテックス大阪（大阪府大阪市住之江区）	主催：日本能率協会
	夏休み 2018 宿題自由研究大作戦		
7	4-5-October-2018	けいはんなオープンイノベーションセンター（京都府相楽郡精華町）	主催：京都スマートシティエキスポ運営協議会
	京都スマートシティエキスポ 2018		
8	4-5-October-2018	けいはんなプラザ（京都府相楽郡精華町）	主催：関西文化学術研究都市推進機構
	けいはんなビジネスメッセ 2018		
9	25-27-October-2018	けいはんなプラザ（京都府相楽郡精華町）	主催：けいはんな情報通信フェア 2018 実行委員会、情報通信研究機構、関西文化学術研究都市推進機構、国際電気通信基礎技術研究所、関西経済連合会
	けいはんな情報通信フェア 2018		



10	28-October-2018	関西光科学研究所（木津地区：京都府木津川市）	主催：関西光科学研究所
	関西光科学研究所施設公開（木津地区）		
11	26-29-November-2018	関西光化学研究所（木津地区：京都府木津川市）、奈良春日野国際フォーラム”麓”（奈良県奈良市）	主催：関西光科学研究所
	The 8th Asian Summer School & Symposium on Laser Plasma Acceleration and Radiation (ASSS-8)		
12	27-November-2018	関西光科学研究所（木津地区：京都府木津川市）	主催：関西光科学研究所、大阪大学レーザー科学研究所、HZDR
	第2回 HZDR-KPSI-ILE ワークショップ		
13	28-29-November-2018	奈良春日野国際フォーラム”麓”（奈良県奈良市）	主催：量子科学技術研究開発機構
	2nd QST International Symposium “Frontier of Quantum Beam Science with High Power Lasers”		
14	6-7-December-2018	福井大学附属国際原子力工学研究所（福井県敦賀市）	主催：日本原子力研究開発機構（敦賀総合研究開発センター）
	レーザー応用技術・産学連携成果報告会		
15	23-January-2019	在アメリカ合衆国日本国大使館（米国ワシントン D.C.）	主催：日本学術会議
	ハイパワーレーザーによる高エネルギー密度科学の展望		

#### 【播磨地区】

1	29-April-2018	SPring-8（兵庫県佐用郡佐用町）	主催：理化学研究所放射光科学総合研究センター
	第27回 SPring-8/SACLA 施設公開（関西研）		
2	8-11-July-2018	SPring-8（兵庫県佐用郡佐用町）	主催：兵庫県立大学大学院物質科学研究科・生命科学研究科、関西学院大学大学院理工学研究科、東京大学放射光連携研究機構、岡山大学大学院自然科学研究科、大阪大学・光科学連携センター・蛋白質研究所・核物理研究センター、（公財）高輝度光科学研究センター、理化学研究所放射光科学総合研究センター、日本原子力研究開発機構 物質科学研究センター、量子科学技術研究開発機構 放射光科学研究センター
	第18回 SPring-8 夏の学校		
3	21-22-July-2018	姫路科学館（兵庫県姫路市）	主催：姫路市
	姫路桜山公園まつり「科学の屋台村」		
4	8-August-2018	けいはんなプラザ（京都府相楽郡精華町）	主催：QST 微細構造解析プラットフォーム、JAEA 微細構造解析プラットフォーム、NIMS 微細構造解析プラットフォーム
	平成30年度文部科学省ナノテクノロジープラットフォーム事業 JAEA&NIMS&QST 微細構造解析プラットフォーム放射光設備利用講習会		

5	25-26-August-2018	SPring-8（兵庫県佐用郡佐用町）	主催：SPring-8 ユーザー協同体（SPRUC）、 （公財）高輝度光科学研究センター、理化学 研究所放射光科学研究センター、兵庫県立 大学
	SPring-8 シンポジウム 2018		
6	18-October-2018	播磨高原東中学校（兵庫県たつの市）	主催：関西光科学研究所 研究企画室（播磨）
	播磨高原東中学校出前授業		
7	9-11-January-2019	福岡国際会議場（福岡県福岡市）	主催：第 32 回日本放射光学会年会・放射 光科学合同シンポジウム組織委員会
	第 32 回日本放射光学会年会・放射光科学合同シンポジウム		
8	30-January-1- February-2019	東京ビッグサイト（東京都江東区）	主催：nano tech 実行委員会
	nano tech 2019		
9	12-February-2019	兵庫県立先端科学技術支援センター（兵庫県赤穂郡上郡町）	主催：兵庫県立大学
	兵庫県立大学理学部・大学院物質理学研究科/生命理学研究科 技術・人材マッチング交流会		
10	22-February-2019	TKP ガーデンシティ京都（京都府京都市下京区）	主催：京大微細構造解析プラットフォーム 最先端構造観察・計測共用拠点 JAEA 微細構造解析プラットフォーム QST 微細構造解析プラットフォーム
	京大・JAEA・QST 微細構造解析プラットフォーム地域セミナー 電顕・放射光による反応・構造解析		
11	1-March-2019	SPring-8（兵庫県佐用郡佐用町）	主催：関西光科学研究所 放射光科学研究 センター、QST 微細構造解析プラットフォーム
	QST 放射光科学シンポジウム 2019/文部科学省ナノテクノロジープラットフォーム事業微細構造解析 プラットフォーム放射光利用研究セミナー		

## KPSI セミナー

木津地区では国内外の著名な研究者をお招きして学術的に最先端の専門的なセミナーを開催しています。今年度は合計 18 回のセミナーを開催しました。開催にあたっては KPSI Web サイトやメールリングリストを活用し、関西研内外に開催案内を行っています。また、報告についても Web サイトを活用しています。

Web サイト : <https://www.qst.go.jp/site/kansai/list68-180.html>

35	9-April-2018	Dr. Sae Chae Jeoung	Korea Research Institute of Standard and Science, Daejeon / Korea
36	19-April-2018	Prof. David NEELY	Central Laser Facility, Rutherford Appleton Laboratory, United Kingdom
37	21-May-2018	Dr. Aleksei Lopatin	Institute for Physics of Microstructures, Russian Academy of Science, Russia
38	30-May-2018	Prof. Gautam Basu	Department of Biophysics, Bose Institute, India
39	4-July-2018	Prof. Daisuke Kihara	Department of Biological & Computer Science, Purdue University, USA
40	11-July-2018	Prof. Bhuvanesh Ramakrishna	Indian Institute of Technology Hyderabad
41	31-July-2018	Dr. Toshiaki Nakano	Radiation-Induced DNA Damage Group, KPSI, QST, Japan
42	24-August-2018	Prof. Masami TERAUCHI	Institute of Multidisciplinary Research for Advanced Materials, Tohoku Univ.
43	26-October-2018	Associate Professor, Kaori Fukuzawa	Laboratory of Chemical and physical chemistry, Faculty of Pharmaceutical Sciences, Hoshi University
44	5-September-2018	Associate Professor, Kenji Sakota	Department of Chemistry, Faculty of Science/ Division of Molecular Materials Science, Graduate School of Science, Osaka City University

45	26-September-2018	Prof. Lee-Wei Yang	Institute of Bioinformatics and Structural Biology, National Tsing Hua University, Taiwan
	Resolution-exchanged structural modeling and simulations jointly unravel that subunit rolling underlies the mechanism of programmed ribosomal frameshifting		
46	3-October-2018	Oanh T. P. KIM, Ph.D	Environmental Genomics Laboratory, Institute of Genome Research (IGR), Vietnam Academy of Science and Technology (VAST).)
	A draft genome of the striped catfish ( <i>Pangasianodon hypophthalmus</i> )		
47	11-December-2018	Dr. Masato KOIKE	Department of Advanced Photon Research, KPSI, QST, Japan
	Soft X-ray high resolution / high diffraction efficiency holographic diffraction gratings —Developments and applications to spectrometers—		
48	16-January-2019	Jun Nakamura, D.V.M., Ph.D.	Laboratory of Laboratory Animal Science, Graduate School of Life and Environmental Biosciences, Osaka Prefecture University
	Oxidative Damage to Macromolecules in Carcinogenesis and Atherogenesis		
49	4-March-2019	Tokuei SAKO, PhD.	Laboratory of Physics, College of Science and Technology, Nihon University
	Light-nanomatter interaction : basic theory and computational approach		
50	6-March-2019	Prof. Naoki HOSOYA	Department of Engineering Science and Mechanics, Shibaura Institute of Technology
	Vibration acoustic study using nanosecond laser		
51	20-March-2019	Kei NAKAMURA, PhD.	Lawrence Berkeley National Laboratory, USA
	Recent progress on laser plasma accelerator development at Lawrence Berkeley National Laboratory		
52	28-March-2019	Katsuhiro MIKAMI	X-ray Laser Group, Department of Advanced Photon Research ,KPSI, QST, Japan
	Optimization study and the medical application of detection method with laser-induced vibration		

## QST 播磨セミナー

播磨地区では国内外の著名な研究者をお招きして学術的に最先端の専門的なセミナーを開催しています。

6	28-June-2018	Dr. Shigehito ISOBE	Graduate School of Engineering, Hokkaido Univ
	Study on Reaction Mechanisms of Hydrogen Storage Materials		
7	5-July-2018	Dr. Mitsuru Imaizumi	Research and Development Directorate, Japan Aerospace Exploration Agency (JAXA)
	Development of space solar cells in Japan —background and current state—		
8	11-July-2018	Masaki Tsubota	Physonit Inc.
	High accuracy refinement of crystal structure parameters via powder diffraction patterns		
9	10-October-2018	Masato Koike, Visiting Researcher	Department of Advanced Photon Research, Kansai Photon Science Institute
	Soft X-ray high resolution / high diffraction efficiency holographic diffraction gratings —Developments and applications to spectrometers—		
10	18-October-2018	Hideaki Iwasawa, Associate professor	Department of Physical Science, Graduate School of Science Hiroshima University
	State-of-the-art synchrotron-radiation APRES: Present and future perspective		

## S-cube (スーパーサイエンスセミナー)

中学高校生を中心に一般の方に光科学についての理解を深めていただくことを目的に、第一線の研究者による講義「S-cube (エスキューブ：スーパーサイエンスセミナー)」を開講しています。2018年度は合計11回(第199回～第209回)開催しました。

Web サイト：<https://www.qst.go.jp/site/kansai/list68-179.html>

199	15-June-2018	講師：今園 孝志 X線レーザー研究グループ	83人参加
	テーマ：光、色々		
200	25-July-2018	講師：赤木 浩 超高速光物性研究グループ	33人参加
	テーマ：分子を分けるって？ ～レーザー同位体分離について～		
201	27-July-2018	講師：近藤 康太郎 高強度レーザー科学研究グループ	50人参加
	High power lasers open a new world for science		
202	22-August-2018	講師：小川 奏 ライトタッチテクノロジー株式会社	45人参加
	テーマ：非線形光学で広がるレーザーの世界		
203	05-September-2018	講師：宮坂 泰弘 先端レーザー技術開発グループ	12人参加
	テーマ：光同期ナノ秒レーザー開発とフェムト秒レーザーアブレーション		
204	17-October-2018	講師：河野 秀俊 生体分子シミュレーショングループ	40人参加
	テーマ：スーパーコンピュータで探るタンパク質分子の形と動き		
205	27-November-2018	講師：森林 健悟 放射線 DNA 損傷研究グループ	45人参加
	テーマ：光と放射線のおはなし		
206	23-January-2019	講師：福田 祐仁 先端レーザー技術開発グループ	81人参加
	テーマ：レーザープラズマ科学入門		
207	31-January-2019	講師：中野 敏彰 放射線 DNA 損傷研究グループ	40人参加
	テーマ：DNA の傷により生じる癌と DNA に傷を作ることによる癌治療		
208	01-February-2019	講師：近藤 康太郎 高強度レーザー科学研究グループ	39人参加
	テーマ：光に導かれてきた？これまでの軌跡とこれから		
209	01-February-2019	講師：赤松 憲 放射線 DNA 損傷研究グループ	37人参加
	テーマ：DNA の“ヒミツ”ーキズがついても治りますー		





関西光科学研究所2018年度年報  
KPSI Annual Report 2018

【発行】

2019(令和元)年6月

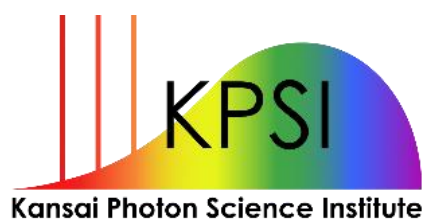
【編集・発行】

国立研究開発法人 量子科学技術研究開発機構  
量子ビーム科学部門 研究企画部  
関西光科学研究所 庶務課

【印刷】

株式会社アイプリコム

©2019 国立研究開発法人 量子科学技術研究開発機構



**Kansai Photon Science Institute**  
**Quantum Beam Science Research Directorate**  
**National Institutes for Quantum and Radiological Science and Technology**

8-1-7, Umemidai, Kizugawa-shi, Kyoto 619-0215, Japan  
<https://www.qst.go.jp/site/kansai-english/>